

ON THE PROPAGATION AND LEAKAGE OF SOLAR ACOUSTIC *P* MODES INTO THE SOLAR ATMOSPHERE

Chris Malins

Submitted for the degree of PhD

Supervised by Professor R. von Fáy-Siebenbürgen

Solar Physics and Space Plasma Research Centre

Department of Applied Mathematics

The University of Sheffield

Sheffield, October 2010

Abstract

Oscillatory signals with a peak period of around 5 minutes, the solar global p modes, are ubiquitously observed at the solar surface. Higher in the atmosphere, signals have been widely observed with shorter periods, notably of about 3 minutes (longer periods have also been seen). Links between the 5 minute p modes and shorter period atmospheric oscillations have often been proposed, with several possible mechanisms for transmission suggested. The area of short cut-off period around the solar photospheric temperature minimum is usually considered as a barrier to direct propagation of 5 minute signals. This thesis uses numerical simulation to investigate possible transmission of solar surface signals, in particular the solar global p modes, into the Sun's atmosphere. It demonstrates two possible mechanisms by which a shorter period signal might drive shorter period signals in the higher atmosphere - resonant excitation of cut-off frequency modes in the photosphere and transition region and the excitation of standing modes in the chromospheric cavity. Further investigation is indicated to examine numerically the outcomes of the application of a more realistic photospheric driver. Simulations performed in the case of a more dynamic transition region may also yield further results, including potential reductions in the periods of driven chromospheric/transition region signals.

Acknowledgments

I would like to thank all those at the Sheffield University Department of Applied Mathematics whose support has made it possible for me to produce this thesis. In particular, my heartfelt thanks go to Viktor Fedun and Sergiy Shelyag, whose numerical advice and work on the ‘Not the VAC’ (SAC) code made my final results possible; Richard Balthazor and Jon Clark in turn for keeping my computers running; Maureen Maltby for (repeatedly) rescuing me when locked out of my office; Mats Carlsson, Viggo Hansteen, Marcel Goossens and Roni Keppens for enabling me to undertake research excursions beyond these fair isles; Gary Verth and Youra Taroyan for mathematical and physical insights and keeping me company in various drinking haunts; and of course Robertus without whose guidance and support I would certainly not have been able to finish. I would like to dedicate this thesis to the memory of my friend Professor Cesar Mendoza-Briceño, whose support and friendship was of great value to a wide-eyed first year PhD student, and who is greatly missed.

Contents

1	Introduction	10
1.1	The basics	10
1.1.1	A little history	11
1.1.2	Remarks on a mass of incandescent gas	13
1.1.3	The atmosphere	15
1.2	Sun waves	19
1.3	Solar atmospheric wave propagation	21
1.3.1	Aim of this thesis	23
2	Physics	24
2.1	The equilibrium	24
2.2	The equations	27
2.2.1	The MHD equations	28
2.2.2	The HD equations	29
2.2.3	The altered MHD equations for the CD4 scheme	29
2.3	MHD waves	31
2.4	The solar atmospheric acoustic cut-off period	33
2.4.1	Deriving the cut-off period - the Klein-Gordon equation	34
2.4.2	A multitude of cut-off frequencies	35
2.4.3	Cut-off in VAL IIIc	38
2.4.4	Resonance and reflection	40
2.4.5	Cold chromosphere	41
2.4.6	Magnetic field	41

3 Numerics	43
3.1 Introduction	43
3.2 Numerical (M)HD	45
3.2.1 Finite differences	45
3.2.2 Finite volumes	46
3.2.3 Finite elements	46
3.2.4 Total variation diminishing schemes	46
3.3 HD simulations	49
3.4 MHD simulations - the modified CD4 scheme	50
3.4.1 An MHD code for gravitationally stratified media	50
3.4.2 Equations of perturbed MHD	51
3.4.3 Numerical methods	52
4 Leakage of point driven photospheric acoustic waves into non-magnetic solar atmosphere	55
4.1 Abstract	55
4.2 Introduction	56
4.3 Short period	59
4.3.1 30 second driver	59
4.4 Long period	64
4.4.1 300 second driver	64
4.4.2 Standing waves	68
4.4.3 Transition region guided waves	73
4.4.4 Cavity modes	76
4.4.5 Cold chromospheric case	78
4.5 Summary	80
5 Direct propagation of photospheric acoustic waves into non-magnetic solar atmosphere	82
5.1 Abstract	82
5.2 Introduction	83
5.3 Multiple Drivers	85
5.3.1 In-phase drivers	85

5.3.2	Drivers out of phase by π radians	86
5.3.3	Drivers with slightly different periods	88
5.4	Wide Coherent Driver	90
5.4.1	‘Fundamental’ mode	90
5.4.2	‘First harmonic’	92
5.4.3	Chromospheric cavity	94
5.5	Summary	94
6	Transition region granulation driven by synthetic photospheric motions	96
6.1	Abstract	96
6.2	Introduction	96
6.3	Transition region granulation	97
6.3.1	Point drivers	97
6.3.2	Horizontally coherent driver	100
6.4	Summary	102
7	Propagation of synthetically driven photospheric acoustic waves into the atmosphere of the quiet Sun	104
7.1	Abstract	104
7.2	Introduction	104
7.3	Results	108
7.3.1	Fast mode	108
7.3.2	Transition region surface wave	111
7.3.3	Slow mode	116
7.3.4	Chromospheric standing waves	118
7.4	Summary	120
8	Summary and conclusions	122
8.1	Overview of the thesis	122
8.2	Conclusions	123
8.3	Relevance to observations	125
8.4	Further work	126

List of Figures

1.1	Plot of the solar atmospheric temperature profile highlighting the transition region (Sheung 2003)	18
2.1	Variation in cut-off period with changing height ignoring stratification (dashed line) and including stratification (solid line) for a VAL IIIc solar atmosphere.	39
4.1	Typical snapshot of the vertical velocity in the model for the 30 second driver, taken after 869 seconds. On the left is a visualisation of the full domain (note that the aspect ratio is not 1:1 for convenience of presentation), accompanied on the right by a plot taken along a vertical cross-section at the centre of the domain.	60
4.2	a) Time-distance image for 30 second driver showing waves moving across a line taken at 1.3 Mm into the atmosphere (in the chromosphere). b) Similar to (a) but taken at a height of 3.3 Mm and thus in the corona.	60
4.3	Time distance image along the central vertical axis of the computational domain showing vertical velocity. The dotted lines show where the cut-off frequency is exactly 300 seconds.	64
4.4	a) Time-distance image for 300 second driver showing vertical velocity along a horizontal line taken at 1.3 Mm into the atmosphere (in the chromosphere). b) Similar to a, but taken at a height of 3.3 Mm and thus in the corona.	65
4.5	Same as Fig. 4.1 but for a 300 second driver, snapshot taken after 1412 seconds.	68
4.6	a) Here the vertical velocity along the central vertical axis of the computational domain is plotted on the same axes for each gridpoint in the range $650 \text{ km} < z < 3.3 \text{ Mm}$. b) Similar to a, but in the range $700 \text{ km} < z < 1 \text{ Mm}$. c) Similar to a, but in the range $1.1 \text{ Mm} < z < 1.9 \text{ Mm}$. d) Similar to a, but in the range $2.1 \text{ Mm} < z < 2.5 \text{ Mm}$	69
4.7	The four lines on this graph plot the vertical velocity at four different heights on the central axis. The solid line is at the driver height, the dotted line is above the driver in the lower chromosphere where the 300 second signal is evanescent, the dashed line is in the chromospheric cavity and the dot-dashed line is in the transition region.	71

4.8	Time series of images showing the development of a guided wave at the transition region from a 300 second driven signal.	73
4.9	Snapshot of the log of the temperature in the computational domain for a simulation driven with an amplitude of 760 ms^{-1} , zoomed in to show the development of fine structure rising from the transition region, taken after 1510 seconds. . .	75
4.10	Power spectrum for the case with a 300 second driver taken along a horizontal cross-section at 1.3 Mm height.	76
4.11	Power spectrum for the case with a 300 second driver taken along a horizontal cross-section at 3.3 Mm height.	77
4.12	Snapshot of the log of the temperature from the cold chromospheric case with a 300 second driver, with a section of the transition region expanded to show small cold protrusions rising towards the low corona.	78
4.13	Time distance image along the central vertical axis of the computational domain showing vertical velocity.	79
5.1	Snapshot of the vertical velocity in the computational domain after 2676 seconds for two in-phase 5 minute drivers, on the left looking at the whole domain, and on the right a plot of vertical velocity along a central vertical line.	85
5.2	a) Time-distance image for a pair of drivers out of phase by π radians showing vertical velocity along a horizontal line taken at 1.3 Mm into the atmosphere (in the chromosphere). b) Corresponding power spectrum for a line at height 1.3 Mm in the chromosphere.	87
5.3	As in Fig. 5.1, but after 2894 seconds for two out-of-phase 5 minute drivers. . .	88
5.4	Arrows representing the magnitude and direction of the flow are superimposed on an image of the change from equilibrium temperature (brighter areas are hotter) in a region of the domain centred on the transition region.	89
5.5	As in Fig. 5.1 but after 2736 seconds for drivers with period 5 minutes (left driver) and 270 seconds (right driver).	90
5.6	Set of snapshots of the log of temperature in the computational domain for the fundamental driver.	91
5.7	Signal in vertical velocity at 2.3 Mm height (transition region) in the horizontal centre of the domain.	92
5.8	Set of snapshots of the log of temperature in the computational domain for the first harmonic wide driver.	93
6.1	Arrows with length proportional to speed of flows at the transition region, superimposed on an image showing changes from the equilibrium temperature (brighter is hotter than equilibrium, darker is cooler), after 1082 seconds. . .	97
6.2	As Fig. 6.1 but taken after 1172 seconds.	98

6.3	Comparison of velocity components in the vertical and horizontal directions taken at a height of 5.3 Mm in the horizontal centre of the domain, for case driven by two 300 second point drivers with a phase difference of π . Solid line is horizontal component, dotted line is vertical.	99
6.4	As in Fig. 6.1 but for case of ‘first harmonic’ horizontally coherent driver with 300 second period and 250 ms^{-1} amplitude, taken after 330 seconds.	100
6.5	As in Fig. 6.1 but for case of ‘first harmonic’ horizontally coherent driver with 300 second period and 250 ms^{-1} amplitude, taken after 503 seconds.	101
6.6	As in Fig. 6.3 but for case of ‘first harmonic’ horizontally coherent driver with 300 second period and 250 ms^{-1} amplitude.	102
7.1	Plasma β in the equilibrium domain.	105
7.2	Sound speed (solid line) and Alfvén speed (dashed line) in the equilibrium domain.	107
7.3	Series of snapshots of the vertical velocity in the computational domain taken at 37.5 second intervals.	109
7.4	Time difference image showing the propagation of signals along a line drawn vertically through the driver application point.	110
7.5	Vertical time difference image with vertical velocity peaks highlighted as follows: a) initial fast mode pulse and reflection highlighted with white lines; b) slow mode signals in the corona and possible slow mode signals in the photosphere/chromosphere highlighted with black lines; c) resonant wake oscillations highlighted with green ellipses; d) quasi-standing modes in the chromospheric cavity highlighted with green boxes.	112
7.6	Series of snapshots of the velocity in the computational domain taken at 37.5 second intervals. The left hand side of each image shows the velocity magnitude only, while on the right hand side arrows represent the flow direction	115
7.7	Power spectrum taken at a height of 1.8 Mm, in the chromospheric cavity . . .	118
7.8	Time distance images taken along horizontal lines at 1.3 Mm, 1.8 Mm (both in the chromospheric cavity), 2.3 Mm (at the transition region) and 2.8 Mm (in the corona)	119

Chapter 1

Introduction

1.1 The basics

The Sun is a mass of incandescent gas

A gigantic nuclear furnace

Where hydrogen is built into helium

At a temperature of millions of degrees

Yo ho, it's hot, the Sun is not

A place where we could live

But here on Earth there'd be no life

Without the light it gives

We need its light

We need its heat

We need its energy

Without the Sun, without a doubt

There'd be no you and me

The Sun is a mass of incandescent gas

A gigantic nuclear furnace

Where hydrogen is built into helium

At a temperature of millions of degrees

The Sun is hot

It is so hot that everything on it is a gas: iron, copper, aluminum, and many others.

The Sun is large

If the Sun were hollow, a million Earths could fit inside. And yet, the Sun is only a middle-sized star.

The Sun is far away

About 93 million miles away, and that's why it looks so small.

And even when it's out of sight

The Sun shines night and day

The Sun gives heat

The Sun gives light

The sunlight that we see

The sunlight comes from our own Sun's

Atomic energy

Scientists have found that the Sun is a huge atom-smashing machine. The heat and light from the Sun come from the nuclear reaction between hydrogen, nitrogen, helium, carbon, boron, chloron, fluoron, moron, and oestrogen.

The Sun is a mass of incandescent gas

A gigantic nuclear furnace

Where hydrogen is built into helium

At a temperature of millions of degrees

Everything that a person might normally be expected to need to know about the Sun is summed up rather nicely by They Might Be Giants (1998) in the above paean to all things solar. Fortunately for such unfortunates as see fit to seek solace in the pursuit of the sciences, upon closer inspection it turns out that there is a great deal more to know and understand about our local star, a smörgåsbord of which is presented here.

1.1.1 A little history

Scientific opinion is divided on who the first person to observe the Sun was. Although to the modern reader it may seem remarkable that the discovery of such a significant celestial object would go without comment, and indeed fail to win its team a Nobel Prize, it seems that either nobody at the time thought to write it up properly (or possibly that the journal it

was mentioned in was lost to posterity as a result of the destruction of the Great Library at Alexandria). Either way, a significant tract of history drifted past under the Sun's watchful eye without an undue level of progress being made in the understanding of it.

Early explanations of the Sun tended towards the supernatural. Indeed, to cultures such as the Inca and Aztecs the Sun was less an object for scientific study than a deity in its own right, while the ancient Greeks considered the Sun to be the chariot of the god Helios. The Judaeo-Christian tradition veered away from such indulgences of anthropomorphic personification, but failed to correctly ascertain the nature of the relation of the Sun to the Earth - placing the Sun as an object circling the world in the heavens.

There were some thinkers amongst the ancient Greeks who postulated alternative, rather more scientifically inclined explanations for the Sun than the Helios hypothesis. Anaxagoras in the fifth century BC, for instance, reasoned that the Sun was not a deity, but rather believed it to be a ball of flaming metal, which he claimed must be larger than the Peloponnesus. This was an insight for which he was imprisoned by the authorities and sentenced to death, an approach by society to solar physicists which has happily been phased out more recently. Moving on from Anaxagoras, the Greek Eratosthenes, working in the third century BC, calculated the distance of the Earth from the Sun to be 149 million kilometres, which is very much similar to the figure accepted by modern science.

Various ancient thinkers, amongst them the Greek Aristarchus and the legendary Indian sage Yajnavalkya, were of the opinion that the Sun did not move around the Earth, but that the Earth in fact moved around the Sun. These notions were revived in the West by the astronomer Copernicus, and the support rendered by Galileo Galilei to the theory landed him in much the same position relative to the Catholic Church as Anaxagoras had previously found himself in relative to the Greek authorities. Galileo recanted the notion having been tried for heresy by the Inquisition, and the Church happily declined to sentence him to death.

Posterity has come to the conclusion that Aristarchus was indeed correct, but the question of whether the Earth revolves around the Sun or vice versa is, however, not of such relevance to us here as the question of what the Sun actually is and how it behaves. Although humanity did spend a significant period of time in blissful ignorance of the nature of the Sun, even without

the benefit of a telescope it is possible to deduce that the Sun has more going on than just being a large warm circle. By the fourth century BC the Chinese astronomer Gan De had observed and noted the presence upon the Sun of dark areas, sunspots. These continued to be observed systematically with the naked eye by Chinese astronomers, and their existence denied gamely by European theologians, for some time after. From the observation of sunspots it is possible to infer both that the Sun is spinning (by watching the spots move) and that the Sun is not without ‘imperfections’ (much to the chagrin of the theologians) and variations.

The second sign that all is not so simple as it seems with the fire ball in the sky is available at eclipse, in the form of the solar corona. The first well documented observation of the corona comes courtesy of Byzantine historian Leo Diaconus (ca. 950-994 AD). Having observed the total eclipse of 22 December 968 from Constantinople (now Istanbul, Turkey, a matter addressed in another instructive ditty covered by the aforementioned ‘They Might Be Giants’) he wrote in the Annales Sangallenses:

“...at the fourth hour of the day ... darkness covered the earth and all the brightest stars shone forth. And it was possible to see the disk of the Sun, dull and unlit, and a dim and feeble glow like a narrow band shining in a circle around the edge of the disk”.

As it turns out, the Sun’s corona and the layers of atmosphere beneath it are of a complexity that Mr Diaconus could hardly have imagined, and it is this dynamically rich area of the Sun which has the privilege of monopolising our attention here.

1.1.2 Remarks on a mass of incandescent gas

The Sun is, then, an extremely complex sort of an object, and both its interior and its atmosphere are highly dynamic and inhomogeneous. While the atmosphere is the region of most interest here, it wouldn’t do to ignore entirely the rest of the Sun, which for convenience can be divided into regions based on the physical processes which dominate them.

The core

The Sun's core is the region in which energy is generated through thermonuclear reactions. It extends from the centre of the Sun to approximately one quarter of the solar radius, and the centre of the Sun has a density of around $1.6 \times 10^5 \text{ kg m}^{-3}$ and a temperature of about 15 million degrees Kelvin. This combination of high density and high temperature allows the Sun to sustain the nuclear fusion reactions which are gradually converting part of the Sun's mass into energy. The bulk of the Sun, about 90%, consists of hydrogen, with about 10% being helium and a very small quantity of heavier elements contributing about 0.1%. The key energy producing nuclear reaction in the Sun is the proton-proton cycle, in which the protons from hydrogen nuclei are fused through several stages to form helium nuclei, with a corresponding decrease in mass and release of energy.

This energy is released mainly in the form of high energy γ ray photons, with the rest being given to neutrinos. The mean free path of a photon in the Sun's core, or the average distance a photon can travel without bumping into something, is of the order of $1 \times 10^{-2} \text{ m}$, and it therefore takes a very long time for the energy released to travel out of the core and all the way to the surface. Indeed, a typical photon which leaves the Sun and might be observed on Earth would have been travelling for around 10^7 years.

The radiative zone

Both the temperature and the density of the Sun decrease outwards from the solar centre, and beyond the core region they are no longer high enough for any significant rate of thermonuclear reactions to occur. The region beyond the core is known as the radiative zone, and extends to about 70% of the solar radius. It is known as the radiative zone, because in this region radiation is the dominant physical mechanism of energy transfer. Here, the high energy photons coming from the core are constantly being absorbed and re-emitted by electrons, protons and the nuclei of heavier elements. The density and temperature continue to drop through this region, with the density reducing from about the density of gold at the edge of the core to below the density of water at the top of the radiative zone, and the temperature dropping from about 7 million to 2 million degrees Kelvin.

The convection zone

An element of fluid which is heated, for instance by absorbing radiation, so that it becomes hotter than its surroundings will experience a buoyancy force and tend to rise, a process known as convection. If the extra heat is quickly lost again by thermal conduction and radiation, the fluid element will drop back to its original position, and the fluid is considered convectively stable. If on the other hand the fluid element loses its extra heat slowly, it will continue to expand and rise, and the fluid is considered convectively unstable. The criteria which determines convective instability is the Schwarzschild criterion,

$$-\frac{dT}{dr} < -\frac{\gamma - 1}{\gamma} \frac{T}{P} \frac{dP}{dr} \quad (1.1)$$

, where T is the temperature of the fluid, r is a measure of distance parallel to the gravitational field, P is the fluid pressure and γ is the adiabatic index of the plasma.

The radiative zone ends when the temperature reduces to about 2 million Kelvin, and some of the heavier elements which make up the Sun (such as nitrogen, oxygen, carbon, calcium and iron) are no longer fully ionised. The presence of partially ionised elements allows part of any additional heat input to the plasma to be absorbed in the ionisation energy, reducing the adiabatic index γ towards 1. The temperature gradient increases and the fluid becomes convectively unstable. From this height outwards to the solar surface is therefore known as the convection zone, because convection rather than radiation becomes the dominant mechanism of heat transfer.

At the top of the convection zone, the temperature has dropped to around 5,700 K, and the density has further reduced to about 2×10^{-5} kgm $^{-3}$. The convective motions themselves are visible at the surface as granules and supergranules. The edges of the granules are the areas where material lifted by convection falls back into the solar interior, having given up its additional energy.

1.1.3 The atmosphere

Above the convection zone lies the relatively diffuse solar atmosphere. The Sun does not have a ‘surface’ in the sense of the word which is applicable on a body such as the Earth with clearly

divided states of solid, liquid and gas. Rather, the Sun consists of material all of which is in a plasma state. Although the density of gas in the outer reaches of the corona may be many orders of magnitude below that at the photosphere, there is no single well defined surface at which the Sun's interior stops and atmosphere begins such that an intrepid solar explorer could sail a ship along it. The Sun's surface tends to be defined as the layer at which the optical depth to visible light (specifically light at 5,000 Å) as observed from the Earth is exactly 1, i.e. the surface of the Sun is by definition the depth beyond which it is impossible to see using optical telescopes alone.

Photosphere

The solar surface lies in the photosphere. This layer is named from the Greek word for light. It is the region from which the bulk of the light in the visible spectrum that reaches the Earth is emitted. Visible light emitted lower, within the convection zone, is normally absorbed and re-emitted higher in the atmosphere. Higher in the atmosphere, the Sun's density continues to fall off and the amount of light emitted is proportionately reduced. The temperature falls in the photosphere from a value of about 5,700 K at the surface to the photospheric temperature minimum, about 500 km above the convection zone, where the solar temperature drops to 4,100 K. This photospheric temperature minimum is the coldest 'static' region of the Sun (lower temperatures may of course be recorded over short timescales due to dynamic phenomena).

Chromosphere

At solar eclipse, it is sometimes possible to see a thin band of reddish light encircling the Sun. Latterly, a similar effect can be achieved artificially though the use of a coronagraph. This red light comes from the solar chromosphere, the atmospheric region directly above the solar photosphere. Just as the photosphere is named from the Greek word for light, the chromosphere is named for the Greek word for colour. This is because chromospheric visible emissions are dominated by the Balmer H-alpha line. The element helium, which is named after the Greek word for the Sun (remember the chariot), was discovered in 1868 due to the identification of its spectral line in chromospheric emission at a solar eclipse, and only discovered on Earth 27 years later.

The density and pressure of gas in the chromosphere continue to fall as one moves away from the centre of the Sun, however the temperature actually starts to increase again. This occurs at what is known as the chromospheric temperature minimum, around 600 km above the solar surface. This seems counter-intuitive — one would not normally expect something to become hotter further from the source of heat (the solar core). The chromosphere extends to a height of about 2 Mm above the solar surface, and the temperature rises from the 4,100 K recorded at the photospheric temperature minimum to about 20,000K.

Observations in the chromosphere, as elsewhere in the solar atmosphere, reveal that rather than being in a state of static homogeneity, it is in fact dynamic and non-uniform. One dynamic phenomenon of particular ubiquity in the chromosphere is the formation of solar spicules.

Spicules, as with other atmospheric structures, can be most easily observed on the solar limb. The first observations of limb spicules were made by Secchi (1877). On the limb, they are apparent as thin cylindrical structures of chromospheric material, which extend into the corona. They can be discerned primarily in the H_{α} line, but also in other strong chromospheric emission lines such as the H and K lines of ionised calcium. Spicules are found to occur at the boundaries of supergranules where tubes of intense magnetic flux are clustered.

Reported diameters of solar spicules have been reduced with improvements in the spatial resolution of instrumentation used to observe them. Lynch et al. (1973) found typical widths of 950 km but more recently Nishikawa (1988) found an average of 615 km. The width of the flux tubes with which spicules are associated remains at the edge of the ability of instruments to resolve, and it seems likely that some if not all of the widest spicules should be understood as bundles of thinner filaments, beyond the ability of current instrumentation to resolve.

Spicules can show group behaviour on a large scale, with ‘porcupine’ and ‘wheat-field patterns’ (Lippincott 1957). ‘Porcupine’ spicules seem to radiate from a common point below the limb, resulting in a dome structure over a spatial scale of ~ 18 Mm. ‘Wheat-field’ spicules seem to share the same orientation over a spatial scale of $\sim 14,000$ km. Given the strong link between spicules and intense flux tubes, such macroscale behaviour is almost certainly a manifestation of local magnetic field structure.

The transition region and corona

Above the chromosphere the temperature of the atmosphere, which you will recall increases through the chromosphere, increases by several orders of magnitude over a very short distance in what is known as the transition region. This transition region divides the chromosphere at about 8,000 K from the extremely tenuous corona, where temperatures are of the order of 1,000,000 K, Fig. 1.1. The exact temperature structure of the Sun's atmosphere remains a subject of some debate, and is discussed further in §2.1.

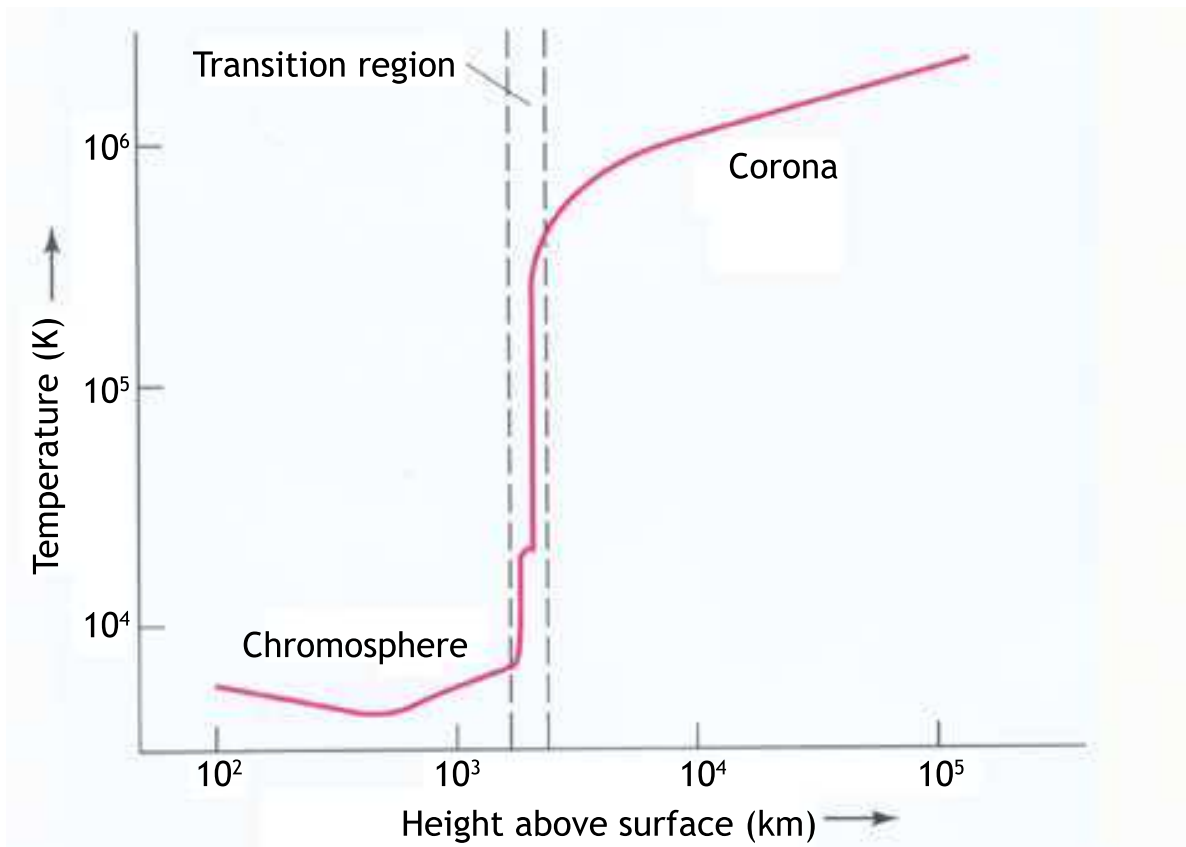


Figure 1.1: Plot of the solar atmospheric temperature profile highlighting the transition region (Sheung 2003)

The corona itself does not have a well defined ‘end’. It simply continues to become increasingly diffuse, and becomes the solar wind which ‘blows’ out into the wider solar system. Just as the chromosphere is ‘home’ to solar spicules, so the solar corona plays host to a variety of dynamic phenomena. The pressure of plasma in the corona is very low, and therefore

in regions of relatively strong magnetic field the plasma behaviour becomes field dominated. There is often a distinction drawn between regions of the Sun according to the strength and configuration of the local magnetic field. In ‘active regions’, the magnetic field is stronger, and it is in these regions that one would expect to see the more striking solar atmospheric structures, such as coronal loops, flares and mass ejections. Active regions are often associated with sunspots, where regions of strong magnetic field penetrate the solar surface.

Areas where the magnetic field strength is lower, on the other hand, are referred to as the ‘quiet Sun’.

1.2 Sun waves

It is possible to learn a great deal about an object by studying the oscillations it produces. If one hears someone pluck a guitar string, one does not need to see either them or their instrument to develop a good first hypothesis about what is happening. While it is nice to be able to work out on a purely auditory basis that there is a piano in the next room, or a set of bagpipes just across the glen, in such prosaic cases there is always the alternative of peering around the wall or climbing over the hill to check. Waves become rather more important as a diagnostic tool when it is not easily possible to otherwise observe the exact details of their source. On Earth, this need has given rise to the discipline of seismology. Although it is not possible to look deep inside the Earth’s mantle with a telescope, it certainly is possible to take measurements of the waves which traverse the Earth’s insides as a result of earthquakes and other violent events. By studying the way these waves travel, seismologists have been able to build up a detailed picture of the inside of our planet.

Just as it is impossible to see directly inside the Earth with a telescope, so it is impossible to see directly below the surface of the Sun. Light from below the solar surface (see §1.1.3) does not reach the Earth, and so cannot be used as a diagnostic tool. The impossibility of studying the inside of the Sun using direct visible light and telescopes is not the end of the story. Just as the idea of using seismology to study the Earth’s interior was inspired by earthquakes, so twentieth century solar physicists have been inspired to take advantage of the presence of naturally occurring waves on the Sun itself.

The first observational evidence of any oscillatory phenomena on the Sun was detected by Plaskett (1916), in the form of Doppler velocity fluctuations in measurements of the Sun's rotation rate. It was not entirely certain at the time whether these observations were true solar oscillations or the result of variations in the earth's atmosphere, but their solar origin was conclusively confirmed some years later by Hart (1954, 1956).

Subsequently, the first observations which showed definite oscillations of the solar surface, and therefore opened the real possibility of a new field of helioseismology, came from Leighton (1960). He measured vertical motions on the surface of the Sun with a dominant period of around 300 seconds, amplitudes of $300 - 400 \text{ ms}^{-1}$ and on a wide range of scales. This characteristic period of 300 seconds has since been confirmed many times, and these 5 minute waves are central to the work presented herein. The results presented by Leighton (1960) were the first measurements of the oscillations ubiquitous across the solar surface which are now referred to as solar *p* modes.

A decade after these first observations were made, Ulrich (1970); Leibacher & Stein (1971) proposed the explanation for these oscillations which has become generally accepted. These 5 minute oscillations are the result of standing acoustic waves in the solar interior.

Since then, detailed observations have been made of the solar *p* modes and have led to the discipline of helioseismology (Gough & Toomre 1991). Though the accuracy and resolution in time and space of measurements of *p*-mode oscillations has improved, power spectra still show a peak of ~ 300 seconds, 5 minutes. The *p* modes are resonant standing waves, which individually may have amplitudes closer to $\sim 1 \text{ ms}^{-1}$ than the initial observations of $300 - 400 \text{ ms}^{-1}$. As a result of superposition of acoustic perturbations travelling within a well defined spherical shell in the solar atmosphere, with upper and lower boundaries at turning points determined by the degree and order of the modes. The depth of the lower boundary can be investigated by analysing the behaviour of the modes, and varies a great deal for different modes. I do not intend to present the full history of helioseismology here — for an excellent review of helioseismology see Christensen-Dalsgaard (2002).

The upper boundary determines how close to the solar surface the modes are able to penetrate, and many modes have upper boundaries of their shells near the solar photosphere.

The p modes are subject to a region of evanescence around the photospheric temperature minimum, which inhibits direct propagation of the p modes into the solar atmosphere, but it is possible for modes to tunnel through this evanescent region and into the atmosphere (De Pontieu et al. 2003a, 2004, 2005; De Pontieu & Erdélyi 2006; Erdélyi 2006a).

1.3 Solar atmospheric wave propagation

The ubiquitous solar p modes are largely trapped within the solar interior by reflection near the solar surface. It would be tempting, therefore, to assume that oscillations observed in the higher solar atmosphere must have local explanations and could not be linked to the p modes. Having said this, signals with distinctive 5 minute periods are observed in the solar atmosphere all the way up to the corona (De Pontieu et al. 2003a,b, 2005), suggesting a possible link between photospheric modes and atmospheric waves.

De Pontieu & Erdélyi (2006) provide a review of possible linkages between oscillations in the lower atmosphere and those observed, in particular, in transition region moss (De Pontieu 2003). Moss is a highly structured and dynamic phenomenon initially observed by Peres et al. (1994) that can be seen in the extreme ultraviolet above active region plage, forming in the legs of hot, high pressure coronal loops. It was found (De Pontieu 2004; Ryutova & Shine 2004a,b; De Pontieu et al. 2003a) that a significant number of locations in a typical region of moss showed evidence of quasi-periodic oscillations. The typical oscillation period observed was 350 ± 60 seconds, and wave trains had a typical duration of 4–7 cycles. Crucially, De Pontieu et al. (2003b); De Pontieu (2004) showed a correlation between moss oscillations in the upper transition region, and oscillatory flows in the chromosphere. The explanation suggested for this correlation is that moss oscillations result from obscuration of EUV emission by quasi-periodic spicular flows.

This observational work is supported by numerical work (De Pontieu et al. 2004) demonstrating that photospheric oscillations propagating in regions of inclined magnetic field can generate non-linear shocks that are able to drive chromospheric spicule formation, providing a direct link between observed photospheric oscillations and 5 minute oscillations observed in the transition region. De Pontieu et al. (2005) suggest that the quasi-periodic shocks driven

by leakage of photospheric oscillations may also propagate into the lower corona, causing density and intensity oscillations such as have been observed by TRACE in 1 MK coronal loops, which have been identified as propagating magnetoacoustic slow modes. These coronal loop oscillations are also, like moss oscillations, associated with active region plage.

De Pontieu et al. (2005) also explore whether connectivity between the coronal and photosphere can be determined through a comparison of coronal oscillations and photospheric sources — a potential lower atmospheric seismology. Numerical simulation of signal propagation from various potential photospheric source locations as a driver of observed coronal oscillations was found to suggest ‘best-fit’ source locations in good correspondence with best guesses from visual inspection of TRACE imagery.

These results do not provide conclusive proof of the possibility of lower atmospheric seismology, but *suggest* that such analysis is possible. Further discussion of the literature on possible links can be found in Erdélyi (2006a,b).

These are not the only examples of suggested linkages between solar photospheric oscillations and oscillations in the upper atmosphere. Carlsson & Stein (1992) examined the generation of Ca K₂V bright points by upwards propagating acoustic shocks in the solar chromosphere, demonstrating that a sinusoidal 180 second period driver was able to produce observed results well. It has been suggested that 3 minute oscillations observed in the transition region are connected to the 5 minute global *p*-modes (Bogdan 2000; Zhukov 2002), and observational work by Marsh & Walsh (2006) has provided evidence of the propagation of oscillatory signals from the transition region into the solar corona in the 3 minute period band.

Leibacher et al. (1982) suggest that the observed chromospheric modes are the result of a chromospheric cavity, while Fleck & Schmitz (1991) contend that a cavity is unnecessary to explain the chromospheric oscillations, and that the correct explanation is the resonant excitation of the cut-off frequency at the temperature minimum, which is discussed further in §2.4.4.

1.3.1 Aim of this thesis

As detailed above, there is a substantial and ever growing literature concerned with the propagation of oscillatory signals from the photosphere into the upper regions of the solar atmosphere.

The equations of compressible magnetohydrodynamics (Alfvén 1942) are typically used to model the behaviour of the field embedded plasmas that make up the solar atmosphere. Due to the highly non-linear nature and intrinsic complexity of these equations, numerical simulations are often the only way to obtain an in-depth knowledge about macroscopic physical processes taking place in magnetised non-uniform turbulent plasmas (e.g. Chan et al. 1982; Nordlund 1985; Brandenburg 2003). The Sun is, at risk of repeating myself, a challengingly non-uniform and dynamic body to study, and even with substantial simplification and assumption it is typically not possible to directly address questions about signal propagation in the solar atmosphere through purely theoretical methods.

A great deal of work has been carried out examining the propagation of photospheric signals in regions of strong magnetic field where waves are to some extent guided by field lines (Bogdan et al. 2003; De Pontieu et al. 2004; Hasan et al. 2005; Hasan & van Ballegooijen 2008; Fedun et al. 2009). In this thesis, I look to extend this body of work by considering two dimensional simulations of wave propagation in a simulated equilibrium solar atmosphere embedded in a uniform vertical quiet Sun magnetic field. Before the magnetic case is addressed, it is instructive to examine the entirely non-magnetic case in order to achieve a better understanding of purely acoustic effects, and as an approximation to the quiet internetwork Sun.

Both the magnetic and non-magnetic case are approached through two-dimensional non-linear simulations. The simulations are carried out with a realistic background atmospheric stratification. The simulations are based on ideal gas assumptions and exclude radiative and non-LTE effects.

Chapter 2

Physics

2.1 The equilibrium

In this work, the propagation of driven acoustic waves, firstly in a non-magnetic stratified two-dimensional solar atmosphere, and secondly in a similar atmosphere in a uniform magnetic field, has been addressed. Previous studies have examined the effect of gravitational and temperature stratification on wave propagation in the solar corona (De Moortel & Hood 2003, 2004) and in a two isothermal layer model of the photosphere, chromosphere and corona (Chaouche & Abdelatif 2005) and demonstrated that gravitational and temperature stratification is crucial in understanding propagation of slow waves, which are somewhat analogous to acoustic waves, through the solar atmosphere. Also, work by O’Shea et al. (2006) has found observational evidence not only for outwardly propagating slow magnetoacoustic waves (in off-limb polar regions) but also have found evidence that such propagating waves are influenced by passage through some sort of resonant cavity.

It is therefore considered important that the model atmosphere used in the simulations is based closely upon accurate observationally derived models of the structure of the solar atmosphere, and that the simulations therefore fully include the effects on wave propagation of realistic atmospheric gravitational and temperature stratification.

The lower part of the initial profile of the first equilibrium implemented here is based on the VAL IIIc (Vernazza et al. 1981) atmospheric model. The temperature-height distribution in VAL IIIc is constructed to provide as close a match as possible to observed solar emission

spectra, and this temperature profile is the starting point in constructing a model atmosphere. There are, however, some differences between the method used in the construction of the VAL IIIc atmosphere and that which is being used to advect the model here. In particular, the VAL model includes a turbulent pressure term based on the existence of a varying microvelocity V . The numerical model used here does not include this term, and thus the temperature profile is an exact match to the VAL IIIc atmosphere while the pressure and density profiles are qualitatively similar but different in detail. Although the pressure and density depart somewhat from the VAL IIIc values, in the non-magnetic simulations the sound speed is the key parameter in determining the behaviour of driven propagating acoustic waves, and this depends entirely on the temperature. In the simulations presented in Chapter 7, the presence of magnetoacoustic modes makes the situation slightly more complicated. This is further discussed in §7.2.

The solar atmosphere is not described in VAL IIIc above 2.5 Mm, and therefore the upper part of the atmosphere is constructed based on McWhirter et al. (1975). In the same way as with the VAL IIIc based lower atmosphere, the temperature profile has been taken, adjusting the McWhirter et al. (1975) height scheme to be consistent with VAL IIIc, while the density and pressure are derived from this temperature profile and the condition of hydrostatic equilibrium.

VAL IIIc includes a temperature plateau in the transition region, on which the otherwise steep transition region temperature gradient drops towards zero. It is computationally challenging to maintain this feature in strict hydrostatic equilibrium in a simulated atmosphere. More importantly Fontenla et al. (1990) demonstrate that the inclusion of ambipolar diffusion in semi-empirical temperature modelling removes the need to include such a plateau, which is not a real solar feature. This plateau has therefore been smoothed out in the process of linking the VAL IIIc and McWhirter et al. (1975) temperature profiles.

The initial equilibrium atmosphere is constructed from the above detailed temperature profiles according to the condition of hydrostatic equilibrium

$$\frac{dp}{dz} = -\rho g, \quad (2.1)$$

where p is the kinetic gas pressure, z is vertical distance from the base of the atmosphere, ρ is mass density and g is gravitational acceleration.

The condition of hydrostatic equilibrium and the assumption of an ideal gas

$$\rho = \frac{mp}{k_B T}, \quad (2.2)$$

(for m the mean particle mass, T temperature and k_B Boltzmann's constant) are used to derive relations for pressure and density

$$\begin{aligned} p(z) &= p_0 \exp - \left(\int_0^z \frac{1}{\Lambda(z)} dz \right), \\ \rho(z) &= \rho_0 \frac{T_0}{T(z)} \exp - \left(\int_0^z \frac{1}{\Lambda(z)} dz \right), \end{aligned} \quad (2.3)$$

where Λ is the pressure scale height

$$\Lambda(z) = \frac{k_B T(z)}{mg}. \quad (2.4)$$

The stratification is thus completely determined by the semi-empirical temperature profile and the boundary parameter ρ_0 . ρ_0 is defined such that the density in the computational model at the height of the VAL IIIc temperature minimum is an exact match for the density at that height in the VAL IIIc model itself.

Unfortunately, there has been some contention in recent years as to what the temperature structure of the solar chromosphere actually is (Carlsson & Stein 1995; Ayres 1998, 2002; Kalkofen et al. 1999; Kalkofen 2001). The VAL IIIc (Vernazza et al. 1981) quiet Sun model, which has been extensively used in the past as a basis for quiet Sun modelling, has been called into question by the work of Carlsson & Stein (1995) that suggests strongly that the existence of a chromospheric temperature rise is chimerical. Carlsson & Stein (1995) suggest that the chromosphere is a fundamentally dynamic region which spends most of the time in a relatively cold state, but undergoing occasional shock heating. It is this shock heating, rather than the existence of a quasi-static equilibrium warm chromosphere, that produces the appearance of a temperature increase under the type of analysis used to construct such semi-empirical models as VAL.

Kalkofen (2001) has argued the counterpoint to this case, recognising that the chromosphere should be considered dynamic but arguing that there is still evidence of sustained chromospheric heating. Ayres (2002) on the other hand points out that there is evidence from

CO lines that the chromosphere has typical temperatures which are actually below those suggested by Carlsson & Stein (1995). Avrett (1996) recognises that the next generation of model stellar atmospheres needs to address the questions raised by the increasing sophistication of numerical modelling and observations which have allowed the gaps in previous models to be exposed.

This all begs the question of whether VAL IIIc is indeed an appropriate model to use in the numerical simulations of the non-magnetic solar chromosphere. The VAL IIIc model has been used as the basis for the chromosphere for the bulk of the work presented here, which gives an added advantage of increasing comparability with previous work based on this model. However, in recognition of the importance of the cold chromospheric hypothesis the key results (those using a 300 second harmonic driver) have been reproduced using a model with an isothermal chromosphere at $\sim 4,400$ K. This allows comparison between the ‘warm’ and ‘cold’ chromospheric cases.

2.2 The equations

The results presented here are primarily obtained through the use of numerical simulation. Of course, in order to be able to perform such computational exercises, one must first identify a set of mathematical equations that can be reasonably considered to describe the physical phenomena under investigation.

The magnetohydrodynamic (MHD) equations represent the mathematical environment most commonly used to describe the physics of the Sun’s corona and lower atmosphere, the region in which this work is interested. The MHD approximation applies to plasmas at macroscopic scales, scales at which the plasma can be treated as a neutral electrically conducting fluid. The MHD model combines Maxwell’s equations, which describe electrodynamic effects, with the Navier-Stokes equations for fluid dynamics. It is a model suited to considering large scale, non-relativistic phenomena.

The MHD approximation is justified for the simulations undertaken here, given the physical conditions found in the photosphere, chromosphere and corona. The treatment of the solar atmospheric plasma as macroscopically neutral is justified for phenomena such as are considered

here, which are on scales of the order 10^4 - 10^6 m. The Debye length in the solar atmosphere, the length scale on which local charge imbalances may result in a non-negligible electric field, is several orders of magnitude below this. Similarly, the period of the oscillatory phenomena we are investigating, and the timescales of the phenomena investigated in general, are substantially greater than the electron gyroperiod for solar atmospheric plasmas.

In the simulations presented herein, and hence in the equations below, the regions of the solar atmosphere in which we are interested are treated under the assumptions of an ideal gas. This means that radiative damping, magnetic diffusion, ohmic heating, etc. are ignored. The justification for ignoring these effects is not that they are in all cases negligible, as they may not be. Disregarding non-ideal effects substantially simplifies the numerical modelling and allows the diagnosis of the results to be very clearly focused on the specific phenomena that are under investigation.

This simplified approach may reduce the proximity of the results presented here to observed phenomena on the real Sun, but that does not necessarily mean that the results do not give insight into aspects of the propagation of solar surface oscillatory signals into the atmosphere. The specific case of short period signals that would be more heavily damped by non-ideal phenomena is discussed in Chapter 4.

2.2.1 The MHD equations

The MHD equations expressed in their ‘conservative’ form (note that they are not strictly in the conservative form as they are acted upon by an external gravitational field), read as follows:

$$\partial_t \rho + \nabla \cdot (\mathbf{v} \rho) = 0 \quad (2.5)$$

$$\partial_t (\rho \mathbf{v}) + \nabla \cdot (\mathbf{v} \rho \mathbf{v} - \mathbf{B} \mathbf{B}) + \nabla p = \rho \mathbf{g} \quad (2.6)$$

$$\partial_t e + \nabla \cdot (\mathbf{v} e - \mathbf{B} \mathbf{B} \cdot \mathbf{v} + \mathbf{v} p) = \rho \mathbf{v} \cdot \mathbf{g} \quad (2.7)$$

$$\partial_t (B) + \nabla \cdot (\mathbf{v} \mathbf{B} - \mathbf{B} \mathbf{v}) = 0 \quad (2.8)$$

$$p = (\gamma - 1) (e - \rho \mathbf{v}^2 / 2 - \mathbf{B}^2 / 2) \quad (2.9)$$

$$p_{tot} = p + \mathbf{B}^2 / 2 \quad (2.10)$$

in which ρ is the density, \mathbf{v} is the velocity vector, e is the total energy density per unit volume, \mathbf{B} is the magnetic field vector, p is the kinetic gas pressure, p_{tot} is the total (magnetic + kinetic) pressure, γ is the gas adiabatic index, and \mathbf{g} is the external gravitational field vector. The magnetic permeability, μ_0 , of the plasma is defined to unity. Eqn. (2.9) in the MHD system is the equation of state of an ideal gas, which connects the internal energy of the gas to its kinetic pressure.

Eqn. 2.5 encapsulates the conservation of mass, Eqn. 2.6 the conservation of momentum, Eqn. 2.7 the conservation of energy and Eqn. 2.8 the conservation of magnetic flux.

2.2.2 The HD equations

The results presented in Chapters 4, 5 and 6 come from ideal hydrodynamic simulations, i.e. simulations in which there is no magnetic field. This can be considered as a special case of the MHD equations in which $\mathbf{B} = 0$. The equations of ideal hydrodynamics then read as follows:

$$\partial_t \rho + \nabla \cdot (\mathbf{v} \rho) = 0 \quad (2.11)$$

$$\partial_t (\rho \mathbf{v}) + \nabla \cdot (\mathbf{v} \rho \mathbf{v}) + \nabla p = \rho \mathbf{g} \quad (2.12)$$

$$\partial_t e + \nabla \cdot (\mathbf{v} e + \mathbf{v} p) = \rho \mathbf{v} \cdot \mathbf{g} \quad (2.13)$$

$$p = (\gamma - 1) (e - \rho \mathbf{v}^2 / 2). \quad (2.14)$$

The hydrodynamic equations, which model a field free fluid, are used here as an approximation to the quiet Sun. In terms of modelling, the additional simplification of the system by removing magnetic terms provides advantages that compensate to some extent for the absence loss of the additional physics contained in the full MHD equations. The interpretation of non-magnetic results is also often more straightforward, as the fast, slow and Alfvén modes of the magnetic simulations are reduced to a single acoustic mode.

2.2.3 The altered MHD equations for the CD4 scheme

In the MHD simulations presented in this thesis, a fourth order central differencing scheme with numerical hyper-viscosity has been used, as detailed below in Chapter 3. As well as using a different numerical scheme from the hydrodynamic simulations, the MHD simulations solve

a modified set of equations in which the flow variables are split into background and perturbed terms.

Without loss of generality the variables ρ , e and \mathbf{B} can be split into their background components (the background components are assumed to be static in time, and in hydrostatic equilibrium) and perturbed components in the following way:

$$\rho = \tilde{\rho} + \rho_b, \quad (2.15)$$

$$e = \tilde{e} + e_b, \quad (2.16)$$

and

$$\mathbf{B} = \tilde{\mathbf{B}} + \mathbf{B}_b, \quad (2.17)$$

where $\tilde{\rho}$, \tilde{p} , \tilde{e} and $\tilde{\mathbf{B}}$ are the perturbed parts of the variables, and ρ_B , p_B , e_B and \mathbf{B}_b are the background parts of the variables. There is no need to split velocity, as the simulations being undertaken will not have background flows.

The condition of magnetohydrostatic equilibrium placed on the background variables can be expressed thus:

$$\nabla p_{kb} + \nabla \frac{\mathbf{B}_b^2}{2} - (\mathbf{B}_b \nabla) \mathbf{B}_b = \rho_b \mathbf{g}. \quad (2.18)$$

Taking the scalar product of Eqn. 2.18 with the velocity vector \mathbf{v} gives:

$$\left(\nabla p_{kb} + \nabla \frac{\mathbf{B}_b^2}{2} - (\mathbf{B}_b \nabla) \mathbf{B}_b \right) \cdot \mathbf{v} = \rho_b \mathbf{g} \cdot \mathbf{v}. \quad (2.19)$$

When Eqn. 2.18 and Eqn. 2.19 are subtracted from Eqn. 2.6 and Eqn. 2.7 (the momentum and energy equations), and diffusive source terms \mathbf{D} are added to the right-hand side of the equations, the system of MHD equations for an arbitrary perturbation of density, energy and

magnetic field can be written:

$$\frac{\partial \tilde{\rho}}{\partial t} + \nabla \cdot [\mathbf{v} (\rho_b + \tilde{\rho})] = 0 + D_\rho (\tilde{\rho}), \quad (2.20)$$

$$\begin{aligned} \frac{\partial[(\rho_b + \tilde{\rho}) \mathbf{v}]}{\partial t} &+ \nabla \cdot [\mathbf{v} (\rho_b + \tilde{\rho}) \mathbf{v} - \tilde{\mathbf{B}} \tilde{\mathbf{B}}] \\ &- \nabla \left[\tilde{\mathbf{B}} \mathbf{B}_b + \mathbf{B}_b \tilde{\mathbf{B}} \right] + \nabla \tilde{p}_t = \tilde{\rho} \mathbf{g} + \mathbf{D}_{\rho v} [(\tilde{\rho} + \rho_b) \mathbf{v}], \end{aligned} \quad (2.21)$$

$$\begin{aligned} \frac{\partial \tilde{e}}{\partial t} &+ \nabla \cdot [\mathbf{v} (e + e_b) - \tilde{\mathbf{B}} \tilde{\mathbf{B}} \cdot \mathbf{v} + \mathbf{v} \tilde{p}_t] \\ &- \nabla \left[(\tilde{\mathbf{B}} \mathbf{B}_b + \mathbf{B}_b \tilde{\mathbf{B}}) \cdot \mathbf{v} \right] \\ &+ p_{tb} \nabla \mathbf{v} - \mathbf{B}_b \mathbf{B}_b \nabla \mathbf{v} = \tilde{\rho} \mathbf{g} \cdot \mathbf{v} + D_e (\tilde{e}), \end{aligned} \quad (2.22)$$

$$\frac{\partial \tilde{\mathbf{B}}}{\partial t} + \nabla \cdot [\mathbf{v} (\tilde{\mathbf{B}} + \mathbf{B}_b) - (\tilde{\mathbf{B}} + \mathbf{B}_b) \mathbf{v}] = 0 + \mathbf{D}_B (\tilde{\mathbf{B}}), \quad (2.23)$$

and

$$\tilde{p}_t = (\gamma - 1) \left[\tilde{e} - \frac{(\rho_b + \tilde{\rho}) \mathbf{v}^2}{2} \right] - (\gamma - 2) \left(\mathbf{B}_b \tilde{\mathbf{B}} + \frac{\tilde{\mathbf{B}}^2}{2} \right). \quad (2.24)$$

Here p_{tb} denotes the total background pressure

$$p_{tb} = p_{kb} + \frac{\mathbf{B}_b^2}{2}, \quad (2.25)$$

which, in terms of background conservative variables, gives

$$p_{kb} = (\gamma - 1) \left(e_b - \frac{\mathbf{B}_b^2}{2} \right), \quad (2.26)$$

and

$$p_{tb} = (\gamma - 1) e_b - (\gamma - 2) \frac{\mathbf{B}_b^2}{2}. \quad (2.27)$$

This set of equations now describes the superposition of some perturbed state onto a background state that is in exact hydrostatic equilibrium. Any terms in which the background variables appear are multiplied by velocity or its derivative. If the background variables were to be set to zero, the canonical form of the MHD equations would be recovered.

2.3 MHD waves

In the hydrodynamic simulations that are presented in Chapters 4, 5 and 6, there is a single wave mode to be considered, the acoustic wave. Acoustic waves in these simulations propagate at the local sound speed which is dependent on the temperature in the model atmosphere.

In the simulations undertaken with a uniform magnetic field, the additional magnetic terms in the equations result in a more complicated dispersion relation. If one considers wave-like solutions of the MHD equations (ignoring gravity) in which perturbed quantities vary as $\exp[i(\mathbf{k} \cdot \mathbf{r} - \omega t)]$ then the dispersion relation for linear MHD perturbations can be determined to be (Stein & Leibacher 1974):

$$(\omega^2 - k^2 v_A^2 \cos^2 \theta) [\omega^4 - \omega^2 k^2 (v_A^2 + c_s^2) + k^4 v_A^2 c_s^2 \cos^2 \theta] = 0 \quad (2.28)$$

. Here, the Alfvén speed $v_A = \sqrt{\frac{B_0}{\rho_0}}$ (noting that the magnetic permeability is defined to one) and the sound speed $c_s = \frac{\gamma p}{\rho}$. This dispersion relation has three independent roots, corresponding to three different magneto-acoustic wave modes. The first and most obvious root is $\omega = kv_A \cos \theta$, which is the non-compressional Alfvén mode. Alfvén waves propagate parallel to the magnetic field at the Alfvén speed.

The other two solutions to the dispersion relation are $\omega = kv_+$ and $\omega = kv_-$, with the fast speed v_+ and slow speed v_- defined

$$v_{\pm} = \sqrt{\frac{1}{2} \left[v_A^2 + c_s^2 \pm \sqrt{(v_A^2 + c_s^2)^2 - 4v_A^2 c_s^2 \cos^2 \theta} \right]} \quad (2.29)$$

where θ is the angle between the wave vector and the magnetic field. These are, respectively, the fast- and slow-magnetoacoustic modes, and in all cases $v_+ \geq v_-$.

For propagation parallel to the magnetic field, in the strong magnetic field (low beta) case we find that the fast speed reduces to the Alfvén speed, and the slow speed to the sound speed. In the weak magnetic field (high beta) case, the fast speed reduced to the sound speed, and the slow speed to the Alfvén speed. Perpendicular to the field, the slow speed reduces to zero, while the fast speed increases to $v_+ = \sqrt{v_A^2 + c_s^2}$.

The presence of gravity is a complicating factor, but for oscillation frequencies above the Brunt-Väisälä frequency (the frequency of the characteristic buoyancy mode) does not fundamentally alter the nature of the three magnetic modes. As this thesis does not consider oscillations with periods much longer than the 5 minute period of the solar global p modes, the effect of gravity on fast and slow mode propagation, and indeed on acoustic mode propagation in the non-magnetic case, can be safely disregarded (Stein & Leibacher 1974). The prime impact of the gravitational field is not in altering the fundamental characteristics of the

waves, but in imposing a cut-off period on vertically propagating signals.

2.4 The solar atmospheric acoustic cut-off period

Lamb (1932) demonstrated that the propagation of acoustic waves in an unbounded medium was affected by an acoustic cut-off period (c.f. §2.4.1). Essentially, the theory predicts that acoustic waves in a gravitationally stratified atmosphere will only propagate if the wave period is less than the local acoustic cut-off period in the atmosphere. Any waves with longer periods will be evanescent in these areas. In addition to this, Lamb demonstrated that the cut-off frequency is the natural frequency of the atmosphere and that any acoustic disturbances imposed on such an atmosphere will trigger a response at the cut-off period. This work has been extended by, among others, Fleck & Schmitz (1991); Sutmann et al. (1998) who have examined analytically the isothermal case under various types of disturbances. Taroyan & Erdélyi (2008) extended this work for non-isothermal multi-layered plasmas.

It is theoretically predicted that in a stratified atmosphere, both in the case of a single excited propagating pulse (Rae & Roberts 1982) and of harmonic excitation (Fleck & Schmitz 1991; Kalkofen et al. 1994; Sutmann et al. 1998), a response at the natural acoustic cut-off period will be generated. In the case of a piston driver above the cut-off period, Fleck & Schmitz (1991); Kalkofen et al. (1994) showed in an isothermal case that the cut-off period oscillation has a higher growth rate due to stratification (De Moortel & Hood 2004) than the driven signal, and thus, at sufficient heights, comes to dominate. This result conforms to the expectation that a signal above the cut-off period will be evanescent and will be damped with height. In the case of a driver below the cut-off period, Kalkofen et al. (1994) found that a signal at the cut-off period is generated and that it experiences stratification driven growth at the same rate as the driven signal, but that the driven signal dominates at all heights.

Based on this body of work, it is to be expected that when the simulated solar atmospheres investigated in the work presented here are subjected to signals of any frequency, or to pulses, a signal at the cut-off period will also be generated. When a harmonic driver with a period above the cut-off period is applied, we expect to see the a strong resonant response that is likely to dominate the driver frequency.

2.4.1 Deriving the cut-off period - the Klein-Gordon equation

The cut-off frequency in a gravitationally stratified field free atmosphere can be derived in the following way (see e.g. Roberts (2004)). In an atmosphere stratified under a uniform gravitational acceleration g , the equilibrium pressure state can be described by the equation

$$p'_0(z) = -g\rho_0(z) \quad (2.30)$$

in which p is pressure, ρ is density, z is height and a dash signifies the derivative with respect to height.

In the special case of an ideal gas, we have

$$p_0 = \frac{k_B}{\hat{m}}\rho_0 T_0 \quad (2.31)$$

for the Boltzmann constant k_B and the mean molecular mass \hat{m} . Integrating Eqn. 2.30 with respect to height gives

$$p_0(z) = p_0 \exp -N_0(z), \quad (2.32)$$

$$\rho_0(z) = \rho_0(0) \frac{\Lambda_0(0)}{\Lambda_0(z)} e^{-N_0(z)}, \quad (2.33)$$

where $z = 0$ is some reference level,

$$\Lambda_0(z) = \frac{p_0(z)}{g\rho_0(z)} \quad (2.34)$$

is the pressure scale height and

$$N_0(z) = \int_o^z \frac{ds}{\Lambda_0} \quad (2.35)$$

is the integrated pressure scale height.

In the context of this vertically stratified atmosphere, we can suggest a perturbation to the equilibrium characterised by small motions in the z -direction, $\mathbf{u} = u(z, t)\mathbf{e}_z$. The linearised equations for such a small amplitude motions are

$$\frac{\partial \rho}{\partial t} = \frac{\partial \rho_0(z) u}{\partial z} = 0 \quad (2.36)$$

(a continuity equation);

$$p_0(z) \frac{\partial u}{\partial t} = -\frac{\partial p(z)}{\partial z} - g\rho(z) \quad (2.37)$$

(a momentum equation); and

$$\frac{\partial p}{\partial t} + p'_0(z) u = c_s^2(z) \left(\frac{\partial \rho(z)}{\partial t} + \rho'_0(z) u \right) \quad (2.38)$$

(an isentropic energy equation), where $c_s(z) = (\gamma p_0(z) / \rho_0(z))^{\frac{1}{2}}$ is the sound speed with γ the adiabatic index and $p(z, t)$ and $\rho(z, t)$ are the variation in pressure and density respectively.

These three equations imply

$$\frac{\partial^2 u}{\partial t^2} = c_s^2(z) \frac{\partial^2 u}{\partial z^2} + \frac{1}{\rho_0} (\rho_0 c_s^2)' \frac{\partial u}{\partial z}, \quad (2.39)$$

and by introducing the variable Q such that

$$u(z, t) = \left[\frac{\rho_0(0) c_s^2(0)}{\rho_0(z) c_s^2(z)} \right]^{\frac{1}{2}} Q(z, t), \quad (2.40)$$

it becomes apparent that the vertical propagation of a signal in a gravitationally stratified atmosphere leads us to the Klein-Gordon equation

$$\frac{\partial^2 Q}{\partial t^2} - c_s^2(z) \frac{\partial^2 Q}{\partial z^2} + \Omega_s^2(z) Q = 0, \quad (2.41)$$

where Ω_s , defined by

$$\Omega_s^2(z) = \frac{c_s^2(z)}{4\Lambda_0^2} [1 + 2\Lambda'_0(z)], \quad (2.42)$$

is the acoustic cut-off frequency, giving a cut-off period of

$$P(z) = \sqrt{\frac{4\Lambda_0^2}{c_s^2(z)} \left[\frac{2\pi}{1 + 2\Lambda'_0(z)} \right]}. \quad (2.43)$$

In an isothermal atmosphere, this reduces to

$$P(z) = \frac{4\pi\Lambda_0}{c_s(z)}. \quad (2.44)$$

2.4.2 A multitude of cut-off frequencies

Schmitz & Fleck (1998) point out that it is possible to calculate alternative values for the cut-off period in a gravitationally and temperature stratified atmosphere to the value resulting from the above derivation.

They derive four different expressions for the cut-off frequency present in the existing literature by considering the wave equations for the displacement and the Lagrangian pressure

perturbation and transforming the independent and dependent variables. All of the forms include as a term the cut-off frequency of an isothermal gravitationally stratified atmosphere,

$$\omega_0 = \frac{\gamma g}{2c_s}. \quad (2.45)$$

The first derivation, from the displacement equation

$$c_s^2 \frac{d^2\xi}{dz^2} - \gamma g \frac{d\xi}{dz} + \omega^2 \xi = 0 \quad (2.46)$$

yields the expression

$$\omega_1^2 = \omega_0^2 + \frac{\gamma g}{2c_s^2} \frac{dc^2}{dz}, \quad (2.47)$$

which is equivalent to Eqn. 2.43.

If, however, one starts with the equation of the Lagrangian pressure perturbation

$$c_s^2 \frac{d^2\Delta p}{dz^2} + \left[\gamma g + \frac{dc_s^2}{dz} \right] + \omega^2 \Delta p = 0 \quad (2.48)$$

one can obtain the alternative expression

$$\omega_2^2 = \omega_0^2 - \frac{1}{4c_s^2} \left(\frac{dc_s^2}{dz} \right)^2 + \frac{1}{2} \frac{d^2c_s^2}{dz^2}, \quad (2.49)$$

which also represents a cut-off frequency. Schmitz & Fleck (1998) suggest that this second expression represents a cut-off frequency due to the temperature gradient, as ω_2 is non-zero if $g = 0$. Due to the special nature of the equation of state for an ideal gas, and the condition of hydrostatic equilibrium $\frac{dp}{dz} = -\rho g$, the expression for ω_1 contains only the first derivative of the sound speed. The frequency ω_2 , however, is dependent on the second derivative, which makes the expression extremely sensitive to the fine detail of the local atmospheric structure. In particular, calculating the second derivative in the transition region is subject to unlimited uncertainties, given the very strong gradients in temperature and hence sound speed that exist there.

This problem also applies to the third and fourth formulations presented for the cut-off frequency. The third formulation, derived through transforming the independent variable z to a time-like variable $\tau = \tau(z)$ such that $dz = c_s(z)d\tau$ (Lamb 1909), and considering the Eulerian displacement, is

$$\omega_3^2 = \omega_0^2 + \frac{\gamma g}{2c_s^2} \frac{dc_s^2}{dz} + \frac{3}{16c_s^2} \left(\frac{dc_s^2}{dz} \right)^2 - \frac{1}{4} \frac{d^2c_s^2}{dz^2}. \quad (2.50)$$

The fourth and final frequency presented by Schmitz & Fleck (1998), based on the τ transformation and the Lagrangian pressure perturbation, is

$$\omega_3^2 = \omega_0^2 - \frac{1}{16c_s^2} \left(\frac{dc_s^2}{dz} \right)^2 + \frac{1}{4} \frac{d^2 c_s^2}{dz^2}. \quad (2.51)$$

Schmitz & Fleck (1998) comment that the belief seems widespread in the literature that the behaviour, oscillatory or otherwise, of a signal with a given period is entirely determined by whether this period is longer or shorter than the cut-off period described above (Eqn. 2.43). This direct interpretation is clearly problematic insofar as the several cut-off frequencies do not necessarily coincide, and hence one might obtain different expectations of oscillatory behaviour through consideration of the different ω_i . They suggest that a period below the cut-off period is a necessary condition of oscillatory behaviour, but not necessarily a sufficient one - there may be cases where the signal period is below the local cut-off period but nevertheless there is a non-oscillatory solution.

Comparing the four cut-off frequencies in the case of the VAL IIIc atmosphere, Schmitz & Fleck (1998) find that the different frequencies are similar in zones of relatively gentle gradients (as behaviour is dominated by the common ω_0 term). However, at the temperature minimum, they find that the $\omega_{1,3}$ solutions are very different to the $\omega_{2,4}$ solutions - while $\omega_{1,3}$ are increased by the local gradients, $\omega_{2,4}$ both decrease.

It is also worth remembering in the discussion of cut-off frequencies that mathematically an oscillatory solution on an interval $[a, \infty)$ refers to a solution with an infinite number of zeroes on this interval. There can be a non-oscillatory solution with a finite number of zeroes on such an interval, and it follows that on a finite interval such as is considered in the numerical work presented here, a non-oscillatory solution might in principle have very similar properties on a finite computational interval to an oscillatory one. In other words, one might find a quasi-oscillatory solution even above the cut-off period on a finite computational domain.

In this work the form derived in §2.4.1, equivalent to ω_1 , is always being referred to when the cut-off frequency (or more often period) is discussed in relation to the numerical results. This is in line with the treatment of the cut-off frequency in much of the literature. It is worthy of note, however, that some papers (Mosser 1995; Balmforth & Gough 1990, e.g.) consider either ω_2 or ω_3 more appropriate. The choice of ω_1 here is made with the justification that

the other forms presented all include terms in the second derivative of c_s^2 (equivalently the second derivative of temperature or of pressure scale height). As Schmitz & Fleck (1998) point out, these second derivative terms cannot be calculated without unlimited uncertainty in the transition region - and this is a region of vital interest to us here.

The cut-off frequency remains a useful and intrinsically important parameter to the discussion of signal propagation in the solar lower atmosphere. It must, however, be recognised that any single formulation should be considered as a useful indicator of signal behaviour rather than a definitive exact value at which signal behaviour is entirely and immediately transformed.

2.4.3 Cut-off in VAL IIIc

Applying Eqn. 2.44, the equation for the cut-off period in an isothermal atmosphere, to the VAL IIIc based temperature profile used in the simulations presented herein gives the dashed line in Fig. 2.1, which is uniformly increasing from the temperature minimum in line with the temperature.

In this study, however, the atmosphere is not isothermal, with particularly strong temperature gradients in the transition region (a region of particular interest to us). As discussed above, a term in the gradient of the scale height must be included for the cut-off period to be a useful diagnostic parameter.

This cut-off, ω_1 as defined by Eqn. 2.43, is illustrated by the solid line in Fig. 2.1. Crucially, it is apparent that this cut-off period is not uniformly increasing, but includes local minima. This is the cut-off period used to inform physical interpretations of dynamics in the lower solar atmosphere. The non-stratified isothermal cut-off period is included for comparison and to emphasise the importance of including thermal stratification in the calculation of the cut-off period when considering this region of the Sun.

Although the cut-off frequency varies to some extent on small scales, the atmosphere may be divided into four distinct key regions for the purposes of analysing the results: first the photosphere around the temperature minimum, in which the cut-off period is below 300 seconds and thus 5 minute oscillations will be evanescent; second the chromosphere in which the cut-off period increases to a value slightly above 300 seconds, and therefore any signal of period 5

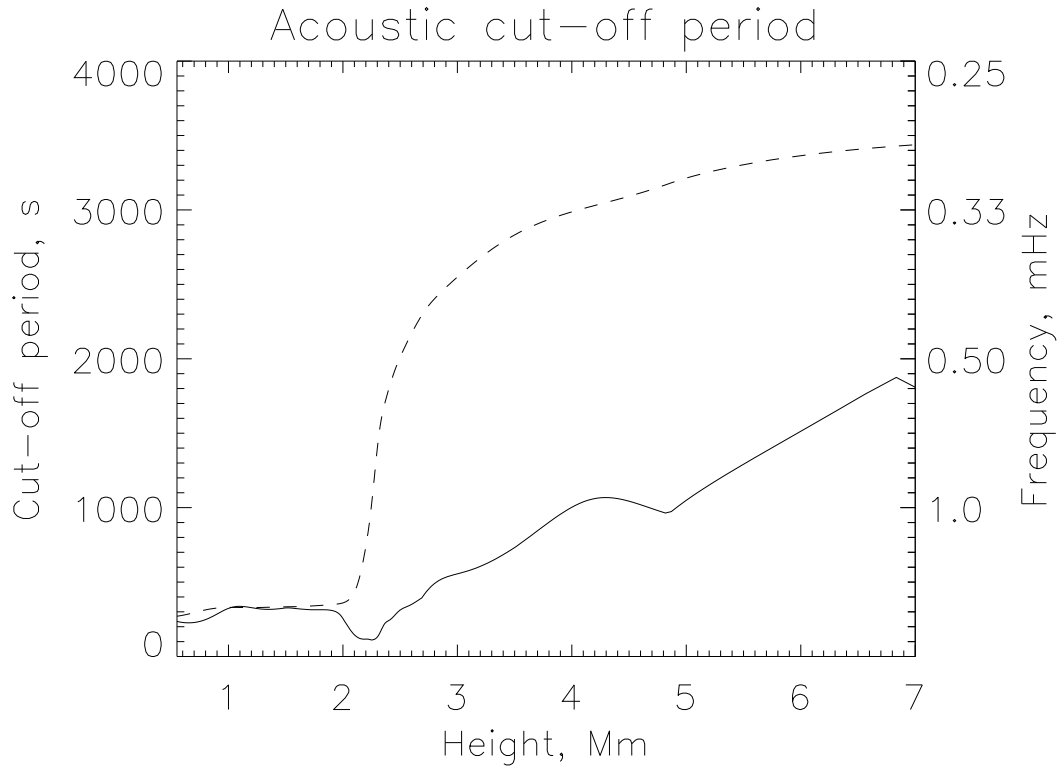


Figure 2.1: Variation in cut-off period with changing height ignoring stratification (dashed line) and including stratification (solid line) for a VAL IIIc solar atmosphere.

minutes or less will propagate; thirdly a zone around the transition region in which the cut-off period drops to a much lower value, perhaps as low as 100 seconds, over a height range of about 400 km; fourthly the corona in which the cut-off period again becomes sufficiently long that waves at all of the periods being considered here will propagate freely.

From Fig. 2.1 it is apparent that the cut-off period rises from ~ 300 seconds in the chromosphere to > 1500 seconds in the corona. However, in the transition region because of the strong temperature stratification it drops to < 150 seconds. This drop is of great importance to the study of propagation through the transition region, and demonstrates the importance of using realistic temperature profiling if the transition region is to be properly modelled. Also, at 200 km (where the 300 second driver is applied), the cut-off period is below 300 seconds, and the minimum cut-off period that signals pass through in the photosphere is ~ 210 seconds. The

important 5-minute oscillations are therefore evanescent in the photosphere but could tunnel through it to reach the chromosphere. This tunnelling occurs for the oscillation to traverse the distance from the driver application height to the propagative region.

The coronal values of the cut-off frequency are adequately high that there is no potential for signals to be evanescent in the corona, and as mentioned above signals oscillating below the cut-off period generate only insignificant amplitudes of resonant excitation at the cut-off.

2.4.4 Resonance and reflection

Resonant excitation at the cut-off frequency is not the only mechanism limiting transmission of energy into the corona. Partial reflection of acoustic waves at all frequencies is expected at the transition region, with a frequency dependent coefficient of reflection. It exhibits sufficiently large gradients in density and pressure that it approximates to a density discontinuity, with lower sound speed below and higher sound speed above. The transition region delineates the upper boundary of the ‘chromospheric cavity’ which has been previously suggested as the source of 3-minute transition region oscillations (Leibacher et al. 1982).

Fleck & Schmitz (1991) argue that it is unnecessary to invoke the ‘chromospheric cavity’ to explain the generation of the 3-minute chromospheric signals. As demonstrated above (c.f. Fig. 2.1), the cut-off period in the photosphere/lower chromosphere drops below five minutes. In particular, Fleck & Schmitz (1991) point out that the cut-off period at the temperature minimum falls towards three minutes. Fleck & Schmitz (1991) argue that rather than having to invoke (Leibacher et al. 1982, e.g.) a chromospheric cavity to explain chromospheric three minute oscillations, they can be fully explained by the resonant excitation of the cut-off mode at the photospheric temperature.

This assertion is supported by analytical and numerical modelling of piston driven waves in an isothermal (temperature as at the temperature minimum) plane atmosphere, and by numerical modelling with the VAL IIIc atmosphere (Fleck & Schmitz 1991). They find in this modelling that the driven frequency is dominant up to ~ 1000 km, above which the resonant mode becomes dominant.

In terms of the transport of energy from the solar interior to the higher atmosphere, long

period evanescent waves will transfer significant energy to modes at the cut-off frequency, whereas short period propagating waves will transfer little energy to cut-off frequency modes. The cut-off period might be expected to limit transmission of long period power from the solar surface into the corona.

Analytical work by Fleck & Schmitz (1991) predicts that as the time tends to infinity in a simple atmosphere with a cut-off period shorter than the driver period, the driver period will eventually become dominant over the resonance. The photospheric p -modes being considered here are normally coherent over about 5 or 6 periods (< 1800 seconds). It is not immediately clear whether this represents a long enough time for the driver frequency to become dominant in the simulations, or for that matter whether the results for the simple atmosphere considered by Fleck & Schmitz (1991) should be expected to be applicable to the stratified equilibrium atmosphere modelled here.

2.4.5 Cold chromosphere

In Chapter 4 a model with an isothermal chromosphere is considered alongside the VAL IIIc case. It is noted that the cut-off period for this cold chromospheric model is similar to the VAL IIIc case (c.f. Fig. 2.1, but with a cut-off period in the photosphere and chromosphere which is constant and a little below 300 seconds (at ~ 270 seconds). This cold chromospheric atmosphere of course does not have a temperature minimum and therefore has no corresponding minimum in cut-off period.

2.4.6 Magnetic field

The presence of a magnetic field may modify the cut-off period in a gravitationally and thermally stratified atmosphere. Bel & Leroy (1977) demonstrate for an isothermal atmosphere that for waves propagating parallel to the gravitational field, if the magnetic field is also parallel to the gravitational field, it is possible to obtain the standard expression (Lamb 1932) for the cut-off period, i.e. Eqn. 2.44. Where, however, the magnetic field is at an angle θ to the gravitational field, they find that (in the isothermal case) the cut-off period is substantially increased. For instance, a magnetic field at an angle $\frac{\pi}{4}$ to the gravitational field is found to increase the cut-off period by a factor of ~ 1.4 .

De Pontieu et al. (2004); Cally (2006); Schunker & Cally (2006) similarly demonstrate for a non-isothermal atmosphere that an inclined ('ramped') magnetic field results in an increased cut-off period, showing for instance that, with appropriately inclined field, the 'ramp cut-off period' may increase such that signals that would otherwise be entirely evanescent may become entirely propagative.

In the discussions presented here, it is felt that it is justified to disregard any effect of the magnetic field on the cut-off period. Firstly, in the magnetic simulations presented in Chapter 7, the magnetic field is uniform vertical in its equilibrium state. While the driven disturbances applied to the atmosphere do result in some dynamic departure from the strictly vertical, the magnitude of the horizontal component of the field remains negligible even at its maximum values. The impact of magnetic field on the cut-off comes primarily in the case of a strongly inclined field (Bel & Leroy 1977; De Pontieu et al. 2004; Cally 2006; Schunker & Cally 2006). Secondly, Bel & Leroy (1977) point out that the effect of the magnetic field on the cut-off is limited in the case that $\beta \gg 1$. In Chapter 7, the entire domain is described by a high-beta regime, and hence one would not expect substantial impact of the cut-off on the magnetic field.

Chapter 3

Numerics

3.1 Introduction

The results presented in Chapters 4, 5, 6 and 7 come from forward modelling performed using numerical codes designed to solve systems of partial differential equations. There are several limiting factors on the results obtained through this type of modelling. Firstly, the modelling is limited by the power of the computers on which it is performed. Modern single processors can perform billions of additions a second, but even so performing a simulation upon a grid of the sort considered in this thesis, for the simulation timescales addressed here, could take several days on a single processor. Where parameters, or even the code itself, need to be refined, several successive iterations of a simulation can be very time consuming.

The availability of powerful multi-node computers has the potential to substantially reduce the time taken to perform such runs. In this thesis, three supercomputers were used to obtain results. First was the Titania machine on the White Rose Grid, second the Iceberg machine that replaced it and third the MHD Cluster machine that resides at St Andrews. On these machines, arrays of 4, 8 or more nodes are potentially available. With a properly parallelised code, this can result in substantial saving, but time never scales precisely with number of nodes - parallel processing introduces its own overheads. There are also increased risks of downtime when using such machines. Nevertheless, sets of results presented in Chapter 7 were able to be produced in just a few hours. Of course, it can still take many runs before the correct combination of parameters for an adequately stable run are identified.

The stability of the code is another great challenge in numerical modelling. In this work, for instance, the magnetic simulations represented a very significant challenge in terms of code stability, with exponentially growing false signals being generated at the upper boundary of the domain even in the simulations that are presented herein. Such unphysical signals can mask real results, and will normally swiftly crash a code once they grow to adequate amplitude. Issues of stability are discussed further in the text below for different numerical approaches.

Finally in this section, a comment on boundary conditions. The solar atmosphere is not subject to arbitrary boundaries – however, numerical simulations are. At the top, bottom, left and right of the simulated environment, some mathematical condition must be applied. Ideally, this condition will provide a zero magnitude of signal reflection from the boundary, i.e. signals will be able to propagate ‘out of the box’. During this research, a substantial amount of work was invested in looking to adapt the method of characteristics for determining boundary values to be compatible with the VAC. Unfortunately, the early results of using this method, based on testing in 1D, suggested that the benefits compared to application of simple ‘continuous’ boundary conditions as defined in the VAC were minor or non-existent, in exchange for a non-negligible computing overhead. The effort was therefore discontinued.

The ‘SAC’ simulations presented in Chapter 7 suffered from significant reflection at the upper boundary. This was managed over the timescales presented by adding an additional 8 Mm unphysical layer above the McWhirter corona, broadly mirroring in temperature profile the physical lower 8 Mm of the model atmosphere. The effect of this was to add a substantial transmission time for signals propagating out of the corona to reach any point of reflection. Nevertheless, although it was broadly effective, it is hardly an elegant solution and doubling the computational domain greatly increases simulation time.

These issues with the numerical modelling are noted in passing to contextualise the work presented below, and as a reminder that in practice computational modelling is rarely as simple as one might like it to be.

3.2 Numerical (M)HD

This section is informed by course notes from Tóth (1998) which are available online courtesy of the author. The ideal equations of MHD are a set of hyperbolic partial differential equations (with the ideal hydrodynamic equations representing a special case where $\mathbf{B} = 0$). As the equations are hyperbolic, they have wave-like solutions that propagate with no dissipation; slow, fast and Alfvén waves. The MHD equations can be written in the form

$$\partial_t \mathbf{U} + \partial_i \mathbf{F}_i(\mathbf{U}) = \mathbf{S}(\mathbf{U}) \quad (3.1)$$

where \mathbf{U} contains the conservative variables, \mathbf{F} contains the fluxes, \mathbf{S} contains source terms and i indexes the spatial dimensions.

Such a system of equations may be spatially discretised in various ways for computational solution, each possibility giving advantages and disadvantages.

3.2.1 Finite differences

One potential method of spatial discretisation is by the finite difference method (FDM). In a finite difference discretisation, the flow variables \mathbf{U} are assigned values \mathbf{U}_j pointwise at a set of locations x_j . It is then possible to approximate spatial derivatives of the variables at any given point by using difference formulae derived from Taylor expansions around the points. In the case of a 1D uniform grid with a spacing δx a first order spatial derivative might be calculated thusly:

$$\frac{\mathbf{U}_{j+1} - \mathbf{U}_{j-1}}{2\delta x} = \frac{1}{2\delta x} \left[\mathbf{U}_j + \delta x \partial_x \mathbf{U} + \frac{(\delta x)^2}{2!} \partial_{xx} \mathbf{U} + \dots \right] \quad (3.2)$$

$$- \left[\mathbf{U}_j - \delta x \partial_x \mathbf{U} + \frac{(\delta x)^2}{2!} \partial_{xx} \mathbf{U} + \dots \right]$$

$$= \partial_x \mathbf{U} + O((\delta x)^2) \quad (3.3)$$

The advantage of the FDM is that it is simple, the disadvantage is that there is no unique definition of FDM on unstructured grids, and no guarantee of conservation of quantities on non-uniform grids.

3.2.2 Finite volumes

In a finite volume discretisation, rather than giving the variables point-wise evaluations, space is divided somehow into cells and the average value of variables \mathbf{U} are known in each cell j ,

$$\mathbf{U}_j(t) = \frac{1}{V_j} \int_{V_j} \mathbf{U}(\mathbf{x}, t) d\mathbf{x}, \quad (3.4)$$

for cell volume V_j . In such a method the fluxes through all cell interfaces are added to and subtracted from the existing cell averages, which has the benefit of automatically giving a conservative discretisation for any arbitrary grid. The disadvantage of a finite volume approach is that it becomes difficult to go higher than second order spatial accuracy.

3.2.3 Finite elements

The finite elements type of discretisation gives the variables \mathbf{U} nodal values at the gridpoints x_j , while approximating \mathbf{U} with a linear combination of localised interpolating polynomials f_j elsewhere,

$$\bar{\mathbf{U}}(\mathbf{x}, t) = \sum_j \mathbf{U}_j(t) f_j(\mathbf{x}). \quad (3.5)$$

The advantage of finite element schemes is the ability to achieve high order accuracy on arbitrary grids by the use of high order interpolating polynomials. The disadvantage is that it is rather complicated, requires inversion of large linear systems even with explicit time integration, and is vulnerable to discontinuities.

3.2.4 Total variation diminishing schemes

One set of schemes which are popular in the solution of hyperbolic systems of PDEs are total variation diminishing (TVD) schemes, as used for instance by Ryu et al. (1995). There are many variations on the theme of TVD schemes, but they are based around a common concept.

In one spatial dimension, for some linear system of hyperbolic equations or for a single non-linear hyperbolic equation it can be shown that the total variation

$$TV(U) = \sup \sum_{j=1}^{N-1} |\mathbf{U}(x_{j+1}) - \mathbf{U}(x_j)| \quad (3.6)$$

of the analytical solution does not increase in time. The analytical supremum is taken over all possible subdivisions of the spatial dimension.

Computational TVD schemes are designed to ensure that the discrete version of Eqn. 3.6 does not increase from one time step to the next,

$$\sum_j |\mathbf{U}_{j+1}^{n+1} - \mathbf{U}_j^{n+1}| \leq \sum_j |\mathbf{U}_j^n - \mathbf{U}_j^n|. \quad (3.7)$$

The MHD equations are actually non-linear, and computational modellers are typically interested in more than one dimension, in this thesis for instance we consider 2D simulations. Nevertheless, schemes which are based on the TVD property tend to perform well near discontinuities, with a very low level of spurious oscillation generated, and are therefore appealing. The disadvantage of the TVD property is a spatially first order representation of smooth local maxima and minima.

The hydrodynamic results presented in this thesis have been carried out using a TVD Lax-Friedrichs (TVDLF) numerical scheme (Nessyahu & Tadmor 1990). This is the simplest type of TVD scheme, and it discretises a conservation law by

$$\mathbf{U}_j^{n+1} = \mathbf{U}_j^n - \frac{\Delta t}{\Delta x} (\mathbf{F}_{j+1/2} - \mathbf{F}_{j-1/2}) + \frac{1}{2} (\Phi_{j+1/2} - \Phi_{j-1/2}), \quad (3.8)$$

where

$$\mathbf{F}_{j+1/2} = \frac{\mathbf{F}_j + \mathbf{F}_{j+1}}{2} \quad (3.9)$$

$$\Phi_{j+1/2} = \mathbf{U}_{j+1} - \mathbf{U}_j. \quad (3.10)$$

The last two terms in Eqn. 3.2.4 add a numerical diffusion term of the form $\nu \nabla^2 \mathbf{U}$ in which the diffusion coefficient $\nu \propto (\Delta x)^2 / \Delta t$. The TVD Lax-Friedrichs scheme is hence only first order accurate, however the numerical diffusion can be reduced by including a diffusive flux term

$$\Phi_{j+1/2} = \frac{\Delta t}{\Delta x} c_{j+1/2}^{\max} (\mathbf{U}_{j+1} - \mathbf{U}_j) \quad (3.11)$$

in which the Courant number $\frac{\Delta t}{\Delta x} c_{j+1/2}^{\max}$, in which $c_{j+1/2}^{\max}$ is the maximum wave speed, is used as a coefficient on the artificial diffusion.

The numerical flux terms Φ can be interpreted as modifying the centred flux difference formula to a one sided upwinded difference formula. This upwinding is only exact for a single

linear equation, while for a whole system of equations the upwinding is only approximate. Nevertheless, it seems appropriate to introduce some element of upwinding for hyperbolic systems of equations, as in such equations information should propagate from the upstream direction.

It is possible to achieve second order spatial accuracy in the TVDLF scheme by using a linear approximation of \mathbf{U} at the boundary interfaces. The interface values can be extrapolated from the left and right cell centre values

$$\mathbf{U}_{j+1/2}^L = \mathbf{U}_j^n + \frac{1}{2}\Delta\bar{\mathbf{U}}_j^n, \quad (3.12)$$

$$\mathbf{U}_{j+1/2}^R = \mathbf{U}_{j+1}^n - \frac{1}{2}\Delta\bar{\mathbf{U}}_{j+1}^n, \quad (3.13)$$

where $\Delta\bar{\mathbf{U}}$ denotes slopes limited by some condition. The interface fluxes then become

$$\mathbf{F}_{j+1/2} = \frac{\mathbf{F}(\mathbf{U}_{j+1/2}^L) + \mathbf{F}(\mathbf{U}_{j+1/2}^R)}{2} \Phi_{j+1/2} = \frac{\Delta t}{\Delta x} c_{j+1/2}^{\max} (\mathbf{U}_{j+1/2}^R - \mathbf{U}_{j+1/2}^L). \quad (3.14)$$

In this second order scheme the diffusive flux Φ is greatly reduced. This spatially second order TVDLF scheme is the one used in the hydrodynamic simulations presented in this thesis.

The spatially second order TVDLF scheme is made temporally second order by the utilisation of Hancock's predictor step. A time-centred value of \mathbf{U} is calculated

$$\mathbf{U}_j^{n+1/2} = \mathbf{U}_j^n - \frac{1}{2} \frac{\Delta t}{\Delta x} \left[\mathbf{F} \left(\mathbf{U}_j^n + \frac{1}{2} \Delta\bar{\mathbf{U}}_j^n \right) - \mathbf{F} \left(\mathbf{U}_j^n - \frac{1}{2} \Delta\bar{\mathbf{U}}_j^n \right) \right], \quad (3.15)$$

and then this time-centred value is used to calculate linear extrapolations

$$\mathbf{U}_{j+1/2}^L = \mathbf{U}_j^{n+1/2} + \frac{1}{2} \Delta\bar{\mathbf{U}}_j^n \mathbf{U}_{j+1/2}^R = \mathbf{U}_j^{n+1/2} - \frac{1}{2} \Delta\bar{\mathbf{U}}_j^n. \quad (3.16)$$

The slope limiter used in the HD simulations presented in this thesis is the Woodward (or monotonised central difference) slope limiter, in which

$$\Delta\bar{\mathbf{U}}_j = \text{minmod} \left(2\Delta\mathbf{U}_{j-1/2}, 2\Delta\mathbf{U}_{j+1/2}, \frac{1}{2}\Delta\mathbf{U}_{j-1/2} + \frac{1}{2}\Delta\mathbf{U}_{j+1/2} \right). \quad (3.17)$$

The hydrodynamic simulations presented here are thus performed using a spatially and temporally second order TVDLF scheme using a Woodward slope limiter and a Hancock predictor step.

3.3 HD simulations

In the simulations discussed in Chapters 4, 5 and 6, the second order TVDLF scheme is implemented through the Versatile Advection Code (Tóth 1996). The equations advected by the scheme are (c.f. §2.11):

$$\partial_t \rho + \nabla \cdot (\mathbf{v} \rho) = 0, \quad (3.18)$$

$$\partial_t (\rho \mathbf{v}) + \nabla \cdot (\mathbf{v} \rho \mathbf{v}) + \nabla p = \rho \mathbf{g}, \quad (3.19)$$

$$\partial_t e + \nabla \cdot (\mathbf{v} e + \mathbf{v} p) = \rho \mathbf{v} \cdot \mathbf{g}, \quad (3.20)$$

$$p = (\gamma - 1) (e - \rho \mathbf{v}^2 / 2). \quad (3.21)$$

The time discretisation is based on a Courant parameter of 0.8. The simulation domain is 8 Mm wide and 8 Mm high, with a resolution of 200×510 grid points (plus boundary layers at each edge two grid points wide). The grid points are positioned on a mesh that is vertically stretched, with highest resolution at the transition region, and significantly lower resolution in the corona. The areas of higher resolution match those areas of the domain which are associated with the highest gradients. The mesh is not adaptive in time, but the area of highest gradient (i.e. the transition region) does not in general move so significantly in space, nor is it so exactly matched to the equilibrium case, in any of the simulations that the mesh becomes problematic.

All of the boundary layers are given boundary conditions of the form $du_j/dx_i \equiv 0$, where u_j are the flow variables and i indexes the direction to which the boundary is perpendicular. These boundary conditions allow disturbances to propagate out of the computational domain with negligible reflection in the simulations described here.

Low gravity regions (De Pontieu 1996; James 2004) are implemented at the higher and lower extents of the computational domain in order to prevent downflows from developing with the use of open boundaries. Data from within these low gravity regions are considered unphysical and are not included in the analysis. Except in these regions, it is a reasonable simplification to treat gravity as a constant over the domain which extends for only $\sim 1\%$ of a solar radius. Gravity is taken as 274 m s^{-2} .

The lower extent of the computational domain corresponds to the solar photosphere, with

the chromosphere above in the region $\sim 0.5\text{-}2$ Mm height. The transition region is positioned from approximately 2-3 Mm height, and the corona extends to about 7 Mm with the final 1 Mm of the domain containing the upper low gravity region.

3.4 MHD simulations - the modified CD4 scheme

The TVDLF scheme which has been used in the hydrodynamic simulations causes problems when used for the magnetohydrodynamic case. The zero gravity boundary condition, which is used successfully with no magnetic field, causes an instability when a field is applied which quickly crashes any simulations. One solution to this would be to construct a boundary condition which enforces the condition of hydrostatic equilibrium properly at the upper and lower boundaries of the domain, while allowing perturbations to exit the domain.

This task is non-trivial when a TVDLF scheme is used, because the spatial derivatives of the flow variables, crucially in this case the conserved energy (from which the pressure is determined) are not well defined under the TVDLF scheme. This results in minor discrepancies between the calculated boundary values for variables and the hydrostatically stable values, generating flows which become quickly problematic. One way of getting around this problem is to use a central differencing scheme instead of the TVDLF scheme, as in a central differencing scheme the spatial derivatives are consistently defined.

3.4.1 An MHD code for gravitationally stratified media

For the reasons above, the VAC TVDLF scheme is not suitable for the MHD simulations that are presented in this thesis. Instead, the simulations in which a magnetic field is present are performed using the ‘MHD code for gravitationally stratified media’ described by Shelyag et al. (2008), called ‘SAC’ (Sheffield Advanced Code).

This code has been designed to address some of the particular challenges that arise when looking to perform non-linear MHD simulations in a gravitationally stratified stable equilibrium atmosphere. Several numerical schemes have been designed with controlled small scale numerical diffusion as a way of enhancing numerical stability (Caunt & Korpi 2001; Stein & Nordlund 1998; Shelyag et al. 2006; Vögler 2003; Nordlund & Galsgaard 1997). However, in

simulations of the gravitationally stratified solar atmosphere such as are presented here, in which the physics of the heavily stratified transition region is of crucial interest, this use of an artificial diffusion in the scheme introduces a small but unavoidable large scale numerical diffusion. The same is the case for TVD or Riemann solver based numerical schemes. Such diffusion can therefore cause the collapse of the background magnetohydrostatic equilibrium in the model, and lead to the development of an unphysical flux that smears the background model (Boris & Book 1973; Tóth 1996).

One alternative that avoids the problems associated with these unphysical fluxes is the use of Flux Corrected Transport (FCT) schemes with strong anti-diffusion terms. While these schemes behave more promisingly in some ways, Boris & Book (1973); Erdélyi & James (2004), they may be more difficult to parallelise, and (Tóth 1996) reports the possibility of spurious oscillations in these schemes.

Shelyag et al. (2008) aim to avoid the problems of unphysical numerical diffusion and spurious oscillations by combining the use of hyperdiffusive terms with linearised MHD approaches, while removing the linear limit requirement. They hence produce a scheme capable of modelling both linear and non-linear processes in strongly stratified media.

3.4.2 Equations of perturbed MHD

Underlying the numerical method of Shelyag et al. (2008) is the use of a form of the MHD equations based on the assumption of an underlying magnetohydrostatic equilibrium (c.f. §2.2.1):

$$\frac{\partial \tilde{\rho}}{\partial t} + \nabla \cdot [\mathbf{v}(\rho_b + \tilde{\rho})] = 0 + D_\rho(\tilde{\rho}), \quad (3.22)$$

$$\begin{aligned} \frac{\partial[(\rho_b + \tilde{\rho})\mathbf{v}]}{\partial t} + \nabla \cdot [\mathbf{v}(\rho_b + \tilde{\rho})\mathbf{v} - \tilde{\mathbf{B}}\tilde{\mathbf{B}}] - \\ \nabla \left[\tilde{\mathbf{B}}\mathbf{B}_b + \mathbf{B}_b\tilde{\mathbf{B}} \right] + \nabla \tilde{p}_t = \tilde{\rho}\mathbf{g} + \mathbf{D}_{\rho v}[(\tilde{\rho} + \rho_b)\mathbf{v}], \end{aligned} \quad (3.23)$$

$$\begin{aligned} \frac{\partial \tilde{e}}{\partial t} + \nabla \cdot [\mathbf{v}(e + e_b) - \tilde{\mathbf{B}}\tilde{\mathbf{B}} \cdot \mathbf{v} + \mathbf{v}\tilde{p}_t] - \\ \nabla \left[(\tilde{\mathbf{B}}\mathbf{B}_b + \mathbf{B}_b\tilde{\mathbf{B}}) \cdot \mathbf{v} \right] + p_{tb}\nabla\mathbf{v} - \mathbf{B}_b\mathbf{B}_b\nabla\mathbf{v} = \\ = \tilde{\rho}\mathbf{g} \cdot \mathbf{v} + D_e(\tilde{e}), \end{aligned} \quad (3.24)$$

$$\frac{\partial \tilde{\mathbf{B}}}{\partial t} + \nabla \cdot [\mathbf{v}(\tilde{\mathbf{B}} + \mathbf{B}_b) - (\tilde{\mathbf{B}} + \mathbf{B}_b)\mathbf{v}] = 0 + \mathbf{D}_B(\tilde{\mathbf{B}}), \quad (3.25)$$

3.4.3 Numerical methods

Shelyag et al. (2008) apply a fourth order central difference scheme for the spatial derivatives, and apply either a second or fourth order Runge-Kutta time advance scheme. Additional stabilisation is normally necessary to prevent the development of spurious oscillations from the use of the central difference scheme. This is provided in this scheme by means of numerical diffusion and resistivity.

The term D in the energy equation consists of three parts:

$$D_e = D_e^{diffusive} + D_e^{viscous} + D_e^{ohmic}, \quad (3.26)$$

describing thermal diffusion, viscous and ohmic heating of plasma, respectively.

The hyperdiffusive terms for scalar quantities are written as follows:

$$D_\rho = \sum_i \frac{\partial}{\partial x_i} \nu_i(\rho) \frac{\partial}{\partial x_i} \tilde{\rho}, \quad (3.27)$$

$$D_e^{diffusive} = \sum_i \frac{\partial}{\partial x_i} \nu_i(e) \frac{\partial}{\partial x_i} \tilde{\epsilon}. \quad (3.28)$$

The derivatives in Eqns. (3.27) and (3.28) are applied in a way that the outer derivative is taken forward, while the inner derivative is taken backward, and the viscosity coefficient is interpolated backward on the grid cell interface. In Eqn. (3.28) $\tilde{\epsilon}$ is the thermal energy perturbation $\tilde{\epsilon} = \tilde{e} - (\tilde{\rho} + \rho_b)\mathbf{v}^2/2 - \tilde{\mathbf{B}}^2/2$.

The hyperviscous terms for vector quantities are more complicated, i.e.:

$$\mathbf{D}_\rho \mathbf{v} = \nabla \cdot \boldsymbol{\tau}, \quad (3.29)$$

and

$$\mathbf{D}_\mathbf{B} = -\nabla \times \mathcal{E}. \quad (3.30)$$

The hyperviscous and ohmic heating terms in Eqn. (3.26) are set as follows:

$$D_e^{visc} = \nabla \cdot (\mathbf{v} \cdot \boldsymbol{\tau}) \quad (3.31)$$

and

$$D_e^{ohmic} = \nabla \cdot (\mathbf{B} \times \mathcal{E}). \quad (3.32)$$

The viscous tensor τ is given by

$$\tau_{kl} = \frac{1}{2} (\tilde{\rho} + \rho_b) \left[\nu_k (v_l) \frac{\partial v_l}{\partial x_k} + \nu_l (v_k) \frac{\partial v_k}{\partial x_l} \right], \quad (3.33)$$

the vector quantity \mathcal{E} is defined as

$$\mathcal{E}_k = \epsilon_{klm} \left[\nu_l \left(\tilde{B}_m \right) \frac{\partial \tilde{B}_m}{\partial x_l} \right], \quad (3.34)$$

where ϵ_{klm} is the Levi-Civita symbol, and the summation is over l and m indices.

The derivatives in the expressions Eqns. (3.29)-(3.32) are such that if the direction of the outer derivative is the same as the direction of the inner derivative, then they are calculated using the same principle as the derivatives in Eqns. (3.27)-(3.28). If the direction of the outer derivative is different from the direction of the inner derivative, then both derivatives are evaluated using a second order central difference scheme, and the viscous coefficients are interpolated to the grid cell centres.

The viscous coefficient ν for the variable u in the i -th direction is expressed as

$$\nu_i (u) = c_2^u \Delta x_i v_t \frac{\max |\Delta_i^3 u|}{\max |\Delta_i^1 u|} + c_1^u \nu_s, \quad (3.35)$$

where $v_t = v_a + v_s$ is the sum of maximum Alfvén and sound speeds in the domain, operators Δ_3 and Δ_1 are the forward differences of the third and first order taken in the i -th direction, and Δx_i are the spatial resolutions. The maxima are taken over five grid cell stencils in the i -th direction. Coefficients c_1^u and c_2^u can be defined for each variable separately and are selected in the way that the hyperdiffusion ensures numerical stability of the solution, and the solution is not influenced strongly by the diffusion. ν_s , the shock viscosity, is defined in the following way:

$$\begin{aligned} \nu_s &= \Delta x_i^2 |\nabla \cdot \mathbf{v}|, \quad \nabla \cdot \mathbf{v} \leq 0, \\ \nu_s &= 0, \quad \nabla \cdot \mathbf{v} > 0, \end{aligned} \quad (3.36)$$

and ensures that regions with strong compression remain resolved by the numerical scheme (Von Neumann & Richtmyer 1950).

The time step is limited by the standard CFL condition and by the hyperdiffusion time scale, given by the following expression:

$$\Delta t = \frac{k \Delta x^2}{\max(\nu)}. \quad (3.37)$$

Here the coefficient k is an equivalent to the constant coefficient of the CFL condition and is less than one to ensure the stability of the solution.

Returning to the problem experienced when looking to apply the VAC TVDLF scheme to the fully magnetic stratified case, the variable separation approach of Shelyag et al. (2008) has the advantage that it is possible to construct a “transparent” boundary condition for the energy perturbation without any requirement of magnetohydrostatic equilibrium. The condition becomes simply $\partial\tilde{e}/\partial x = 0$. This boundary condition, in terms of the values of the function defined on the grid, can be expressed as follows:

$$f_{N+i} = f_{N-i}, \quad (3.38)$$

where N is the position of the last grid cell in the working part of the domain, and the function is symmetrically copied from the working part of the domain to the ghost cells. Two layers of the ghost cells are necessary for the fourth-order central difference numerical scheme used in the code.

Similar boundary conditions are introduced for the other variables. The authors note that it is in principle possible and perhaps desirable to define higher order boundary conditions for higher precision calculations.

The scheme is implemented using the MPI VAC code (Tóth 1996) with an expanded domain decomposition to accommodate the additional grid cell requires from each neighbouring subdomain by the hyperdiffusion and hyperresistivity modules for a larger 7-point stencil.

Chapter 4

Leakage of point driven photospheric acoustic waves into non-magnetic solar atmosphere

4.1 Abstract

This chapter considers the propagation of synthetic photospheric oscillations from a point source into a two-dimensional non-magnetic solar atmosphere, with specific focus on the leakage of 5 minute global oscillations into the atmosphere. A model solar atmosphere is constructed based on realistic temperature and gravitational stratification and the response of this atmosphere to a range of periodic velocity drivers is numerically investigated in the hydrodynamic approximation.

The findings of this modelling are threefold. Firstly, in the absence of non-ideal effects high-frequency waves are shown to propagate from the lower atmosphere across the transition region experiencing relatively low reflection and transmitting energy into the corona. Secondly, it is demonstrated that driving the upper solar photosphere with a harmonic piston driver at around the 5 minute period may generate three separate standing modes with similar periods in the chromosphere and transition region. In the cavity formed by the chromospheric cavity this is caused by reflection, while at either end of this region in the lower chromosphere and transition region the standing modes are caused by resonant excitation. Finally, the transition region becomes a guide for horizontally propagating surface waves for a wide range of driver periods,

and in particular at those periods which support chromospheric standing waves. Crucially, these findings are the result of a combination of a chromospheric cavity and resonant excitation in the lower atmosphere and transition region.

The results presented in this chapter are the results published by Erdélyi, Malins, Tóth, & De Pontieu (2007).

4.2 Introduction

The Sun is a turbulent and energetic environment, and the motions of its ‘surface’ and atmosphere are turbulent and complex. To computationally model the full complexity of such a system is, to say the least highly challenging, but it is instructive to consider idealised cases using numerical methods. When one looks at observational data, the full complexity of the system can actually obscure the underlying processes taking place. In this work, the transmission of information from idealised oscillations at the solar surface into the solar atmosphere is examined, by applying oscillatory drivers to a steady state two dimensional computational representation of the solar atmosphere.

In this Chapter, we consider a magnetic field free (hydrodynamic) case as an approximation to the quiet Sun, and we apply a simple point driver. The use of a single point driver makes it relatively simple to analyse the way in which signals propagate into the model atmosphere, not least because the path of the waves can be followed visually. It is possible to isolate by visual inspection of results the effects of reflection, in particular any reflection of signals as they reach the transition region.

Also, there is some degree of comparability between the results of 2D simulations using a point driver, and the results of previous one dimensional simulations. Specifically, if a cross-section is considered which is taken vertically through the point of application of the driver, one would expect a qualitative similarity between the results of the 2D simulation apparent on this cross-section, and the results of 1D simulations using similar atmospheres and drivers.

The intent of this research is to investigate the effects of motions at the solar surface and photosphere on the higher solar atmosphere. In particular, any connection between solar global p modes which are observed at the solar surface and oscillatory motions in the higher

atmosphere is of interest. The point driver is therefore applied towards the bottom of the simulated atmosphere, and the upwards propagation of the driven signals is carefully observed.

Any synthetic driver represents a profound simplification of the complex motions present on a solar surface which is highly dynamic, and this applies especially to the point driver used in this section of the research. On the other hand, the advantage of the point driver is that it enables a greater clarity of analysis, allowing us to focus strongly on the importance of the parameters which are investigated, primarily the period of the driven signal, to the results. While it is important to be mindful of the extreme simplifications applied in the simulations, these simulations should help us to achieve a clearer understanding of the way in which signals propagate in the solar atmosphere.

The signals observed on the real Sun which are of prime interest are the solar global p modes (c.f §1.2), which display a peak in power periods of approximately 5 minutes. In the simulations undertaken not only using this simple point driver, but also using other synthetic drivers, 5-minute signals are therefore an area of strong focus. Nevertheless, the solar surface is a very dynamic region, and plays host to signals with a wide variety of other periods. These signals may be linked directly to p -mode oscillations, or they may be explained by other phenomena. With attention to the existence of this wide range of periodicity, simulations are carried out using point drivers at a wide range of periods.

By investigating the results of changing the driver period, it is hoped that a fuller understanding may be obtained of the sensitivity of the results to the specifics of signal periodicity, and therefore of the importance of periodicity to the physics involved.

A range of driver periods from 10 to 450 seconds has been used in these point driver simulations. This range includes signals which have both longer and shorter periods than the key p -mode period of 5 minutes. By comparing the response of the model atmosphere to these various signal periods, it is possible to gain insight into the degree to which the period of motions in the photosphere affects their propagation (or lack thereof) into the higher atmosphere. It also offers the prospect of determining whether there might be a connection between signals observed with one dominant period in the photosphere, and signals observed at other dominant periods in the chromosphere, transition region and corona.

When using computational models one must recognise the limitations introduced by the assumptions and simplifications which underly a model, and the possibility that unphysical behaviour may be introduced into results due to these simplifications. In the case of the shorter period signals investigated here, it is particularly important to acknowledge the limitations imposed on the model by the assumption of ideal hydrodynamics, neglecting such effects as thermal conduction and radiative emission. While the results obtained using short period drivers are instructive, it is emphasised that the inclusion of thermal conduction and radiative emission would be expected to cause a significant damping of such short period signals in the real atmosphere. Indeed, any propagation of such signals so far as the transition region and into the upper atmosphere would be negligible due to the energy lost by such short period signals to the above mechanisms.

The short period simulations remain valuable because they provide a contrast between the behaviour which would be expected from signals below the acoustic cut-off period (c.f. §2.4), and the behaviour of signals which are around or above the cut-off period. By considering this full range of periodicities, and observing the resulting changes in behaviour, it becomes possible to assert with confidence that certain results are directly related to the changing period of the driven signals, rather than attributable to other factors.

The assumption of ideal HD is justified by the desire to study the longer period signals, and especially the signals with periods around 5 minutes, which can be reasonably studied without considering radiative emission, etc. The damping caused by these physical processes on longer period signals is no longer a dominant process, and thus the results of ideal HD simulations should provide results which can be usefully compared to the real Sun.

From the wide range of drivers used, the two periods which are focused on as representative of the two key regimes (well below cut-off period, around cut-off period) are 30 seconds and 5 minutes. The comparison of these two cases shows clearly the differences in the response of the atmosphere to signals in these two regimes.

In addition to examining a range of frequencies, this part of the work addresses the issues mentioned in §2.1 by applying the drivers to a pair of equilibrium atmospheres. The first of these atmospheres is an atmosphere based on the temperature distribution of the VAL

IIIc temperature profile. The second is an atmosphere which assumes an isothermal ‘cold’ chromosphere, based around the ideas expressed by Carlsson & Stein (1995). By examining both of these cases, it is hoped that the work presented will remain robust in the light of future advances in our understanding of the real nature of the solar atmospheric temperature distribution. These equilibria are discussed in more detail in §2.1 above, including a discussion of the respective cut-off periods in the two atmosphere’s.

To reiterate, although the cut-off frequency varies to some extent on small scales throughout, it is constructive when analysing results, and with an eye specifically to signals with periods at the peak p -mode power between 270 and 320 seconds, to consider the atmosphere as divided into distinct regions of cut-off frequency. In the VAL IIIc case, there are four key regions, while in the cold-chromospheric case there are three.

In the cold-chromospheric case, the photosphere and chromosphere have a cut-off period below 300 seconds and thus 5 minute oscillations will be evanescent. In the VAL IIIc case, a 5 minute oscillation will be evanescent in the photosphere, but in the chromosphere the cut-off period increases with the increasing temperature to a value slightly above 300 seconds, and therefore any signal of period 5 minutes or less will propagate. Around the transition region in both cases the cut-off period drops to a much lower value, perhaps as low as 100 seconds, and so long period signals should be evanescent. Finally, in the corona the cut-off period again becomes high and waves at all of the periods being considered here will propagate freely.

4.3 Short period

4.3.1 30 second driver

It is expected that acoustic waves with high frequencies (10-50 mHz) will be produced in subsurface layers of the Sun (Fossum & Carlsson 2005), and it has been suggested in the past that they may constitute the dominant heating mechanism for the chromosphere. Fossum & Carlsson (2005) demonstrate, using radiative 1D numerical hydrodynamic simulation, that the energy flux of such waves is not sufficient to account for radiative losses in the chromosphere. High frequency waves are also strongly radiatively damped in the upper photosphere (Carlsson & Stein 2002). The study of their propagation into the upper solar atmosphere under the

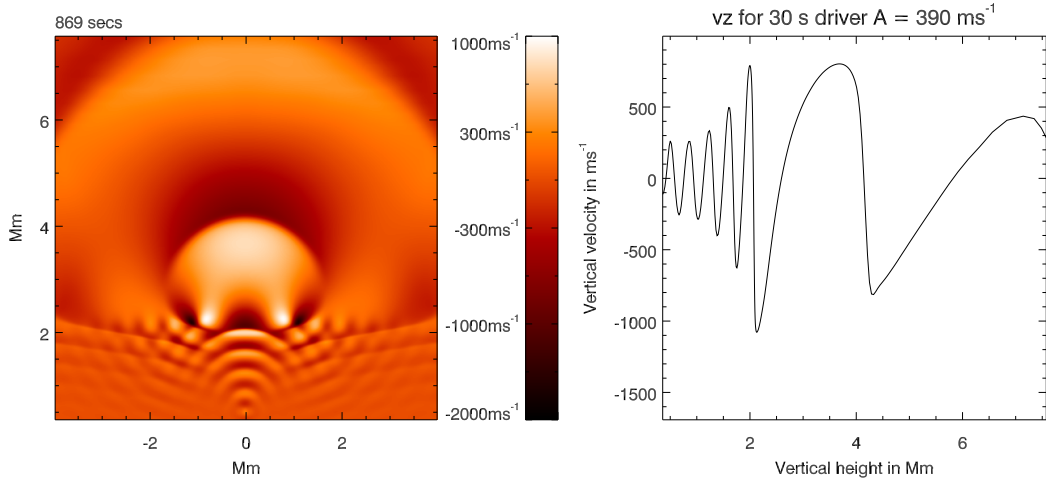


Figure 4.1: Typical snapshot of the vertical velocity in the model for the 30 second driver, taken after 869 seconds. On the left is a visualisation of the full domain (note that the aspect ratio is not 1:1 for convenience of presentation), accompanied on the right by a plot taken along a vertical cross-section at the centre of the domain.

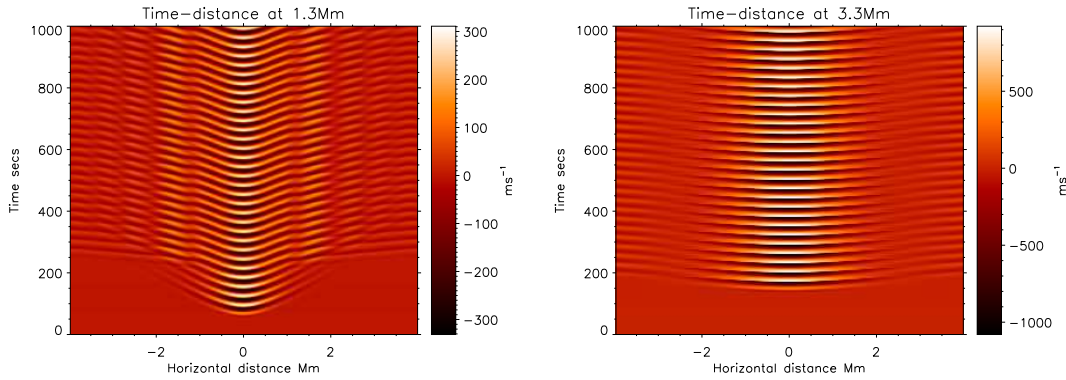


Figure 4.2: a) Time-distance image for 30 second driver showing waves moving across a line taken at 1.3 Mm into the atmosphere (in the chromosphere). b) Similar to (a) but taken at a height of 3.3 Mm and thus in the corona.

assumptions of ideal MHD is therefore relatively academic. Nevertheless, the simulation of the propagation of high frequency waves into the chromosphere and corona is of interest from a diagnostic perspective, and working in 2D it becomes possible to examine the effects of attenuation on propagating high frequency waves.

Drivers at several periods in the high frequency range were studied, with the drivers applied just above the temperature minimum at a height of 450 km. The case of a 30 second driver is

discussed, but the main conclusions apply equally well to other drivers with periods well below the cut-off period (30 seconds is of course well below the local acoustic cut-off period at any point). Fig. 4.1 is a snapshot in time of the vertical velocity observed in the domain, taken after 869 seconds. On the 2D image on the left, the quasi-circular propagating wavefronts are clearly apparent in the lower atmosphere, while in the corona the enhanced wave speed distorts the shape of the wavefronts and causes the increased spatial separation (the wavelength which is around 400 km in the photosphere and chromosphere increases to ~ 2 Mm in the corona).

On the right hand side of Fig. 4.1, there is a snapshot of the vertical velocity plotted along a vertical line through the point of driver application. It is clear from this graph that the amplitude of the velocity perturbations increases with height up to the transition region. This is a result of the gravitational and temperature stratification of the atmosphere, as one would expect from De Moortel & Hood (2004). This amplitude growth shows that the stratification driven amplification is stronger than the attenuation of the wave front during propagation. In the presence of a magnetic field acting as a wave guide, this growth in a solar atmospheric magnetic flux tube would be even more pronounced for any slow/mixed modes which share some of the characteristics of these acoustic-gravity modes, and can be considered analogous in behaviour (De Pontieu et al. 2004).

The transit of the waves across the high gradients (in temperature, pressure and density) at the transition region into the corona causes the most rapid enhancement in the amplitude of this perturbation. Having crossed the transition region, the waves then propagate away into the corona. At these heights, the temperature stratification of the atmosphere is relatively mild, and hence the amplitude of the transmitted signal slowly decreases due to the dispersal of the wave across an ever greater area of 2D space. The higher coronal temperature is accompanied by a larger sound speed, and therefore there is a significant increase in the propagation speed of the wave as it passes the transition region.

These results are all qualitatively consistent with the results presented by De Moortel & Hood (2004) for the vertical propagation of perturbations guided by a magnetic field in a gravitationally stratified one-dimensional isothermal atmosphere.

A useful way to visualise wave propagation at a given height is to construct time-distance

images. Because the sound speed is uniformly increasing with height in the VAL IIIc atmosphere, it is possible to infer the direction of propagation of any of the wavefronts which appear on these images. The waves are emitted by a point source towards the bottom of the computational domain, and take longer to reach the horizontal extrema of the domain than the centre at any given height. In an isothermal atmosphere with constant sound speed, this will give a wave travelling up from the source a curvature like this \smile , especially at the centre of the wavefront. In the stratified VAL atmosphere, an upwardly propagating front accelerates with height, tending to accentuate the upwards curvature of the wavefront in the time-distance representation.

Any signal reflected at the transition region, or indeed elsewhere, will be travelling downwards. Such signals decelerate as the temperature decreases with height, so that the wave fronts will appear flatter and with curvature slightly downwards, more like this \frown . Any wavefronts propagating purely horizontally will move at the sound speed for the height in question and will appear on the time-distance plot as lines of constant gradient, where the gradient will match the sound speed.

Fig. 4.2a shows the signal at a height of 1.3 Mm. The first few wavefronts pass through showing the curvature characteristic of a wave propagating upwards, just as one would expect. After about 240 seconds the first wavefront from the transition region reaches this height. These reflected waves are travelling down with reducing sound speed, and thus display the opposite curvature. It is clear from the time-distance image that the reflected component of the wave has a somewhat smaller amplitude than the incident wave. However, it is also spread over a larger area. It is estimated that at this frequency approximately 40% of the wave energy is transmitted into the corona while the other 60% is trapped in the lower atmosphere by the reflection.

The waves exhibit the highest amplitudes (visible here as the lightest and darkest regions) directly above the driver. This is because where the wave is travelling vertically, the stratification induced amplification is most dominant over the dispersive attenuation (see Fig. 4.1), and the distance travelled by the wavefront is least. Further out the signals have a much lower amplitude.

The reflected wavefronts in contrast have approximately similar amplitudes from the centre to the horizontal extent of the domain, which suggests that the more inclined propagation at the edges of the box leads to stronger reflection. Also, the changing sound speed refracts them so that the direction of propagation is primarily vertically downwards. The interference between the upwards and downwards propagating waves is visually apparent as alternating vertical bands of higher (points of constructive interference) and lower (points of destructive interference) peak amplitude

The time distance image for a height of 3.3 Mm in Fig. 4.2b has wavefronts that are much flatter, indicative of the higher coronal sound speed. The small curvature which is apparent shows that these signals are propagating upwards. At the horizontal extrema of the domain there is evidence of a slightly different element to the signal with the curvature indicative of downwards propagation. Examining Fig. 4.1 at the height of 3.3 Mm the explanation is clear. At a sufficient horizontal distance from the centre of the domain, the 3.3 Mm line is below the height at which the wavefront achieves its maximum width and is propagating horizontally, and the signal actually has a small downwards component. There is no reflection coming from higher in the atmosphere, and hence no interference.

The data from the 30 second driver does not show any clear evidence of the generation of a resonant signal at the cut-off period, and the use of wavelet analysis does not show any clear evidence of strong power in the long period range that is covered by the cut-off at various heights. This is all consistent with the prediction that driven signals below the cut-off period would dominate any resonant response.

The signal is associated with some temperature variations, but these are insignificant compared to the background temperature. In particular, at a driven amplitude of 390 m s^{-1} , the waves do not drive any significant change in the position of the transition region nor do they drive any significant flow of cool matter into the corona.

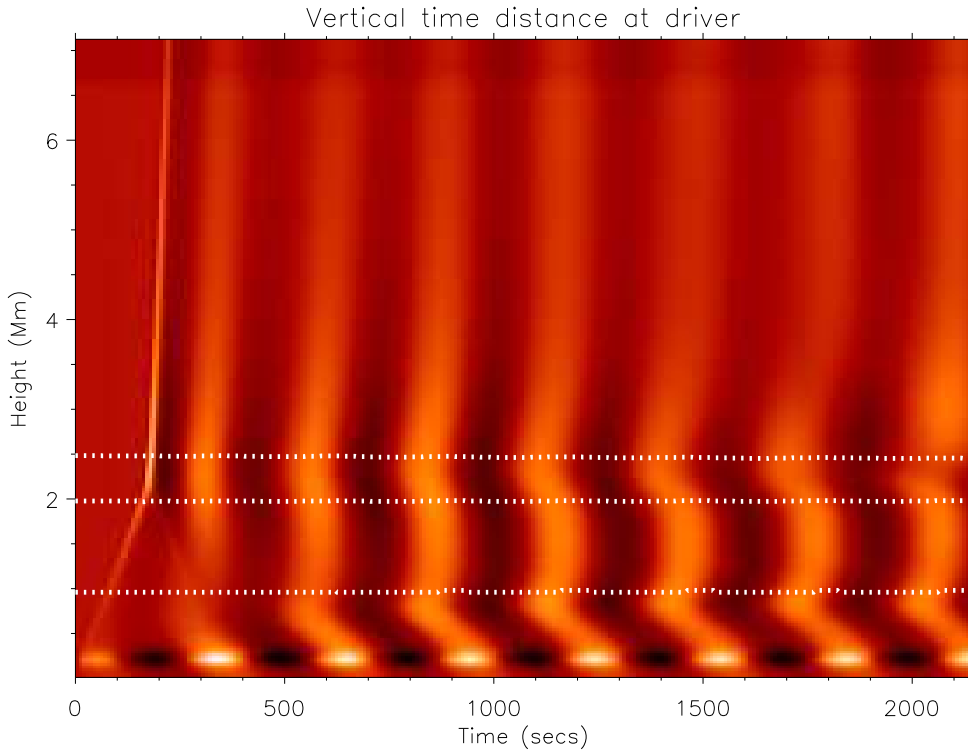


Figure 4.3: Time distance image along the central vertical axis of the computational domain showing vertical velocity. The dotted lines show where the cut-off frequency is exactly 300 seconds.

4.4 Long period

4.4.1 300 second driver

The 300 second driver is of particular interest because this is around the period of many oscillations observed in coronal loops with footpoints in plage regions (De Moortel et al. 2002a,b), of oscillations in transition region moss (De Pontieu et al. 2003a, 2005) and of the dominant *p*-mode period in the photosphere. The simulations model the potential propagation of 5-minute acoustic signals in the non-magnetic atmosphere from the photosphere upwards into the rest of the solar atmosphere. Results from these simulations provide insight into the possible leakage of solar global 5 min photospheric *p*-modes into the solar chromosphere, transition region and corona, in regions where the non-magnetic approximation is reasonable.

The 300 s driver is applied at a height of 200 km, below the photospheric temperature

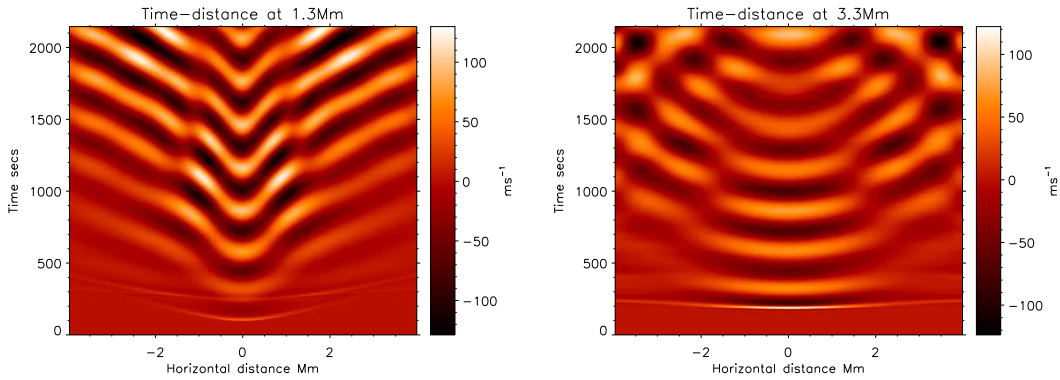


Figure 4.4: a) Time-distance image for 300 second driver showing vertical velocity along a horizontal line taken at 1.3 Mm into the atmosphere (in the chromosphere). b) Similar to a, but taken at a height of 3.3 Mm and thus in the corona.

minimum. For simplicity the temperature distribution has been set to be isothermal below the temperature minimum, at the minimum temperature. The driver period is slightly above the cut-off period at the point of application, and it is expected that the signal will be evanescent immediately above the driver height up to ~ 700 km, and therefore that the resonant excitation at the cut-off frequency will become the dominant signal.

The long period simulation has a richer behaviour than the short period, and the behaviour is continuously evolving with time. Before we examine the full two dimensional behaviour of the model, it is helpful to consider the behaviour of the signal along the central vertical axis of the domain, reducing the analysis to 1D for a moment, by taking a time distance image along this axis, see Fig. 4.3. The effect of the local cut off period on the simulations is most apparent from the behaviour along a vertical line through the point of driver application. Marked on this image are dotted lines depicting the height at which the local cut-off period is exactly 300 seconds. None of these occur at local maxima or minima of the cut-off, so these lines indicate the heights at which the behaviour of signals at the 300 second driver period should alter from evanescent to propagative, or vice versa. They hence delineate the two evanescent regions: one at the bottom of the domain in the upper photosphere and lower chromosphere and the other around from ~ 2 Mm - 2.5 Mm at the transition region where the strong stratification reduces the cut-off period. Between these two regions, and in the corona, a 300 s period signal should be propagative. Where the ‘chromospheric cavity’ is referred to, it should be taken to mean the propagative region in the mid to upper chromosphere.

We now consider the different behaviours that are apparent as height increases in the simulations. Firstly, towards the bottom of the graph the driving signal can be seen clearly as a thin band of alternating bright and dark with the 300 second period. The region where the driver is dominant is spatially limited, and between the driver and the first ‘cut-off line’ we see the development of a signal with a slightly shorter period than the driver, and a slightly lower amplitude.

The presence of this signal at a higher than driven frequency is a consequence of the resonant excitation of the cut-off frequency mode. This resonant signal becomes stronger over time, as the evanescent driver signal loses energy to the cut-off mode. As predicted, given the evanescence of the longer period driven signal, it quickly becomes the dominant signal in the upper photosphere.

Moving further up into the atmosphere, there is another distinct behaviour in the chromospheric cavity. Here we see a dominant period that is longer than that in the photosphere, but still shorter than the driver period. This region is discussed below in more detail in §4.4.2. At the transition region in the second evanescent zone, we see a separate behaviour again. Here the dominant period is again shorter than the 300 second driver period, but also shorter than either the period of the dominant oscillation in the chromospheric cavity, or period of the resonant oscillation in the photospheric evanescent region. This result is again consistent with our expectation based on the prediction that resonant excitations will be excited at the local cut-off period. Looking back at Fig. 2.1 it is clear that the cut-off period is shorter in the transition region than at any other point in the domain. It is thus unsurprising that the region should display the shortest period oscillatory response.

Finally, we see that there is significant signal transmission into the corona. The initial pulse is apparent as a well defined straight line, the slope of which is the sound speed in the corona. Although the sound speed does increase with height in the corona, it is approximately constant, and the subsequent light and dark bands are parallel to this first line. The coronal signal can be seen to be driven by the resonant signal at the transition region, although there is a certain amount of interference in the lower corona at later times (c.f. §4.4.3).

Fig. 4.4b is a time distance image taken along a horizontal line at a height of 3.3 Mm in

the corona. Again, we see the transmission of wave energy beyond the transition region into the corona, but this transmission shows nothing like the strong amplitude growth from the driver amplitude which the stratification gives to the shorter period waves (c.f. §4.3). Rather, the maximum amplitude recorded at 3.3 Mm is $\sim 120 \text{ m s}^{-1}$ which is below the maximum amplitude at 1.3 Mm of 130 m s^{-1} and the driver amplitude of 270 m s^{-1} .

The bulk of the energy deposited into the system by the driver is prevented from propagating into the corona, firstly by the resonant excitation of cut-off modes due to driver evanescence, and secondly by strong reflection at the transition region. This transition region reflection can be seen clearly for the initial pulse in Fig. 4.3. The first driven pulse can be seen as a straight line propagating through the chromospheric cavity, which is then divided upon hitting the transition region into a transmitted part in the corona, and a reflected part travelling back down into the chromospheric cavity. The transmission coefficient for these longer period signals is much shorter than for short period signals. It is estimated that only of the order of 1% of the wave energy is able to penetrate from the chromospheric cavity to the corona.

On Fig. 4.4b the initial transmitted pulse can be seen after 150 seconds. Shortly after this at 250 seconds is a second peak. It is clear from these timings that the second peak cannot have originated from the second driver peak, nor is there a reflection from a higher point in the corona. This coronal signal in fact originates from the resonant excitation of the transition region, as is visible in Fig. 4.3. The hundred second delay between the initial pulse and the second pulse is consistent with the generation of a signal in the transition region which has some power at the one hundred second period, which we calculated to be the minimum cut-off period in the transition region.

Crucially, the photospheric p -modes have thus generated a shorter period signal which is transmitted into the corona.

The behaviour visible in Fig. 4.4b is more complex than this however. After about 800 seconds, there are clearly several separate signals at different horizontal positions. The horizontal behaviour visible in Fig. 4.4b is due to the leakage into the corona of the transition region surface waves discussed below in §4.4.3. Higher in the corona these surface waves are not apparent.

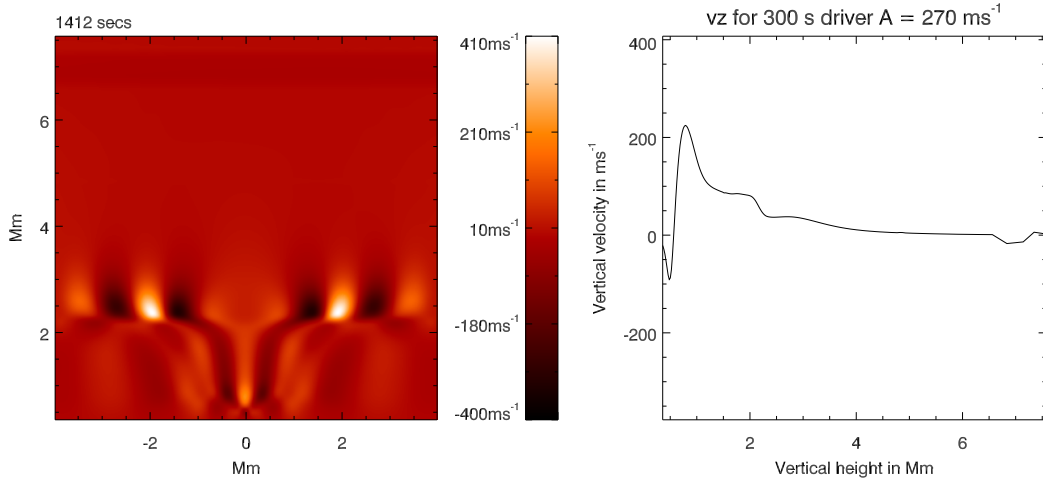


Figure 4.5: Same as Fig. 4.1 but for a 300 second driver, snapshot taken after 1412 seconds.

4.4.2 Standing waves

Fig. 4.5 is a snapshot of vertical velocity in the domain after some time has passed. Inspecting the right hand side, which depicts a snapshot in time of the vertical velocity along a vertical line through the point of driver application, we can compare the signal amplitude with height here to the signal amplitude with height in the shorter period case (c.f. Fig. 4.1). Of course, as the signals at different heights are not all in phase, they cannot all be seen achieving their maximum amplitudes in one snapshot in time. This image is, however, representative of several features discussed below.

While the shorter period signals show immediate growth due to stratification, this is not apparent here. Rather, in this snapshot we see a local maximum for velocity magnitude at ~ 750 km in the photospheric resonant region, with the amplitude dropping off to ~ 1 Mm due to evanescence.

In the chromospheric cavity the signal should be propagative again and here we indeed see a combination of stratification driven growth and interference from reflected waves counteracting wave dispersal, so that the signal amplitude grows from 1 Mm to ~ 2 Mm, achieving another local maximum at the transition region (as in the short period case). This local maximum is comparable to the driver amplitude, whereas in the short period case it was significantly greater than the driver amplitude. This is due to the deposition of energy at the resonant

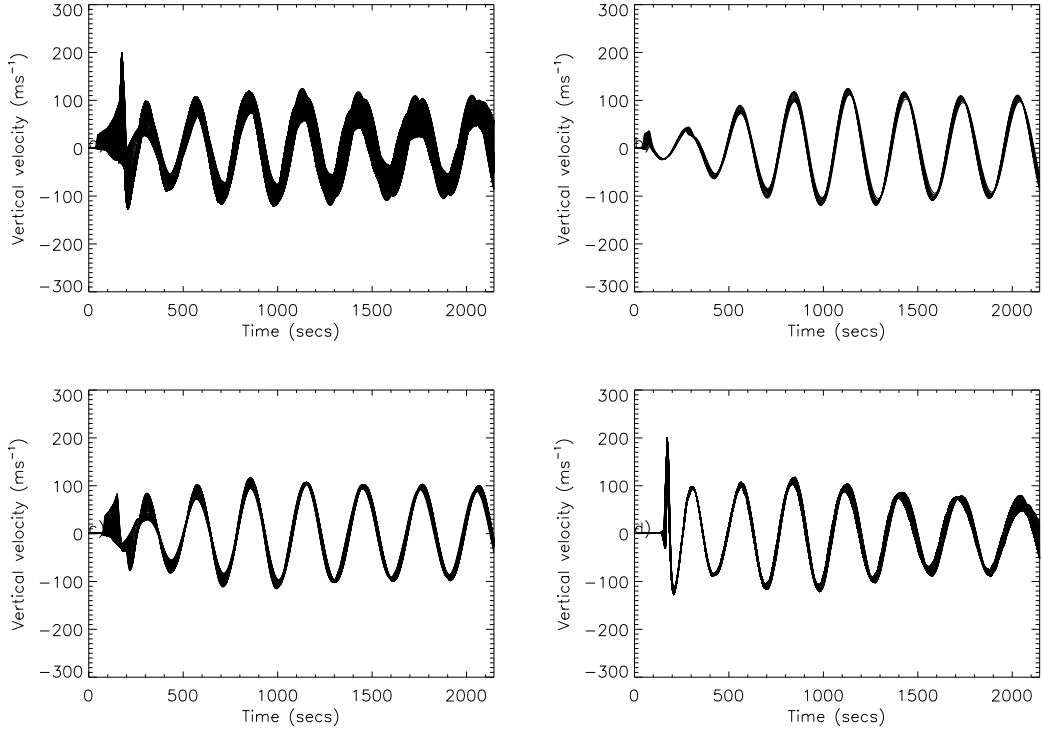


Figure 4.6: a) Here the vertical velocity along the central vertical axis of the computational domain is plotted on the same axes for each gridpoint in the range $650 \text{ km} < z < 3.3 \text{ Mm}$. b) Similar to a, but in the range $700 \text{ km} < z < 1 \text{ Mm}$. c) Similar to a, but in the range $1.1 \text{ Mm} < z < 1.9 \text{ Mm}$. d) Similar to a, but in the range $2.1 \text{ Mm} < z < 2.5 \text{ Mm}$.

frequency in the photosphere.

Going from left to right, from photosphere to corona on the right of Fig. 4.5 the first feature is the driver. This is visible as the local minimum at the far left of the plot. Clearly, the driver is not in phase with the behaviour of the rest of the model atmosphere, registering as it does as the only negative velocity along this line. In contrast, in this snapshot we notice that the signal from the resonant zone above the driver right through to the transition region and corona is uniformly positive. Movies of the data support the impression that a standing mode, or something very close to a standing mode, is set up above the driver. To determine whether this is truly a single coherent standing mode, consider Fig. 4.6.

Fig. 4.6a is a superposition of plots of velocity against time at every datapoint along the central vertical axis from the photospheric resonant region to the low corona. The spread of

the lines in the time direction is an indicator of the extent to which the signals at these various different heights are coherent. If they were perfectly coherent then while the amplitudes might vary, each signal would achieve maximum amplitude at the same time, and the zeros of velocity would all occur at the same time. The ‘width’ in time of the region where the various signals record zero velocity is therefore a measure of how out of phase the signals are. In Fig. 4.6a there is clearly a strong similarity between the phase of the signals at different heights. However, the signals are certainly not exactly in phase, with a typical lag of ~ 50 secs between the first and last signals to reach zero velocity and a clear tendency for the signals to become more out of phase as time progresses.

Fig. 4.3 suggests that there is not a single standing wave from the photosphere all the way to the transition region, but that there are sub-regions in which the signal is coherent and in which the standing wave description may apply. Specifically, firstly there is the signal in the lower chromospheric evanescent region above the driver that seems to be coherent over ~ 300 km in height. Above this, in the propagative chromospheric cavity it appears that the signal is again coherent over ~ 800 km. In Fig. 4.3 this gives the appearance of light and dark stripes in the chromospheric cavity, and these seem to occur at a period above the lower chromospheric resonant period, but still shorter than the 300 second driver period. Finally, in the transition region it appears that the signal is relatively coherent over ~ 400 km.

Fig. 4.6b, c and d show the signals only at gridpoints in the low chromosphere, chromospheric cavity and transition region respectively. It is clear that in each of these regions, the signals are indeed very strongly coherent. Fig. 4.7 shows the signal at a single data point in each region and the driven signal, from which it is equally clear that there is a difference in phase and frequency between each of the three, and the driver signal itself.

The signal represented on Fig. 4.7b covers the area of the lower chromosphere above the temperature minimum in which the local acoustic cut-off frequency is > 3.3 mHz. It is expected (Fleck & Schmitz 1991; Rae & Roberts 1982; Roberts 2004) that a signal below the cut-off frequency will cause resonant excitation, and this fits with the results. This resonant response achieves a local maximum at about 750 km, the height at which resonance becomes dominant over the driven signal. The signal at this height starts to oscillate at the local cut-off period of ~ 280 seconds, but by the end of the simulation is oscillating with a period of 300 seconds.

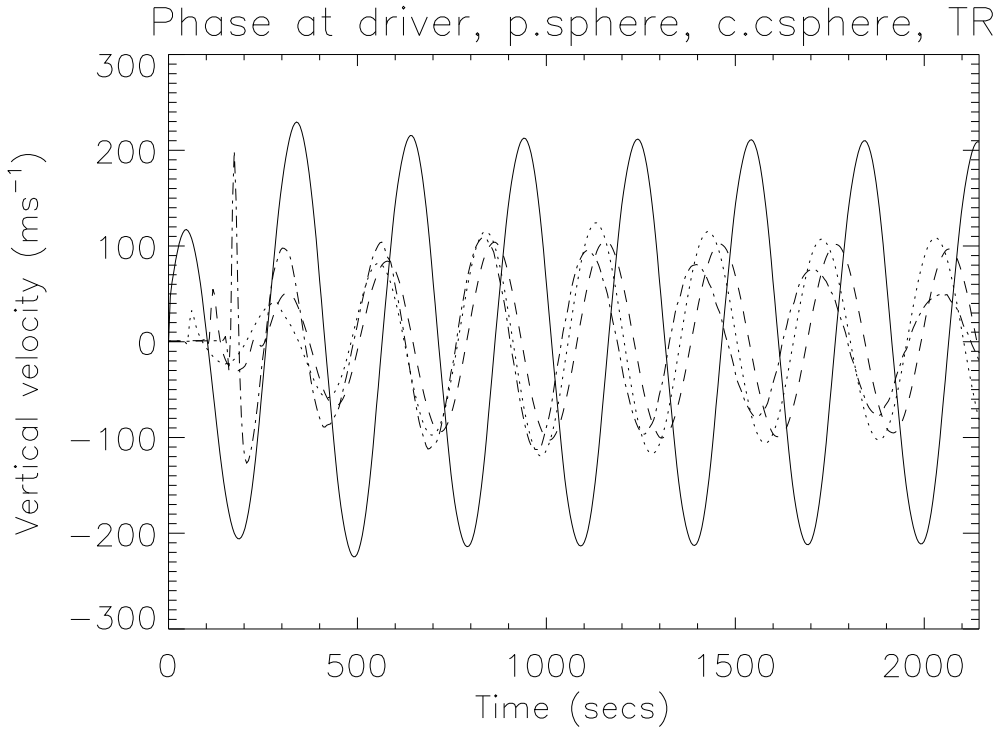


Figure 4.7: The four lines on this graph plot the vertical velocity at four different heights on the central axis. The solid line is at the driver height, the dotted line is above the driver in the lower chromosphere where the 300 second signal is evanescent, the dashed line is in the chromospheric cavity and the dot-dashed line is in the transition region.

This supports the theoretical prediction (Fleck & Schmitz 1991) that the driver period should become dominant as time progresses.

The next part of the graph, from 1-2 Mm, is harder to interpret. The forward modelling data show clear evidence of the existence of a coherent standing wave in the chromospheric cavity, see Fig. 4.6c. Fleck & Deubner (1989) presented observational evidence of the existence of standing waves in the chromosphere, and thus the presence of standing waves in the simulations is of great interest. In Fig. 4.5 in the 2D image the vertically coherent waves spreading outwards from the centre at chromospheric heights suggest that there is a standing mode in the cavity, and this can be seen in Fig. 4.3 where the alternating light and dark bars in the chromospheric region 1-2 Mm show that the signal is approximately vertically coherent. The signal here starts with a period of about 255 seconds, but this increases to 300 seconds (never above 300 seconds) by the end of the simulation.

In this region, the 300 second signal, or for that matter any resonant signals from lower, should be able to propagate. Any resonant response at the local cut-off frequency would be at a period > 300 seconds, but should also be negligible compared to the propagating signal. Rather, the presence of what seems to be a highly coherent standing wave in this region is due to reflection of the propagating signal at the transition region, at a height of ~ 2.1 Mm (Fig. 4.3). There may also be reflection at the bottom of the chromospheric cavity, however the stratification here is very much gentler than at the transition region and any reflection is likely to be weak.

The transit time from the bottom of the chromosphere to the reflection point and back again is ~ 270 seconds, and this is a good match for the period of the chromospheric standing wave as would be expected. The reflection based interpretation of the standing mode does not offer an explanation of the increase in signal period from 255 to 300 seconds. However, given that the chromospheric cavity is only semi-closed it is unsurprising that the behaviour of the resonant signal, especially below, influences the cavity signal. There is further discussion of the cavity mode in §4.4.4.

Finally, from about 2.1–3.5 Mm, is the transition region signal. On the full 2-D image on the left of Fig. 4.5 this signal is very clear, manifesting as the centre of a surface wave propagating out along the transition region. Fig. 4.3 clearly shows that this signal has a higher maximum amplitude than that of the chromospheric standing wave, but an amplitude below that of the resonantly excited wave in the photosphere or of the driver. Comparing this to the result for the high frequency 30 second wave for which the transition region represented maximum amplitude, it is evident that much of the wave energy fails to reach the transition region, instead being trapped in the photosphere and chromosphere. The signal initially has a period of ~ 235 seconds, but this increases to 270 seconds and thence to 300 seconds by the end of the simulation. The signal is due to the resonant excitation of the transition region cut-off frequency mode, and as above this increase to the driver period is predicted analytically. In the transition region the cut-off period is strongly varying, and drops significantly shorter than 235 seconds. However, it seems that a response is excited primarily at a ‘typical’ cut-off and that within the transition layer the signal is largely coherent despite this variation, see Fig. 4.6.

In conclusions, the simulations produce three standing signals at very similar periods, which

start off approximately in phase when driven by an initial pulse. Collectively, these signals form a quasi-standing mode from the lower chromosphere to the transition region over about 1000 seconds, during which period they are close enough to being in phase that they could easily be interpreted as a single standing signal. Indeed, given that *p*-modes are only observed to be coherent over about 6 periods at any given point, it seems plausible that observations might give the appearance of a single phenomenon where in fact there may be more than one mechanism at work. It is suggested that whereas previous work (Fleck & Deubner 1989; Fleck & Schmitz 1991; Leibacher et al. 1982) has attempted to explain standing modes and 200 second signals observed in the chromosphere as either generated by partial reflection at the transition region, or as the result of resonant excitation at the cut-off frequency, it is more appropriate to consider both phenomena as important, and as able to generate oscillatory signals at similar amplitudes. Having said this, the resonantly excited signals here do not occur at periods so short as 200 seconds, and it is not clear whether with different model assumptions these mechanisms would be able to generate such signals.

4.4.3 Transition region guided waves

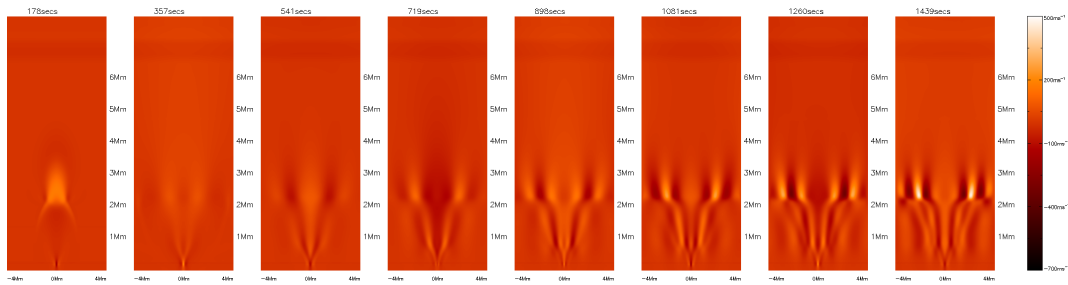


Figure 4.8: Time series of images showing the development of a guided wave at the transition region from a 300 second driven signal.

Returning to the full 2D behaviour of the simulation, Fig. 4.4a displays the propagation of the signal across a line at 1.3 Mm height, and shows the behaviour of the signal in the horizontal dimension in the chromosphere. The shape of the wavefronts at this height is much more time dependent than in the shorter period case. The first front is very narrow and quite faint on this image, impacting on 1.3 Mm after slightly less than 100 seconds, and has uniform direction of curvature, indicating that the pulse caused by the first wavefront travels up through the

atmosphere as one might expect. Just above this front, and below the first ‘thicker’ signal, is the flatter signature of the first reflected wave travelling back down the simulation from the transition region.

Above this at about 300 seconds is a much thicker wavefront. In the centre (about ± 0.7 Mm) the this signal seems to have a strong curvature suggesting upward propagation. Closer examination reveals that there is a faint wave front very similar to that of the first pulse, which is a simple upwardly propagating front. The dominant signal however is the horizontal propagation of a signal outwards from the centre. Fig. 4.5 shows these outward propagating waves, which are slanted due to the increasing sound speed. This signal is launched at the same time that the second upward wave is detected, and superposed in the centre, but has much greater amplitude because the standing wave is set up from this point on. In the chromosphere this signal is damped as it travels outwards, and the amplitude is greatly reduced beyond ± 2 Mm. However, at the transition layer the speed is greater and the transition region acts as a guide and the wave on this surface has a strong amplitude and is still strong when it leaves the domain at ± 4 Mm.

The transition region wave and the chromospheric standing wave start in phase and thus these horizontally moving wavefronts start almost coherent from chromosphere to transition. However, the transition region signal is of a higher frequency, and therefore the transition region wave becomes out of phase with the lower signal over time. This generates some complex behaviour at the interface between the chromospheric cavity and the transition layer, but it does not seem to be of crucial importance to the behaviour of the system.

Fig. 4.8 allows us to clearly see the development of this guided wave, and also makes clear the strong amplitude of these guided waves compared to the velocity signals elsewhere in the domain. The transition region guided wave has a wavelength of ~ 160 km and the period of the waves is around 300 seconds, but there is a strong variation with the period at different times and positions within the transition region covering a range $\sim 250\text{-}350$ seconds.

This guided wave (which is associated with changing vertical velocity) causes a small lifting of cool dense material into the corona. At the 270 m s^{-1} driver amplitude this movement is rather insignificant, but in runs performed at higher amplitudes for comparison the phe-

nomenon becomes more noticeable, for instance in Fig. 4.9 where there are dark protrusions rising ~ 200 km above the equilibrium height of the transition region, driven by a 760 m s^{-1} amplitude signal. Although such harmonic amplitudes are unphysical for a single point driver, this does suggest that if more energy were put into the system (by driving the whole lower boundary for instance or by driving at more than one point) that more interesting transition region behaviours might be found. This is addressed in Chapter 5.

The behaviour of the transition region is also somewhat richer in the cold chromosphere simulations, see §4.4.5.

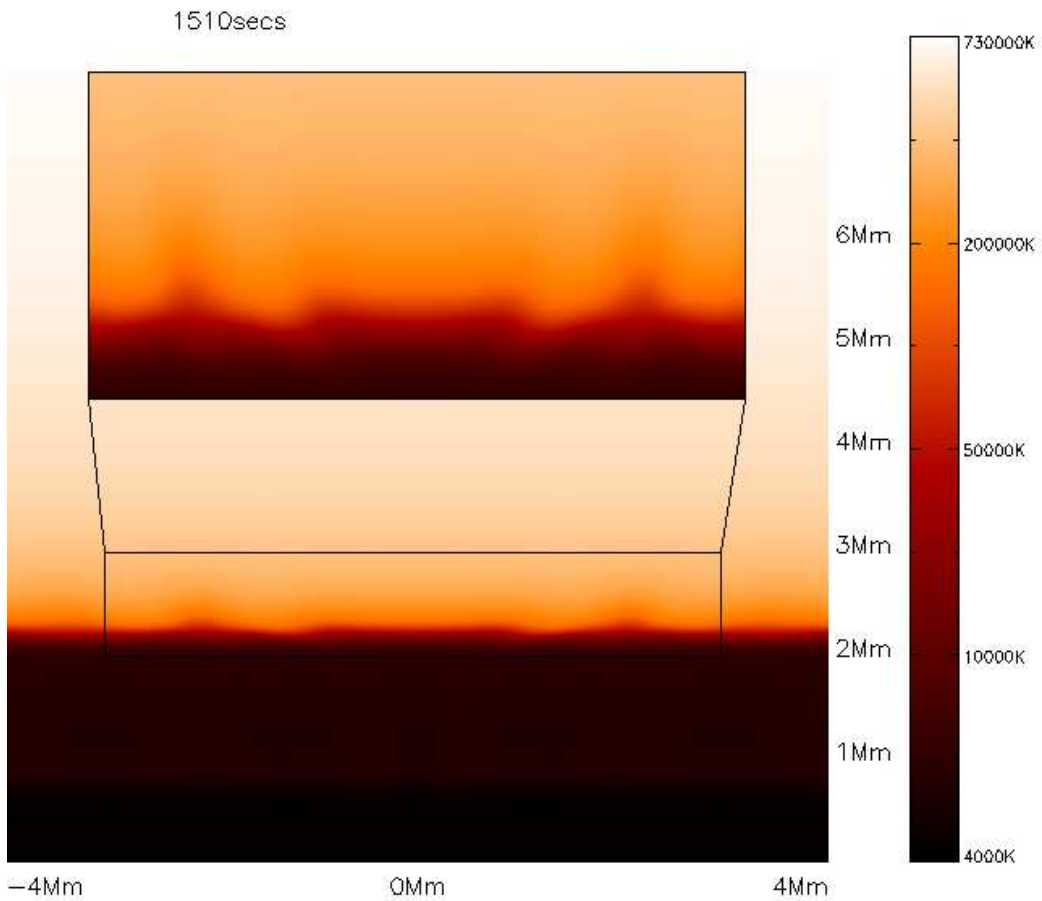


Figure 4.9: Snapshot of the log of the temperature in the computational domain for a simulation driven with an amplitude of 760 ms^{-1} , zoomed in to show the development of fine structure rising from the transition region, taken after 1510 seconds.

An initial effort has been made to find a dispersion relation which would describe the

properties observed in this guided wave, by considering the dispersion equation in e.g. Miles & Roberts (1992) for a two isothermal layer atmosphere and also considering a simple three layer atmospheric model. Neither of these models proved to be a sufficiently close approximation to the realistic simulated atmosphere that the equations were satisfied, or close to being satisfied. A full theoretical consideration of the dispersion relation for these guided waves fell outside the scope of this thesis, but might be addressed in future.

4.4.4 Cavity modes

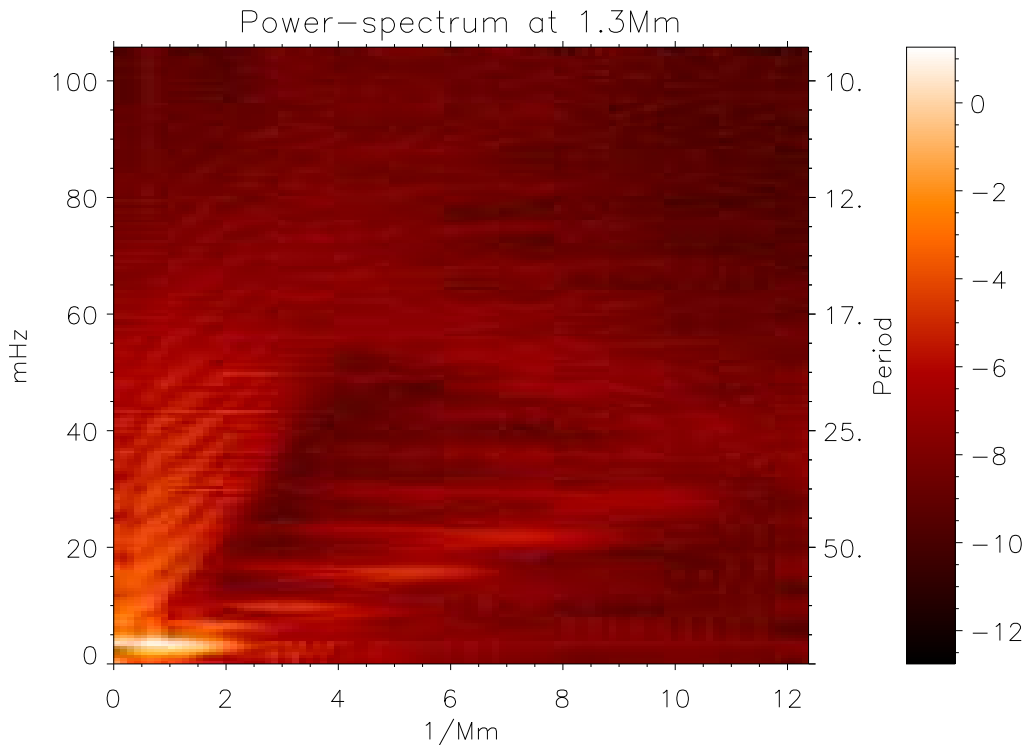


Figure 4.10: Power spectrum for the case with a 300 second driver taken along a horizontal cross-section at 1.3 Mm height.

Fig. 4.10 shows the power spectrum within the chromospheric cavity generated by the 300 second driver. It clearly reveals the signature of the standing modes being set up in the cavity, in the form of localised areas of high signal power, with the driven power showing up clearly at ~ 3.3 mHz and higher harmonics at $\sim 6.5, 10, 16$ and 22.5 mHz. The frequencies are close to the harmonics of the 5 minute signal, but the power spectrum does not resolve the frequencies well

enough to distinguish clearly between the key signal periods mentioned above. These results are consistent with the presence of a standing signal between 250 and 300 seconds in period, but would not distinguish between two different signals at such close frequencies. The response at 13.3 and 20 mHz seems somewhat weaker, but is still visible on the spectrum, and as the sound speed is constant on the cross-section along which the spectrum is taken, the localised power signals of the harmonics are in a straight line. The equivalent power spectrum taken at a position above the transition region (Fig. 4.11), contains only evidence of the driven 300 second signal, and at a lower power something of the first harmonic signal. There is nothing to generate harmonics from the fundamental signal above the transition region, rather it is evidence of leakage of power at these frequencies from the chromospheric cavity.

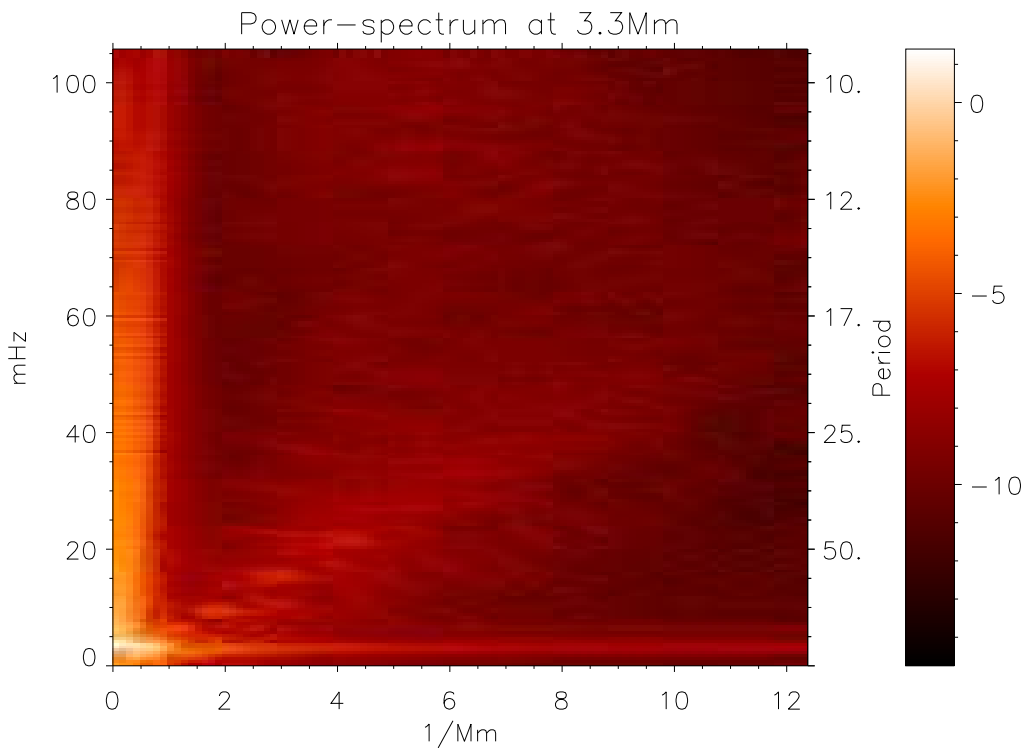


Figure 4.11: Power spectrum for the case with a 300 second driver taken along a horizontal cross-section at 3.3 Mm height.

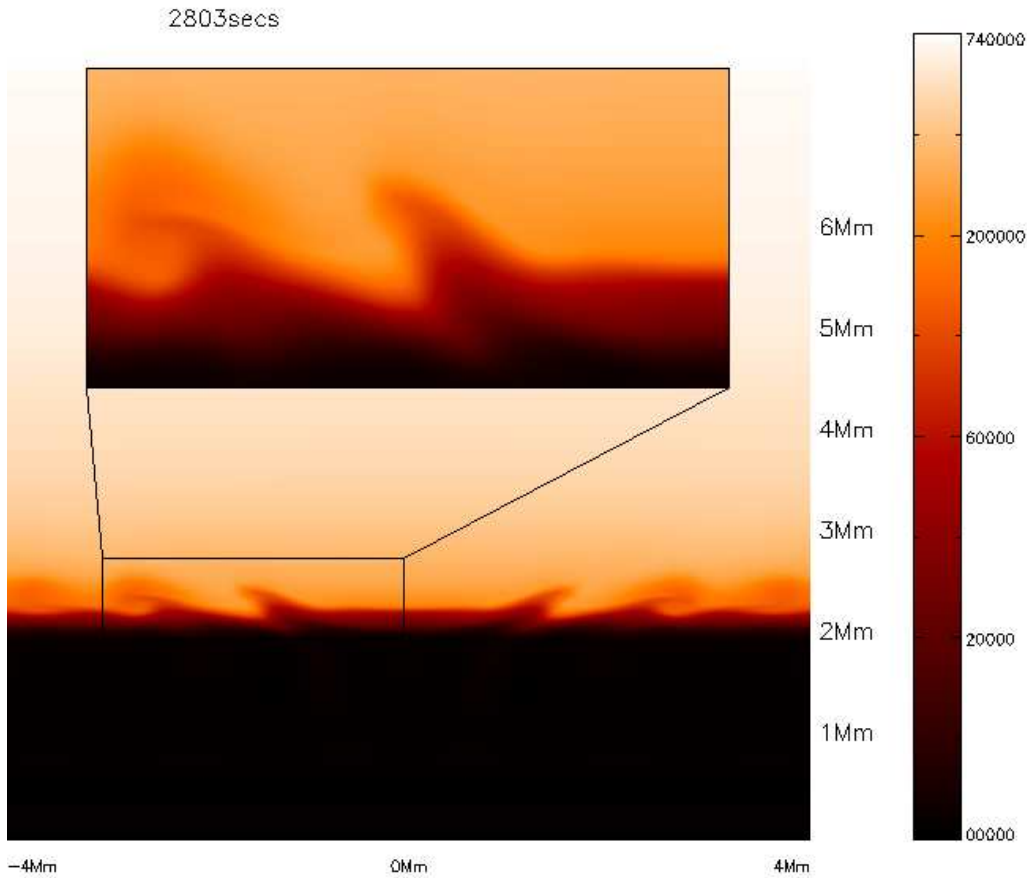


Figure 4.12: Snapshot of the log of the temperature from the cold chromospheric case with a 300 second driver, with a section of the transition region expanded to show small cold protrusions rising towards the low corona.

4.4.5 Cold chromospheric case

For the reasons mentioned in §2.1, further 300 second driven simulations have been produced using a temperature model which assumes a cold isothermal chromosphere. Most of the key results obtained are not fundamentally changed by the alternative temperature structure, however there is an important alteration in the behaviour at the transition region. In the cold chromospheric case the start of the transition region is more abrupt than in the hot chromospheric VAL IIIc, and it was found that this caused the transition region to act more effectively as a reflective surface for the upwards propagating signals. A node is formed at the reflection height directly above the driver, and the resonant transition region signal is severely limited

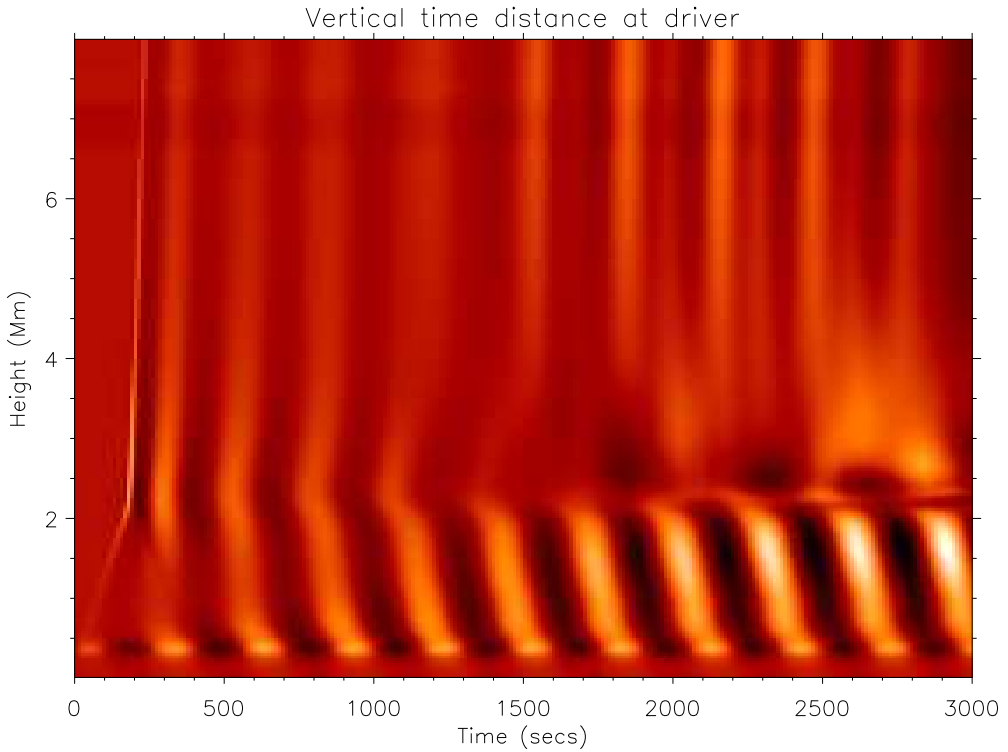


Figure 4.13: Time distance image along the central vertical axis of the computational domain showing vertical velocity.

in the centre of the domain, with the chromosphere behaving as a semi-open cavity.

Without wave energy being deposited in wake oscillations in the photosphere, more energy is channelled into the surface waves on the transition region. These surface waves are seen to drive structured protrusions into the corona, Fig. 4.12, which are more well-defined and more extensive than the coronal incursions observed in the VAL IIIc simulations.

There is no variation of cut-off period in the chromosphere now, so the signals in the photosphere/lower chromosphere and the cavity mode are at the same period, see Fig. 4.13. This differs from the well distinguished set of periods observed at different heights in the VAL IIIc case.

Nevertheless, despite various specific distinctions, the important conclusion to be drawn from these additional results is that overall the simulations are not dramatically different from the VAL IIIc results. Although the system is sensitive to the temperature structure

in the chromosphere, it is demonstrated that it is not so sensitive that conclusions based on one model cannot be relevant to another. On the other hand, the differences in behaviour apparent in these results are sufficiently interesting to suggest that the question of how the detail of chromospheric temperature structure affects p mode propagation is an interesting one which deserves further study, and that numerical models need to pay due attention to identifying appropriate models for temperature structure if they are to deliver the most useful possible results.

4.5 Summary

Simulations of the propagation of driven waves from the upper photosphere into the chromosphere and corona (in a non-magnetic case) have been carried out, and have resulted in three key results.

Firstly, the simulations have shown the strong propagation of waves driven at frequencies higher than the transition layer cut-off frequency into the corona, with relatively low reflection at the transition region.

Secondly, due to both resonant excitation of the atmosphere at the cut-off frequency and partial reflection of upwards propagating signals at the chromosphere-transition region boundary, the 300 second driver is able to set up standing waves in the chromospheric cavity, and at the photosphere and transition region. This is also true of drivers at similarly long periods from 250-350 seconds, although where the driver is more out of phase with the resonant excitations the standing waves are less clearly defined, and in the case of a driver of 450 seconds, for instance, the three signals become completely out of phase with each other over only ~ 4 periods.

Thirdly, for the 5 minute driven signal, but also for all the other drivers which have been considered (although not discussed in detail here) with periods in the range 200-400 seconds, the signals drive the formation of transition region guided waves propagating horizontally, with periods around 300 seconds and wavelength of around 160 km. This guided wave formation is of particular interest, and we intend to extend the work to a more realistic model with the aim of determining what observational signatures might be associated with such guided waves.

For all driver amplitudes we have found that the simulated waves experience stratification driven growth to a local maximum at the transition region, which is analogous to results from the active Sun of various observational studies of three minute sunspot oscillations, which have found that the observed oscillation amplitude of such waves above sunspots peaks at transition region temperatures (Brynilsen et al. 2002; Fludra 2001; Marsh & Walsh 2006; O'Shea et al. 2002).

These results were extended to a three dimensional case by Fedun et al. (2009). The three dimensional study presented in Fedun et al. (2009) supports the observations of the two dimensional modelling presented here. For a short period 30 second driver, the 3D modelling found that the signals were able (given assumptions of ideal MHD) to penetrate into the corona through the transition region, with some reflection. For the longer period 5 minute driver, the 3D modelling confirms the results presented in this chapter of the generation of transition region surface waves, and the presence of standing waves in the chromospheric cavity. It is not considered surprising that the three dimensional modelling should support the two dimensional results presented here, in particular given the cylindrical symmetry of the model used by Fedun et al. (2009). While the addition of a third dimension allows energy in the model to disperse in an additional direction, the results of this modelling are essentially linear for the driver amplitudes considered in this thesis and by Fedun et al. (2009). Hence, while the relationship between the precise amplitudes of the driver and observed transition region signals may vary between the studies, one would expect the qualitative nature of the results to be consistent - indeed, this consistency somewhat vindicates the use of the 2D simplification.

Chapter 5

Direct propagation of photospheric acoustic waves into non-magnetic solar atmosphere

5.1 Abstract

Solar p modes are one of the dominant types of coherent signals in Doppler velocity in the solar photosphere, with periods showing a power peak at five minutes. The propagation (or leakage) of these p -mode signals into the higher solar atmosphere is one of the key drivers of oscillatory motions in the higher solar chromosphere and corona. This chapter examines numerically the direct propagation of acoustic waves driven harmonically at the photosphere, into the non-magnetic solar atmosphere. In Chapter 4 the acoustic response to a single point-source driver was investigated. This chapter extends the work to more structured, coherent, photospheric drivers mimicking solar global oscillations. When the model atmosphere is driven with a pair of point drivers separated in space, reflection at the transition region causes cavity oscillations in the lower chromosphere, and amplification and cavity resonance of waves at the transition region generate strong surface oscillations. When driven with a widely horizontally coherent velocity signal, cavity modes are caused in the chromosphere, surface waves occur at the transition region, and fine structures are generated extending from a dynamic transition region into the lower corona, even in the absence of a magnetic field.

The results presented in this Chapter are the results published by Malins & Erdélyi (2007).

5.2 Introduction

In Chapter 4 (see also Erdélyi et al. 2007) we studied the propagation of waves driven by a single harmonic point vertical-velocity driver from the upper solar photosphere to the solar corona. It was demonstrated that in such cases, driving the atmosphere at the 5 minute period would generate surface waves propagating along the transition region and that the chromosphere could act as a cavity, potentially leading to the generation of chromospheric standing waves.

The driver amplitudes applied in the point driven case were not high enough to cause significant movement of cool, dense material upwards into the corona (De Pontieu et al. 2004, c.f.), but there was evidence (c.f. Fig. 4.9) of small, cold, dense structures being lifted upwards above the transition region. It was commented in §4.4.3 that if additional energy were input to the system, it seemed possible that the driven signals might cause more substantial movement of cool dense material upwards.

The point driver was used because of its simplicity, because a simple driver makes it relatively easy to analyse results, and because a point driver provides a certain degree of comparability with results from one dimensional modelling. In reality, the Sun does not often provide simple point harmonic drivers, and therefore it is instructive to consider alternative driver geometries. In this chapter, the study of the propagation of acoustic waves into the non-magnetic solar atmosphere is extended from the results for a single point driver by examining different spatially structured driver configurations.

In Chapter 4 results were presented for short period (30 s) driven waves, demonstrating that short period signals are able to traverse the transition region into the corona without transferring substantial energy to wake oscillations. It was remarked that on the real Sun, non-ideal phenomena would be expected to strongly damp such short period signals. Having made the point that the response of the simulated atmosphere to long period signals is significantly different to its response at short periods, there is little to be gained from repeating short period simulations with structured drivers. Hence, the synthetic drivers used in the simulations in this chapter are given periods of around 5 minutes, which of course corresponds to the longer period driver results presented in Chapter 4, and the dominant power of the solar global p modes.

In §2.4 and Chapter 4 the local acoustic cut-off period was discussed, both theoretically and in specific relation to the simulations in which an equilibrium atmosphere was perturbed by a point driver. Recall that the VAL IIIc atmosphere is divided into four distinct regions for 5 minute oscillations by the varying cut-off period. These are respectively; the region around the temperature minimum, in which the cut-off period is below 5 minutes and oscillations will be evanescent; the chromospheric cavity in which the cut-off period increases to an approximately constant value slightly above 5 minutes, and oscillations will propagate; the transition region where the cut-off reduces to a minimum perhaps as short as 100 seconds; the corona in which the cut-off period is long.

When applying structured drivers, it is again expected that cut-off period oscillations will be excited, especially in the regions of short cut-off. It is also expected that signals will be again reflected at the transition region—in Chapter 4 such reflections were observed to contribute to the generation of standing waves in the chromospheric cavity, which has been previously suggested as the source of three minute transition region oscillations (Leibacher et al. 1982).^m

In this chapter, two additional types of driver geometry are applied. In the first case, instead of applying a single driver in the middle of the domain, two drivers are applied, 1.5 Mm from the centre to the left and right respectively. These act in the same way as the single point driver investigated in Chapter 4—i.e. vertical-velocity perturbations, varying sinusoidally in time. Three examples of this paired driver are investigated: a pair of harmonic drivers with exactly a 5 minute period and in phase; a pair of harmonic drivers with a period of exactly 5 minutes and out of phase in time by π radians; a pair of drivers one of which is at the 5 minute period exactly, and the other of which is at a period of 270 seconds. The third case is particularly important as a comparison to results from the more symmetric cases. Oscillations at different points on the surface of the real Sun would rarely be exactly in phase or display identical periods.

In the second driver geometry, simulations have been carried out for two cases of horizontally coherent driver. These horizontally coherent configurations are pertinent as in the real Sun photospheric *p*-mode oscillations have a horizontal wavelength and coherence. The two cases are a driver with a wavelength of 10 Mm, applied along the middle 5 Mm of the base of the computational domain, with sinusoidal horizontal amplitude dependence (a ‘fundamental

mode') and a driver with wavelength 5 Mm applied in the same way (the 'first harmonic').

5.3 Multiple Drivers

By considering a combination of point drivers, it is possible to examine the way in which signals propagating from different spatial locations and with different phases might interact with each other in the solar atmosphere. As the Sun's surface is highly dynamic, it is highly unlikely that one single point source on the real Sun would exist in the effective absence of other signals, and hence considering this interference may assist in understanding observed solar phenomena.

Looking at a pair of point drivers acting on an equilibrium atmosphere is still a gross simplification compared to the real Sun. As in Chapter 4 it is hoped that examining a relatively easy to analyse case will be instructive in consideration of real solar phenomena.

5.3.1 In-phase drivers

The first example of these paired point harmonic drivers is a pair of point drivers oscillating in phase. Fig. 5.1 is a snapshot of the vertical velocity in the computational domain, taken

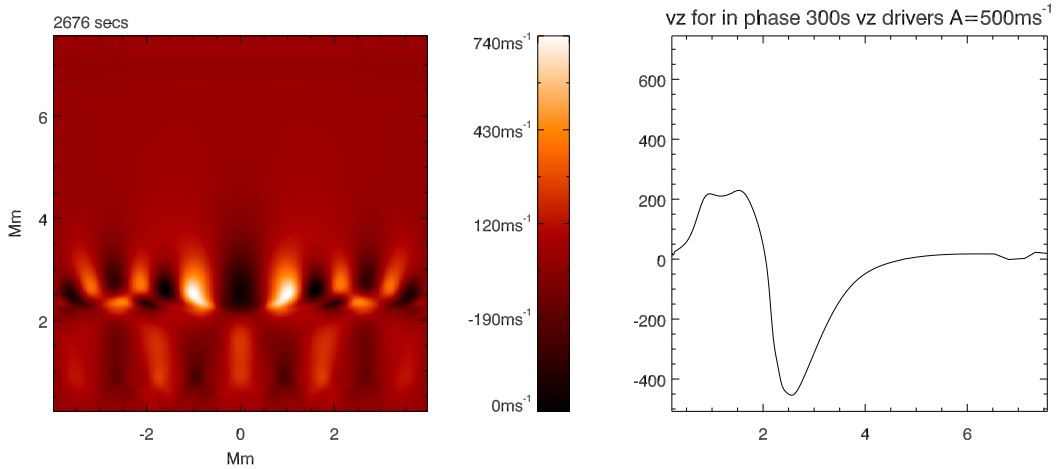


Figure 5.1: Snapshot of the vertical velocity in the computational domain after 2676 seconds for two in-phase 5 minute drivers, on the left looking at the whole domain, and on the right a plot of vertical velocity along a central vertical line.

after 2676 seconds, after nearly ten driver periods. Reminiscent of the results from Chapter 4, in the chromospheric cavity there is a clear pattern of alternating positive and negative velocity. After this amount of time has elapsed in the simulation, there is a signal very close to a standing wave pattern in the region between the two drivers, where the reflection from the transition region interacts with interference of the signals.

At the transition region, again just as in Chapter 4, a surface wave forms. Due to the stratification driven amplification of acoustic signals at the transition region, and the resonant excitation of modes at the cut-off period, it is at the transition region that the highest velocity amplitudes present in the simulations are observed.

Whereas in the previous chapter the surface waves propagated outwards along the transition region from a point directly above the driver, there are now wave components propagating in each direction in the region between the two drivers. In the centre of the domain where the amplitudes of the two signals are well matched, this in-phase interference results in a standing oscillation over ≈ 2 Mm horizontally at the centre of the transition region. It would be of great interest to confirm the existence of these predicted transition region surface waves by the available high resolution space instruments currently available (*e.g.* *Hinode*'s EIS camera).

By looking at the temperature in the simulation, it is possible to determine whether the surface waves are driving any significant motion of the transition region, or are causing cool dense material to be lifted into the corona (c.f. solar spicules etc). It is found that the waves drive a gentle undulation in the height of the transition region. This change in height is only of the order of 100 km, and at these amplitudes there is no lifting of larger cool structures into the corona.

5.3.2 Drivers out of phase by π radians

Now consider the case where the wave sources are out of phase by exactly π radians. Fig. 5.2a shows the propagation of the signals across a horizontal line at a height of 1.3 Mm, in the chromospheric cavity. The signals propagating from the two drivers clearly interfere with each other, with the most pronounced interference pattern manifesting in the centre of the domain, where the amplitudes of the two signals are relatively well matched. As in the single driver

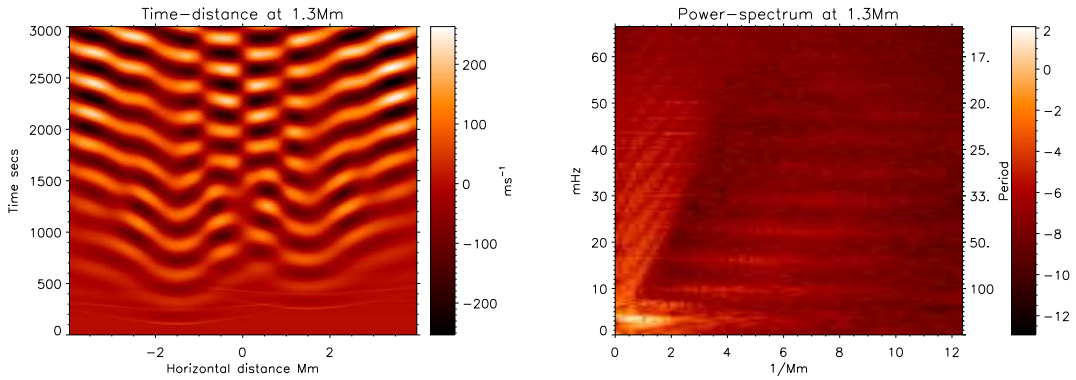


Figure 5.2: a) Time-distance image for a pair of drivers out of phase by π radians showing vertical velocity along a horizontal line taken at 1.3 Mm into the atmosphere (in the chromosphere). b) Corresponding power spectrum for a line at height 1.3 Mm in the chromosphere.

case, on each side we first see the initial pulse crossing propagating through, visible as a narrow bright wavefront, then we see a second wavefront with lower amplitude and lower curvature, which corresponds to the reflection from the first pulse. The dominant behaviour after this first pulse-reflection cycle shifts to broader light and dark peaks and troughs, as the resonantly excited cut-off frequency modes in the photosphere and transition region become dominant over the driver. The highest amplitudes are recorded at the end of the simulation, demonstrating that increasingly large amounts of energy are being deposited from the drivers into the chromospheric cavity, with the amplitude at points of positive interferences still growing even after 3000 seconds.

Fig. 5.2b shows the corresponding power spectrum in the chromosphere. Notice that as well as a power peak at the driven period, there are significantly smaller but discernible power peaks for the harmonics of the signal. This matches earlier findings for a single driver (c.f. Chapter 4), and demonstrates that the chromosphere acts as a resonant cavity.

Having considered the behaviour in the chromospheric cavity specifically, let us draw back and examine the signal behaviour on the whole of the domain. Fig. 5.3 is a typical vertical-velocity snapshot from late in the simulation. In the chromospheric cavity we see the alternating light and dark vertical bands that are characteristic of a standing wave in the cavity, much as were observed for a single driver. This is consistent with the observation of peaks in

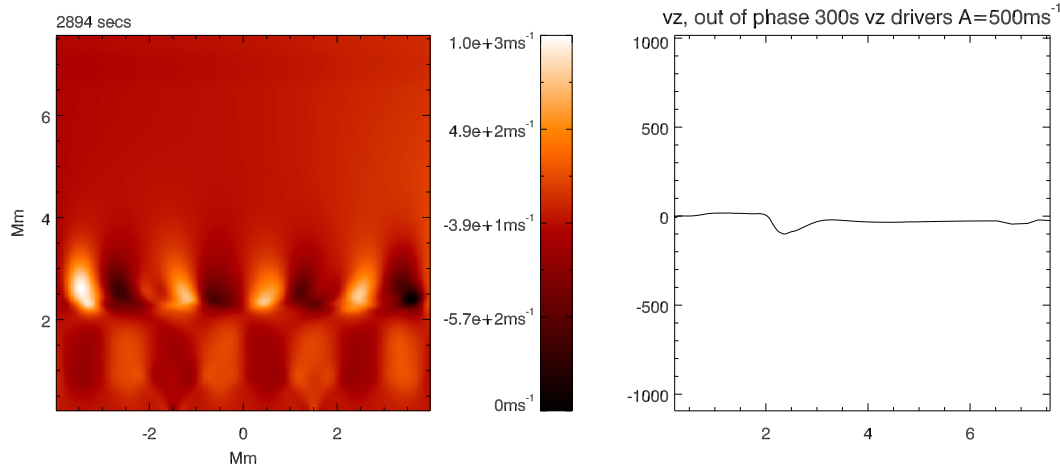


Figure 5.3: As in Fig. 5.1, but after 2894 seconds for two out-of-phase 5 minute drivers.

the power spectrum at the harmonic frequencies of the driver.

At the transition region, surface waves are again clearly visible. As previously, the amplitude of the vertical velocity perturbations achieves a maximum at the transition layer. The surface waves have similar properties to the in-phase case, but display a simpler configuration of peaks and troughs, due to the different interference pattern set up by the out of phase drivers. In both this case and the case with in-phase drivers, the chromospheric standing wave and transition region surface wave become out of phase with each other, supporting the conclusion from Chapter 4 that there are waves with different but similar periods being driven in each of the photosphere, chromosphere and transition region.

The surface wave is associated with a granulation of the transition region into circulation cells. Fig. 5.4 depicts the direction of flow of plasma at the transition region against the variation from the background temperature. In this image it can also be seen that in the corona, the dominant flow direction is now horizontal even though two vertical velocity drivers were used. This is examined in more detail in Chapter 6.

5.3.3 Drivers with slightly different periods

Finally, we look at the application of a pair of drivers one of which is at exactly 300 second period, and the other of which has a period of 270 seconds. In this third case, the interference

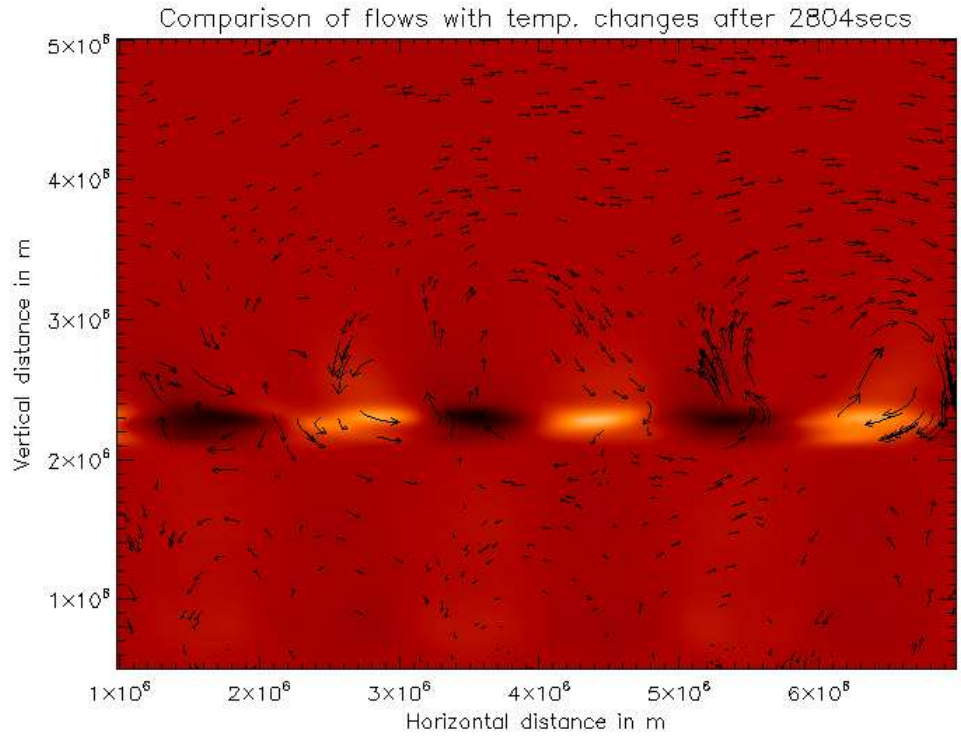


Figure 5.4: Arrows representing the magnitude and direction of the flow are superimposed on an image of the change from equilibrium temperature (brighter areas are hotter) in a region of the domain centred on the transition region.

between the signals is, predictably, more inhomogeneous.

Fig. 5.5 is a representative snapshot of the behaviour in the full domain towards the end of the simulation. The behaviour of the signal in the chromospheric cavity is no longer similar on left and right. One can still make out the vertical bands that are suggestive of a standing wave, but they are of varying thickness and strength. There are also still power peaks for the harmonics in the power spectrum, indicating that the chromosphere continues to act as a resonant cavity for the signals to an extent, but it is not possible to identify a persistent standing wave at any single location in the cavity (given the resolution of the power spectrum, it is also not possible to resolve whether there are different power peaks from the different drivers).

Just as the behaviour in the chromospheric cavity is relatively inhomogeneous now, so in

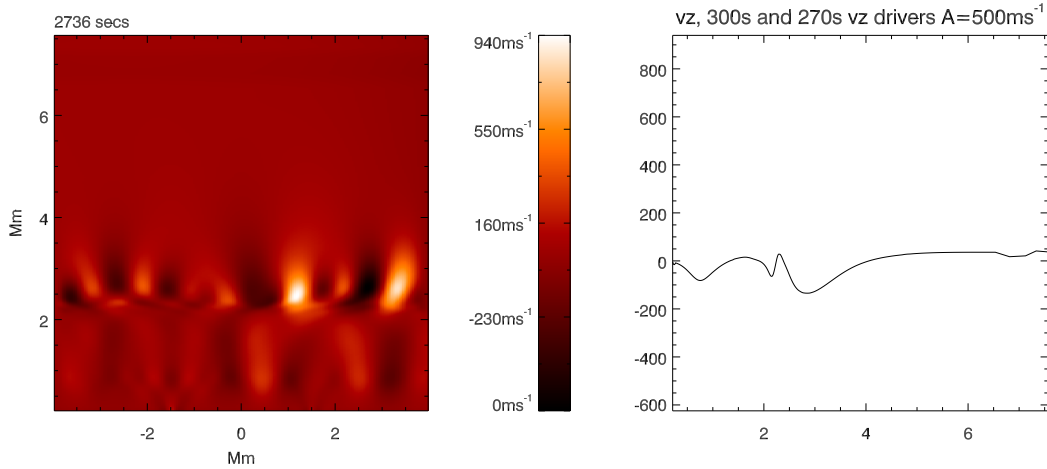


Figure 5.5: As in Fig. 5.1 but after 2736 seconds for drivers with period 5 minutes (left driver) and 270 seconds (right driver).

In this example it can be seen that due to destructive and constructive interference of signals the surface-wave amplitude is relatively inhomogeneous. In this frame, the right hand side has stronger surface wave amplitudes, while in the centre the waves are damped. This spatial variation in transition region surface wave amplitude is the key indicator of the asymmetric driving. It seems plausible that similar patterns of constructive and destructive interference on the real Sun could lead to locally enhanced amplitudes of transition region surface waves. These could potentially result in localised lifting of chromospheric material into the corona.

5.4 Wide Coherent Driver

Simulations using both cases (i.e. the fundamental and the first harmonic) of the wide drivers are run with amplitudes of 100 m s^{-1} , 250 m s^{-1} and 500 m s^{-1} .

5.4.1 ‘Fundamental’ mode

Fig. 5.6 shows a series of snapshots of the temperature in the computational domain in the ‘fundamental’ mode case for a driver amplitude of 500 m s^{-1} . A strong surface wave is set up again at the transition region, the height of which oscillates by $\approx \pm 300 \text{ km}$ in the centre of the domain.

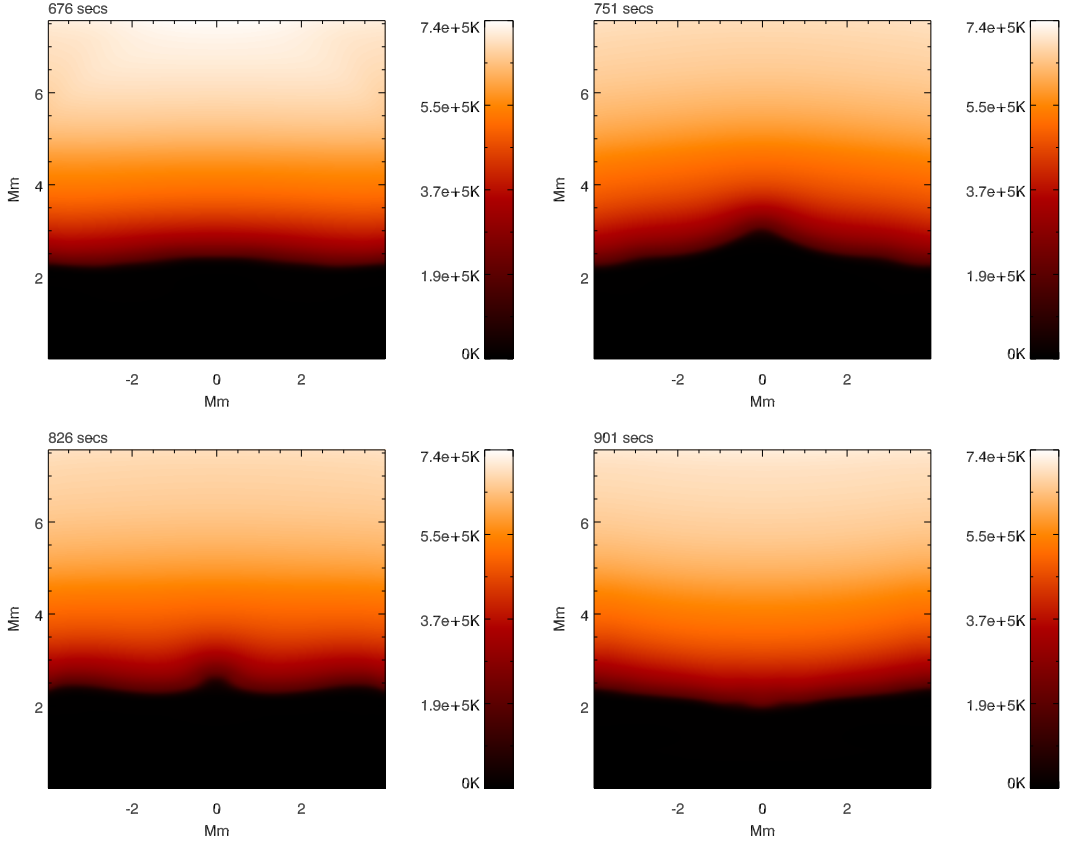


Figure 5.6: Set of snapshots of the log of temperature in the computational domain for the fundamental driver.

The surface wave has a structure which is largely similar to the driver structure beneath it, but as can be seen particularly in the third frame of Fig. 5.6 there is some development of localised ‘protrusions’ on the transition surface.

Fig. 5.7 shows the vertical-velocity signal measured at a point in the transition region. The signal has two clear beats, which implies that there are two signals of similar frequencies interfering. This beating does not only occur at the transition region, but is present from the upper photosphere upwards. It is suggested that one of the beating signals is the 5 minute driven frequency. Given this, and based on the beat period of ≈ 1500 seconds the second other signal should have a period of ≈ 250 seconds. Based on the ubiquity in height of the beating and the fact that the beating seems to start immediately, it seems likely that this 250

second signal derives from the resonant wake oscillation in the photosphere. This is consistent with the photospheric/lower chromospheric cut-off period (at which the resonant response is expected), which varies over a range $\approx 230\text{--}300$ seconds.

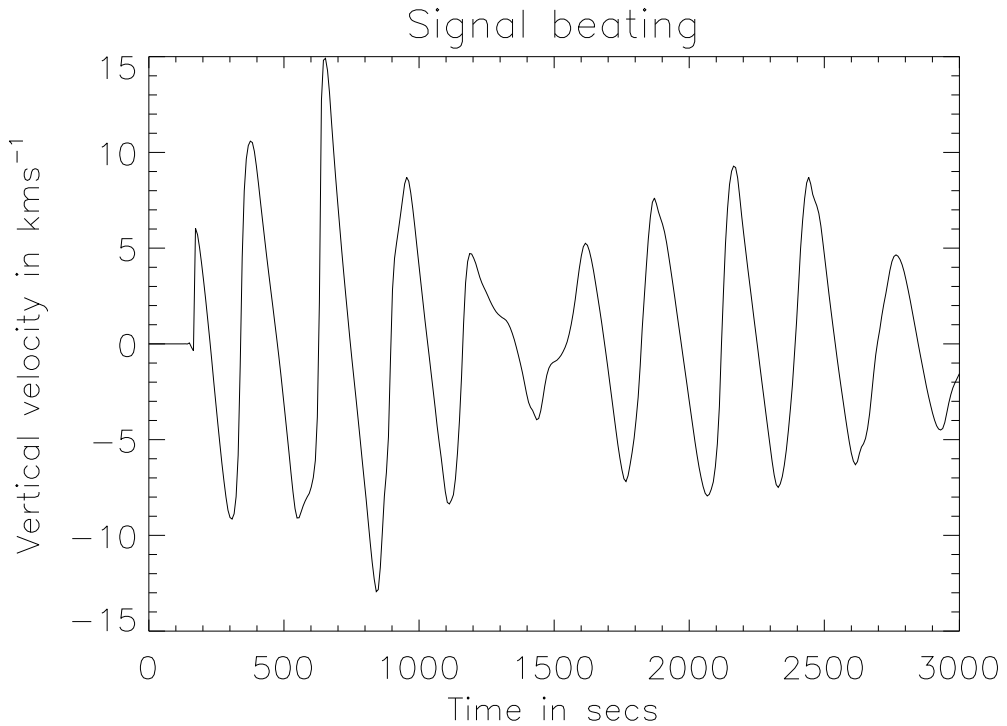


Figure 5.7: Signal in vertical velocity at 2.3 Mm height (transition region) in the horizontal centre of the domain.

5.4.2 ‘First harmonic’

The ‘first-harmonic’ driver generates some much more dynamic behaviour. Figure 5.8 shows a sequence of snapshots of the temperature in the simulation, with a driver amplitude of 500 m s^{-1} . In the first frame, taken at 900 seconds, there is a clear undulation in the height of the transition region, which matches the horizontal configuration of the driven signal. There is also some sign of fine structures on a scale of about 0.5 Mm being generated, extending into the corona. In the next three frames, the underlying surface wave is still apparent, but the turbulence and fine structures in the lower corona become much more prominent, and there

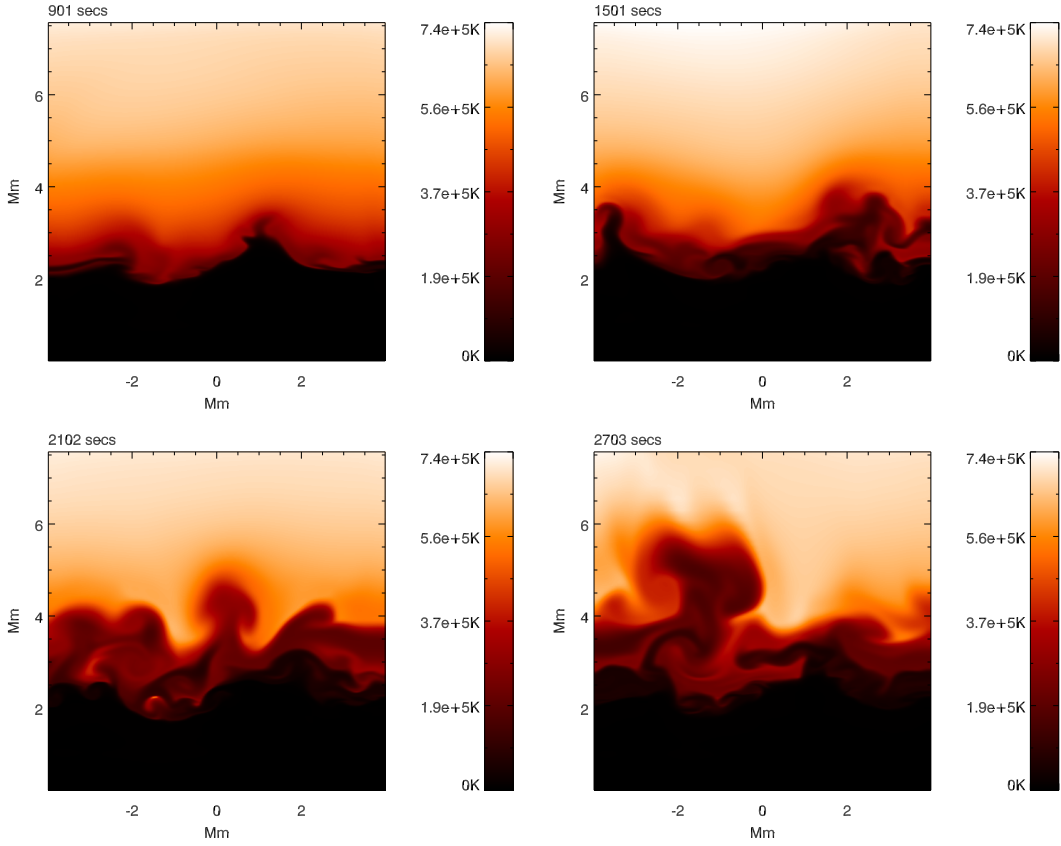


Figure 5.8: Set of snapshots of the log of temperature in the computational domain for the first harmonic wide driver.

is a general lifting of cooler chromospheric material into the corona. In particular, there is a ‘mushroom’ structure of material at $\approx 30,000$ K on the left which extends as high as ≈ 3.5 Mm above the equilibrium height of the transition region, with a width of \approx two Mm. This is a structure on a similar vertical scale to small solar spicules.

The first-harmonic driver does not experience the strong beating present for the fundamental mode, which is unsurprising given the horizontal structure of the driver.

The figures presented above for the wide drivers have a driver amplitude of 500 m s^{-1} . In lower-amplitude-driver cases which were also investigated, it was found (as one might expect) that there was significantly less movement of material into the corona. There is still some development of fine structures for the lower amplitudes, and the underlying surface undulation

of the transition region is observed at all amplitudes.

5.4.3 Chromospheric cavity

The chromosphere continues to act as a cavity despite the significant disturbance to the local height of the transition region. On power spectra taken in the chromosphere for both the 10 Mm and 5 Mm horizontal wavelength drivers, power peaks are observed corresponding to the first few harmonics of the driven 5 minute signal.

5.5 Summary

It has been shown that the surface waves on the transition region that were demonstrated in Chapter 4 in the case of a harmonic point vertical-velocity driver, recur in a case where the atmosphere is perturbed with spatially structured (*e.g.* a pair of such) drivers. Transition-region surface waves are also generated when the atmosphere is driven by a horizontally-coherent signal, but in this case the horizontal wavelength of the surface waves is correspondingly increased. It is suggested that if these surface waves were to be observed, it would be in Doppler-velocity measurements taken at transition region temperatures. It is anticipated that it would be much harder to find these oscillations in intensity or emission-measure imaging observations.

The standing waves in the chromosphere are reproduced in the case of a pair of drivers, in positions determined by the driver geometry, and limited to cases where there is a symmetry between the drivers. In the more general case, quasi-standing modes may still be able to exist in the chromosphere for short times when signals interfere in the right way. Power spectrum analysis of signals in the chromosphere suggest that it acts as a cavity (Leibacher et al. 1982, c.f.) for all of the spatially structured drivers considered.

Finally, it has been shown that fine structures on a much larger scale than those found for the single point driver are generated by driving the base of the computational domain with a 5 Mm horizontal wavelength 5 minute signal at 500 m s^{-1} , and that there is some small-scale structure demonstrated even at lower amplitudes, and to some extent by a 10 Mm wavelength signal. It is suggested that shorter horizontal coherences, or otherwise more locally inhomogeneous drivers, may be associated with increasingly dynamic impacts on transition

region behaviours.

Chapter 6

Transition region granulation driven by synthetic photospheric motions

6.1 Abstract

This chapter examines the way that transition region surface waves, generated in 2-D numerical simulations of the non-magnetic solar atmosphere when various synthetic photospheric drivers are applied, drive the granulation of the transition region/lower corona. It is shown that these cells are generated by both synthetic point drivers and synthetic horizontally coherent *p*-mode drivers. These cells cause the conversion of driven signals in vertical velocity into coronal signals predominantly in horizontal velocity, which if carried over to a case with a magnetic field included could cause mode conversion.

This chapter presents results published by Malins (2007).

6.2 Introduction

In this chapter additional examination is made of the transition region surface waves identified as a key feature of the simulations presented in Chapters 4 and 5. Particular attention is paid to the flows associated with the surface waves, and it is suggested that they drive the granulation of the transition region/lower coronal region into circulation cells. It is shown that such granulation is generated by both synthetic point drivers and synthetic horizontally coherent *p*-mode drivers. These cells are associated with the conversion of driven signals

associated predominantly with variations in vertical velocity into propagating coronal signals associated predominantly with variations in horizontal velocity. If carried over to a case with a magnetic field included such generation of horizontal motion from a vertical perturbation could cause mode conversion.

6.3 Transition region granulation

6.3.1 Point drivers

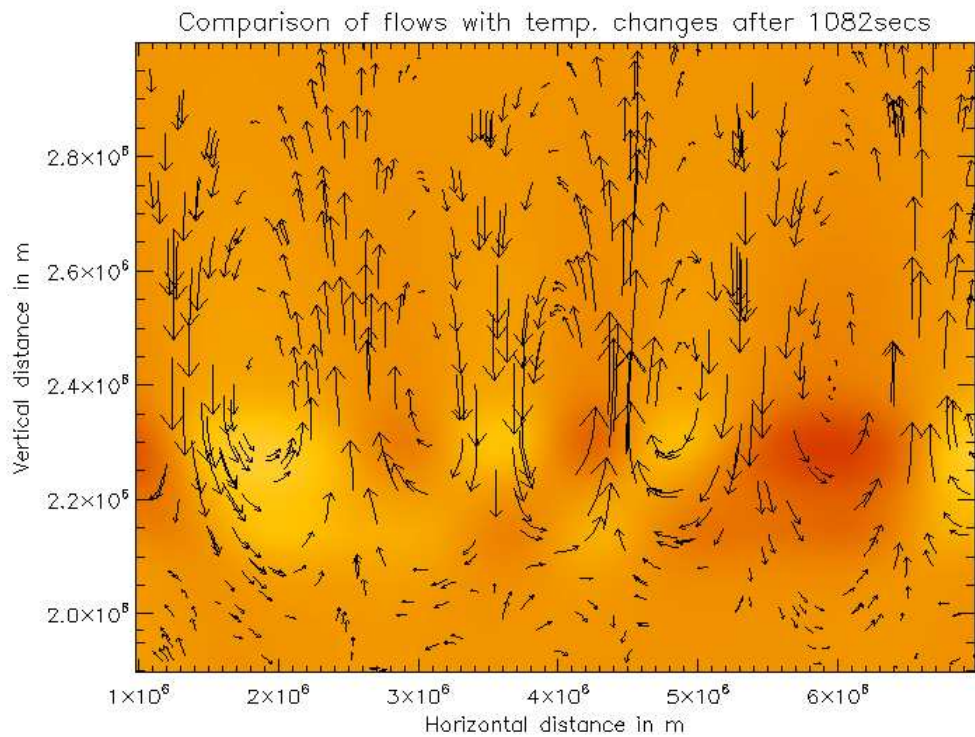


Figure 6.1: Arrows with length proportional to speed of flows at the transition region, superimposed on an image showing changes from the equilibrium temperature (brighter is hotter than equilibrium, darker is cooler), after 1082 seconds.

In Chapter 5, it was noted that in simulations where a model atmosphere is driven with a pair of point vertical velocity drivers, there is a potential resultant granulation of the transition region. This phenomenon is examined in more detail here, specifically for the case where the atmosphere is driven with two 300 second period point drivers, exactly π radians out of phase.

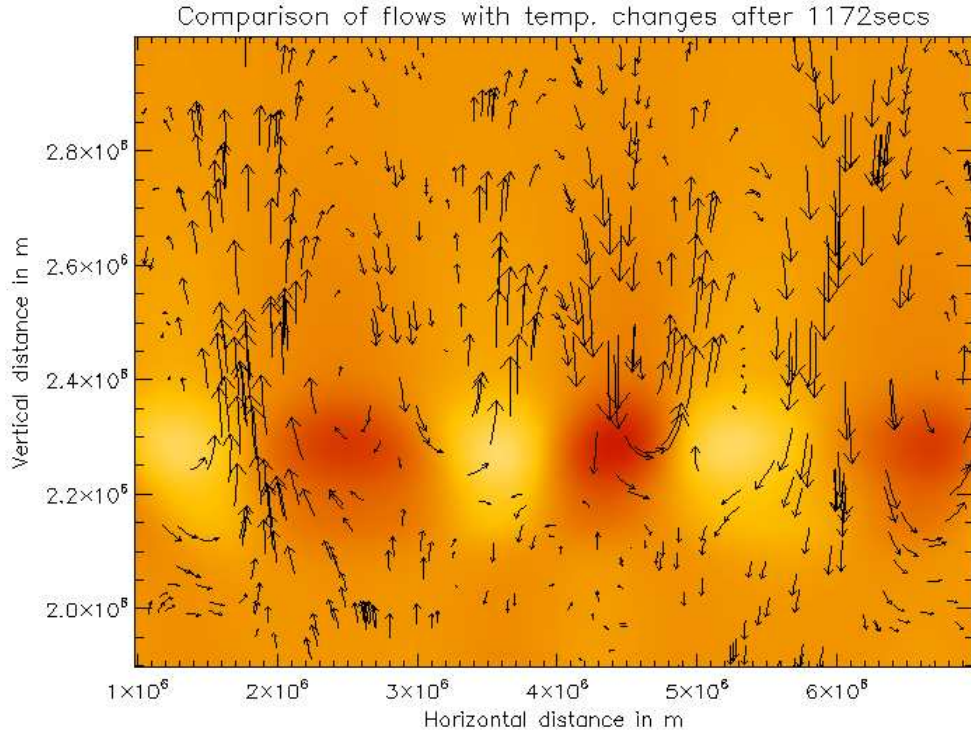


Figure 6.2: As Fig. 6.1 but taken after 1172 seconds.

Figures 6.1 and 6.2 are snapshot images taken after 1082 and 1172 seconds of simulation time respectively, showing arrows in the direction of flows at the transition region, with length proportional to the speed of the flows. These representations of the vector velocity are superimposed on images representing the departure of the atmospheric temperature from the equilibrium value. In Fig. 6.1 there are five distinct circulation cells. These cells extend from approximately 2.1 Mm height to 2.75 Mm height, and the velocities around each cell are comparable. It is important to note that because the image has been ‘zoomed’ in at transition region height, while still covering 6 Mm in width, the arrows are distorted such that a ‘vertical flow arrow’ is longer than the ‘horizontal flow arrow’ for the equivalent speed of flow. These cells can be clearly seen to be associated with changes in the background temperature.

In Fig. 6.1 the surface waves can be seen as temperature variations most noticeably from

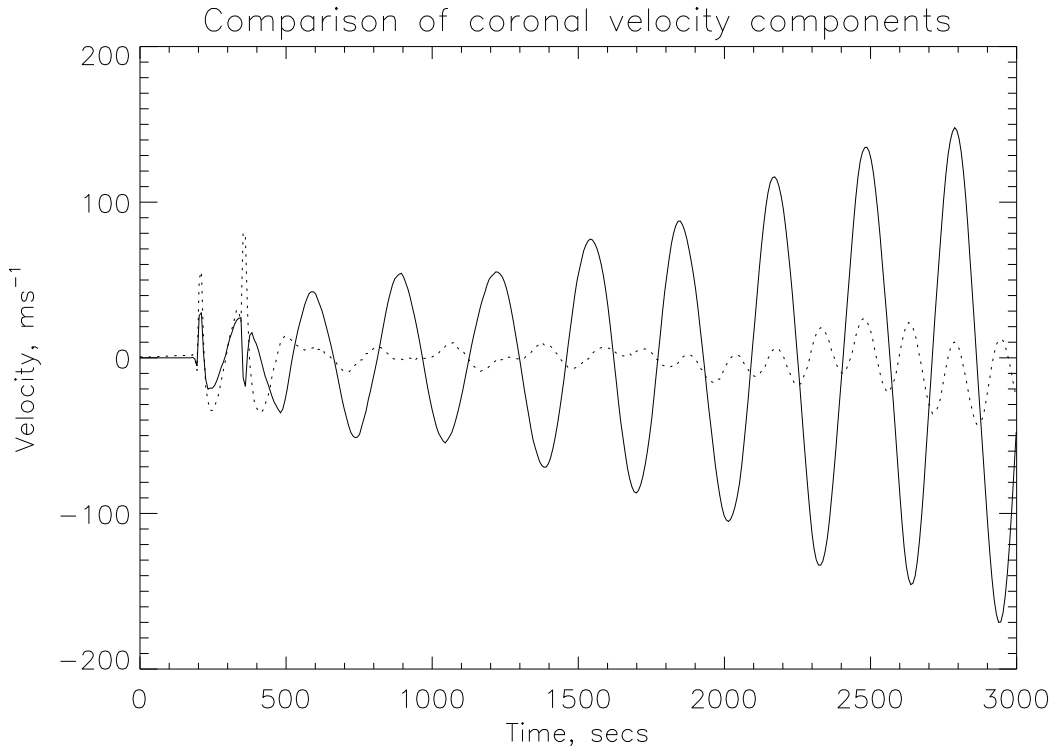


Figure 6.3: Comparison of velocity components in the vertical and horizontal directions taken at a height of 5.3 Mm in the horizontal centre of the domain, for case driven by two 300 second point drivers with a phase difference of π . Solid line is horizontal component, dotted line is vertical.

2.1-2.3 Mm. Comparing with Fig. 6.2 however the temperature variations are small. This snapshot, taken 110 seconds later (about half a period for the transition region waves) shows the point where the strong temperature deviation at the transition region is causing the reversal of the flows. At the cell boundaries, the flows reverse from upwards to downwards every half period of the surface waves.

The presence of these transition region granules causes a change of velocity alignment in the waves which are transmitted into the corona. The drivers are both 300 second period vertical velocity signals, however in the corona above the cells the dominant velocity associated with the transmitted wave is horizontal. In Fig. 6.3 this is made very clear by comparing the horizontal and vertical velocity components at a point in the centre of the domain horizontally, and 5 Mm up vertically - right in the middle of the coronal region of the domain.

Whereas the vertical component of the signal (dotted line) is weak ($< 20 \text{ ms}^{-1}$), the horizontal component is much stronger, with an amplitude of about 150 ms^{-1} by the end of the simulation. This amplitude can be seen to be steadily increasing. It is not entirely clear without extending the simulation whether this growth would continue, would level out, or constitutes for example the growth phase of a beat, c.f. §5.4.1. It suggests that energy is being built up in the surface wave and circulation cells, and then leaking away into the corona as horizontal velocity waves.

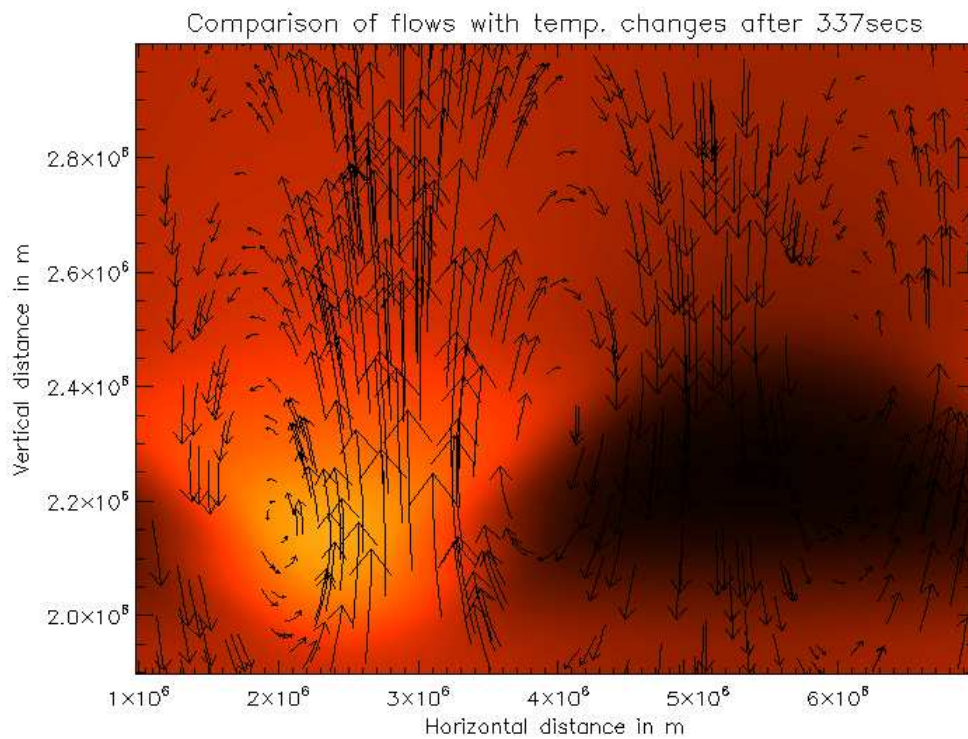


Figure 6.4: As in Fig. 6.1 but for case of ‘first harmonic’ horizontally coherent driver with 300 second period and 250 ms^{-1} amplitude, taken after 330 seconds.

6.3.2 Horizontally coherent driver

In Chapter 5, a synthetic sinusoidal driver horizontally coherent over 5 Mm is also considered, representing solar global oscillations. Recall that there were two cases—a ‘fundamental mode’ case with a horizontal wavelength of 10 Mm, and a ‘first harmonic’ case with a wavelength

of 5 Mm. The ‘first harmonic’ driver has some similarities to the out of phase point drivers considered above, in the sense that the left side of the driver is out of phase by π with the right side of the driver, and similar granulation occurs at the transition region.

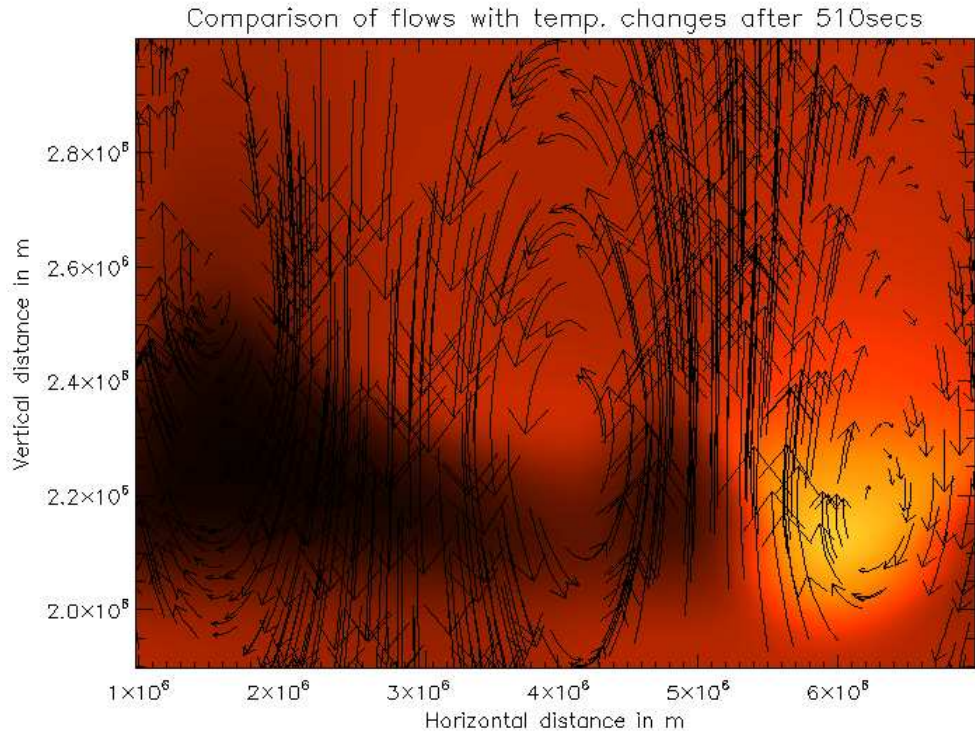


Figure 6.5: As in Fig. 6.1 but for case of ‘first harmonic’ horizontally coherent driver with 300 second period and 250 ms^{-1} amplitude, taken after 503 seconds.

Fig. 6.4 has three clear circulation cells present. The bright region on the left shows an increase from equilibrium temperature, i.e. the transition region height has dropped on this side due to the surface wave. The cell on the left is lower, as it is associated with the dynamic transition region, and manifests from about 1.7–2.7 Mm height (partially below the frame of the figure). On the right the transition region has been raised by the surface wave, hence the dark region. On this side, the cell is higher, extending from about 2–2.9 Mm in height. In Fig. 6.5 the situation is similar, but it is taken about half a period later, and thus the cell rotation is reversed and the right hand cell is now lower than the left hand one.

As in the case with two point drivers, these cells convert the vertical motion present in

the driver to a predominantly horizontal motion in the signal which leaks into the corona. In Fig. 6.6 this is clearly demonstrated, with the horizontal velocity signal in the corona typically having over twice the amplitude of the vertical velocity signal. In this case, note that the amplitude of the horizontal signal is not growing with time. For the horizontally coherent case, the surface wave is not progressively absorbing additional energy from the driver.

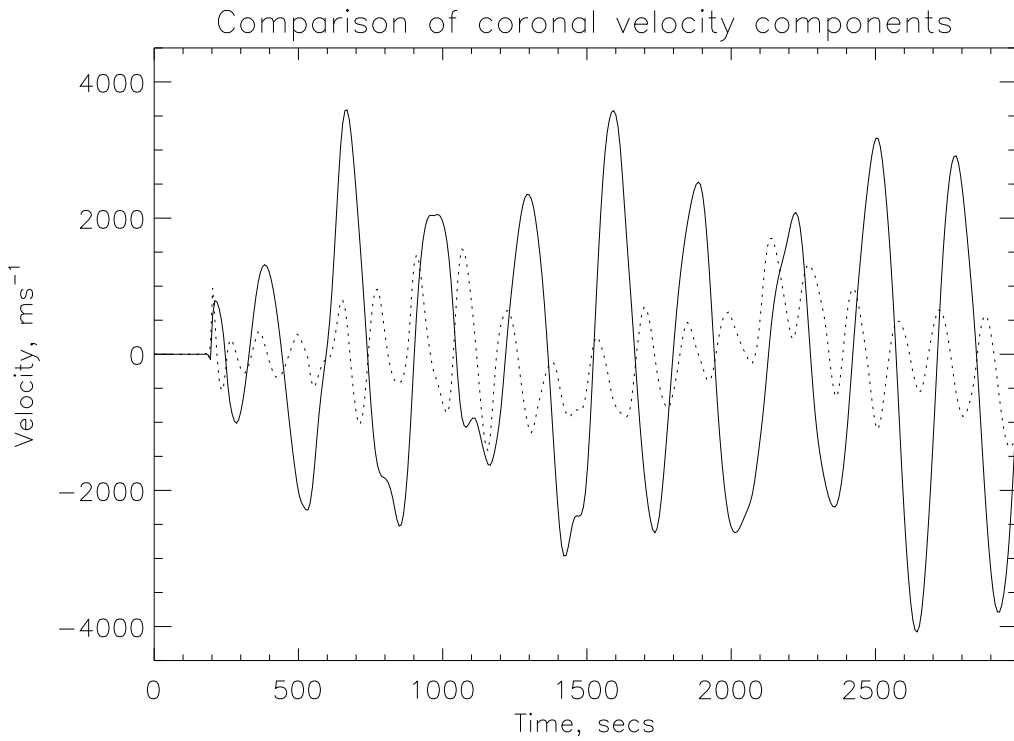


Figure 6.6: As in Fig. 6.3 but for case of ‘first harmonic’ horizontally coherent driver with 300 second period and 250 ms^{-1} amplitude.

6.4 Summary

It has been shown in this chapter that transition region surface waves, which are found in the numerical forward modelling presented in Chapters 4 and 5, drive granulation into circulation cells at the transition region. It is further shown that these cells result in the conversion of driven waves predominantly manifesting as vertical velocity, or longitudinal, perturbations to waves whose predominant perturbations are in horizontal velocity, transverse to the direction

of wave propagation. In a regime with a magnetic field, such a change in the direction of motion relative to the direction of propagation could potentially have implications for mode conversion. Mode conversion is a necessity for efficient resonant heating (Erdélyi, Goossens, & Ruderman 1995; Erdélyi & Goossens 1994; Erdélyi 1998; McDougall & Hood 2007) and these simulations may have further implications for the energy budget of the solar corona.

Chapter 7

Propagation of synthetically driven photospheric acoustic waves into the atmosphere of the quiet Sun

7.1 Abstract

In previous chapters, a non-magnetic model solar atmosphere was treated as an approximation to the quiet Sun. In this chapter, the results are extended to consideration of a simplified quiet Sun magnetic field - a uniform 10 Gauss vertical field. The response of this magnetised model atmosphere to perturbation by a point harmonic vertical velocity driver is investigated.

As in the non-magnetic simulations, the resonant excitation of modes at the cut-off frequency both in the photosphere and at the transition region is linked to the generation of quasi-standing modes in the chromosphere and transition region surface waves. These resonances occur at the local cut-off frequency, providing a mechanism for the generation of shorter period signals by the 5 minute *p*-mode oscillations. In contrast to the non-magnetic case, the magnetic field acts as a waveguide for magnetic waves, allowing the more substantial leakage of energy from the transition region surface waves into the corona as slow modes.

7.2 Introduction

In Chapters 4 and 5, results were presented from simulations in which a non-magnetic solar atmosphere was driven with synthetic oscillatory signals. This non-magnetic case was presented

as an approximation to the quiet Sun.

In this chapter, results are presented in which similar synthetic drivers are applied to a solar atmosphere with a uniform magnetic field of 10 Gauss. The uniform field is used as a simplified approximation to the real magnetic field. In the real Sun, in general the magnetic field, in particular in the photosphere and chromosphere, would be stronger and more structured. The use of a uniform field is made for reasons of numerical simplicity. The differences observed between the results obtained in these simulations and those presented in Chapters 4 and 5 indicate the effect of a quiet Sun-type magnetic field on the propagation of oscillatory signals in the Sun's lower atmosphere.

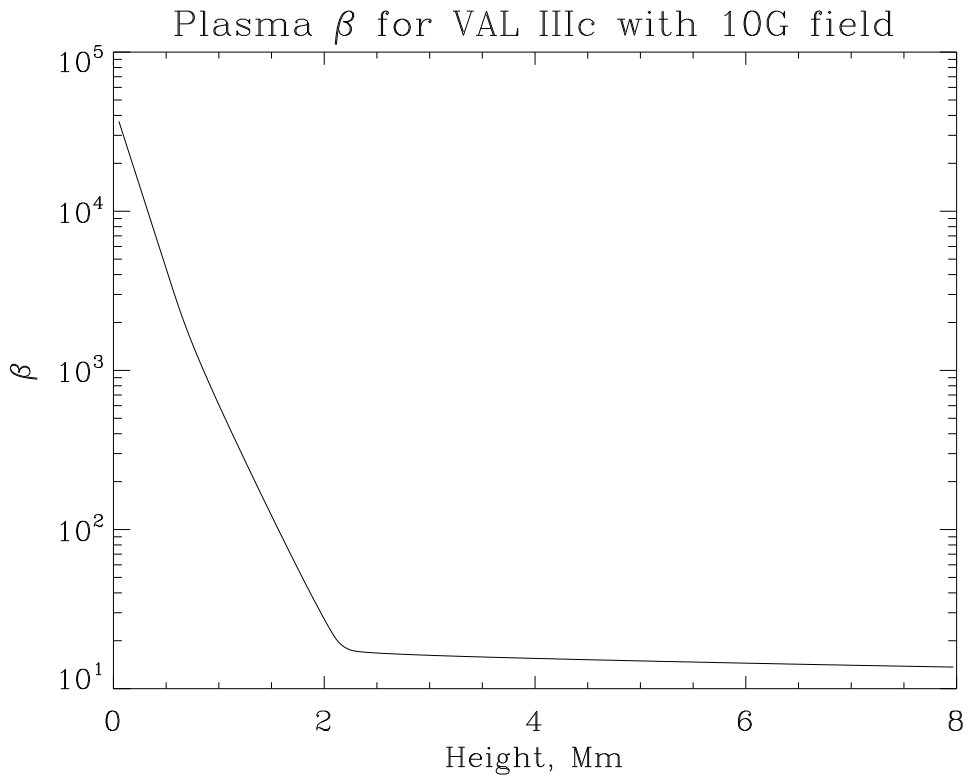


Figure 7.1: Plasma β in the equilibrium domain.

As in Chapters 4, 5 and 6, the model atmosphere is constructed based on the VAL IIIc lower atmosphere and McWhirter et al. (1975) corona, under the condition of hydrostatic equilibrium (c.f. §2.1). In §2.1, it was pointed out that while it was possible to construct an atmosphere with a temperature profile exactly determined by the VAL and McWhirter

data, the pressure and density would depart somewhat from the semi-empirically modelled values (being set to match the semi-empirical expectation at height 0). This was caused by the non-inclusion in the hydrostatic equilibrium of more complicated physical terms, in particular a turbulent pressure term modelled in VAL IIIc based on a varying microvelocity. For the hydrodynamic simulations, this was of little importance - the key parameters determining the behaviour of propagating signals in the HD case, sound speed and cut-off period, were dependent on temperature (i.e. the ratio of pressure and density).

In the MHD simulations presented in this chapter, however, there is one key parameter that is dependent on pressure with no density term - the plasma beta. The plasma beta is proportional to the thermal pressure, so any variation in pressure from the semi-empirical models will change the simulated beta. While the pressure, and hence plasma beta, is correct for a 10 G typical solar atmosphere at the sun's surface, in the corona there is a difference of over two orders of magnitude between the (higher) simulated thermal pressure and the (lower) thermal pressure predicted by VAL IIIc/McWhirter. The beta is proportionately increased.

In the simulations, therefore, with a 10 Gauss field, the photosphere and chromosphere are in a high beta regime with the thermal pressure dominating the magnetic pressure, as illustrated in Fig. 7.2. In the corona, it can be seen that the pressures are relatively close, with $\beta \sim 15$. However, beta is nevertheless $\gg 1$, showing that the thermal pressure dominates the magnetic pressure at all heights. It is found that the coronal plasma beta is more consistent with a real Sun magnetic field of order 1 Gauss than 10 Gauss, and thus the results presented in this Chapter should be considered likely to be better indicators of the coronal behaviour of signals propagating in fields of < 1 G than of 10 G. Without modelling additional complicated physical processes, however, it is impossible to make all of temperature, pressure and density consistent with the semi-empirical modelling at all heights.

As magnetoacoustic waves in the model atmosphere are always in a high beta regime, the fast speed parallel to the field matches the sound speed (increasing for waves propagating at an angle), while the slow speed parallel to the field matches the Alfvén speed (reducing for waves propagating at an angle, c.f. §2.3).

The sound speed is uniformly higher than the Alfvén speed throughout the domain, as

demonstrated in Fig. 7.2. Normally, one would expect that mode mixing might occur when the sound and Alfvén speeds are similar, when $\beta = 1$. This would occur at the transition region for stronger uniform fields above about 40G (Fedun et al. 2009). In the simulations presented here, strong mode mixing would not be anticipated, as even in the transition region and corona the sound speed is ~ 4 times higher than the Alfvén speed.

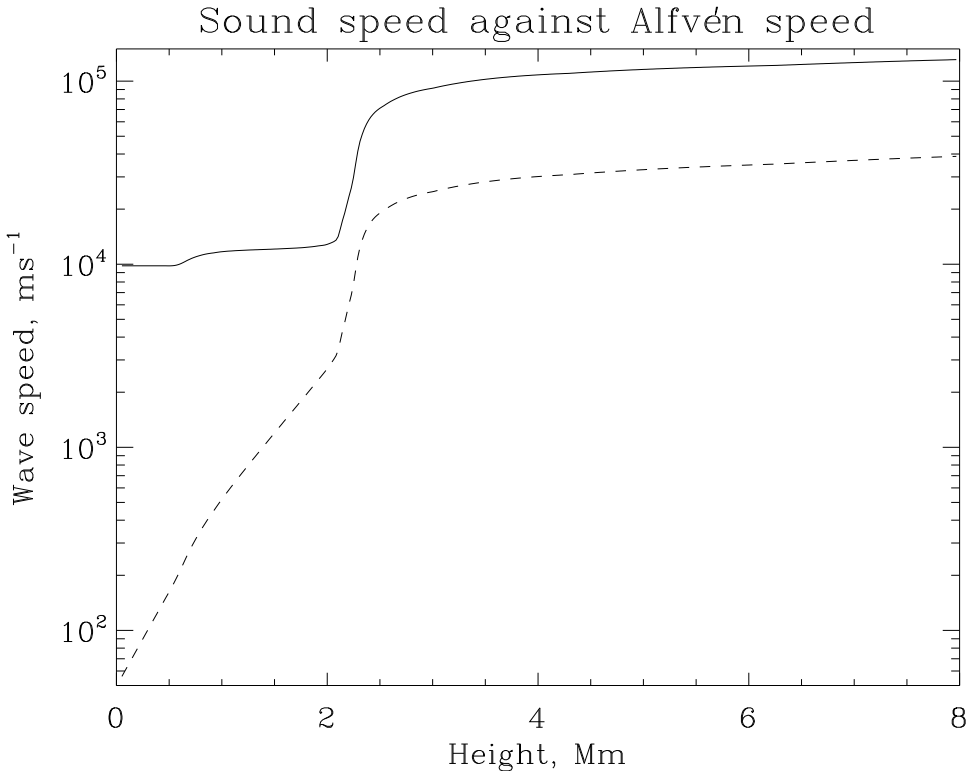


Figure 7.2: Sound speed (solid line) and Alfvén speed (dashed line) in the equilibrium domain.

The simulations presented in this chapter are analogous to the 3D simulations presented by Fedun et al. (2009). Fedun et al. (2009), also using the SAC, model the propagation of signals driven with a 30 second period and a 300 second period into the VAL IIIc/McWhirter atmosphere with a 40 Gauss uniform magnetic field. For the 5 minute synthetic oscillations modelled here, they find that much as in the non-magnetic case modelled in Chapter 4 transition region surface waves are formed propagating horizontally outward from the point directly above the driver. They find that both fast and slow modes are generated in the high beta photosphere by the synthetic driver, and that the magnetic field acts as a waveguide allowing

energy to be carried into the corona by the slow mode.

7.3 Results

7.3.1 Fast mode

In §4.4, results were presented in which a 300 second synthetic point driver was used to perturb the non-magnetic VAL atmosphere. As you will recall, this examination of the 300 s signal is of proportionately more interest than our consideration of the shorter period 30 s signal. This is both because 300 s is the period of several oscillatory phenomena in the observed Sun (e.g. oscillations observed in coronal loops with footpoints in plage regions (De Moortel et al. 2002a,b); oscillations in transition region moss (De Pontieu et al. 2003a, 2005); and the dominant *p*-mode period in the photosphere) and because the assumptions of ideal MHD that underly the simulations are more appropriate to longer period waves - the 30 s signal would be heavily damped by non-ideal phenomena, preventing significant propagation to the upper atmosphere in the real Sun.

As in Chapter 4, the driver is a vertical velocity driver applied at a height of ~ 200 km. While several driver amplitudes were investigated, in the case presented here the amplitude of the driver is 140 ms^{-1} .

Fig. 7.3 shows a series of snapshots of the vertical velocity in the computational domain. The first two frames, taken at 105 seconds and 142 seconds respectively, show the initial pulse travelling up through the chromospheric cavity to the transition region. At this stage the results are extremely similar to the results from the non-magnetic case. The wavefront propagates upwards from the driver application point, dispersing outwards in much the same way as the sounds waves driven in the non-magnetic case do.

In the photosphere and chromosphere, the 10 Gauss field corresponds to a high beta plasma, in which the sound speed is substantially higher than the Alfvén speed. The initial wavefront visible in these frames is a fast magnetoacoustic wave, travelling parallel to the field (in the vertical direction) at the local sound speed. In the photosphere and chromosphere the sound speed is of the order of 10^4 ms^{-1} , gradually increasing towards the transition region due to the temperature stratification of the atmosphere.

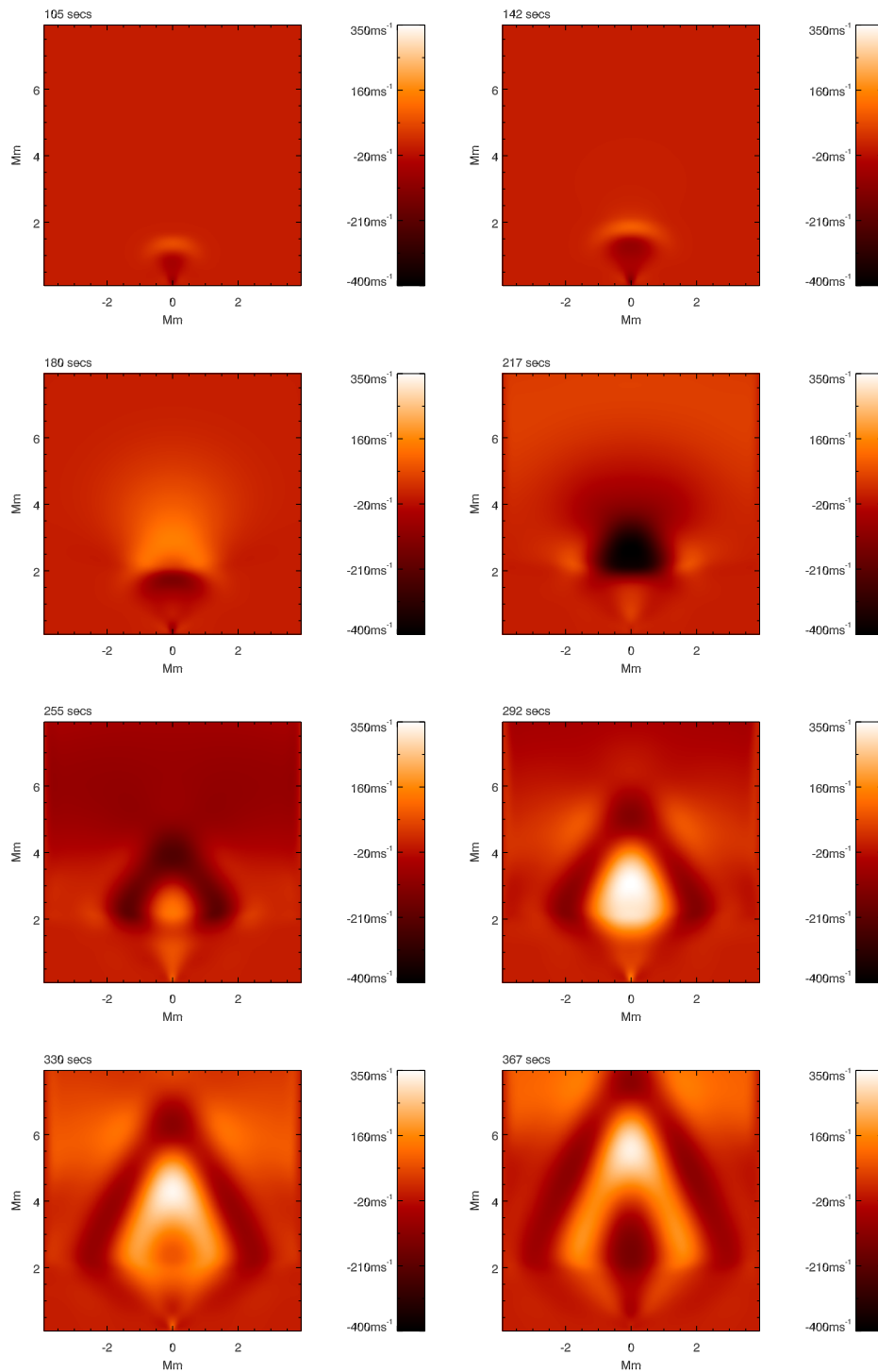


Figure 7.3: Series of snapshots of the vertical velocity in the computational domain taken at 37.5 second intervals.

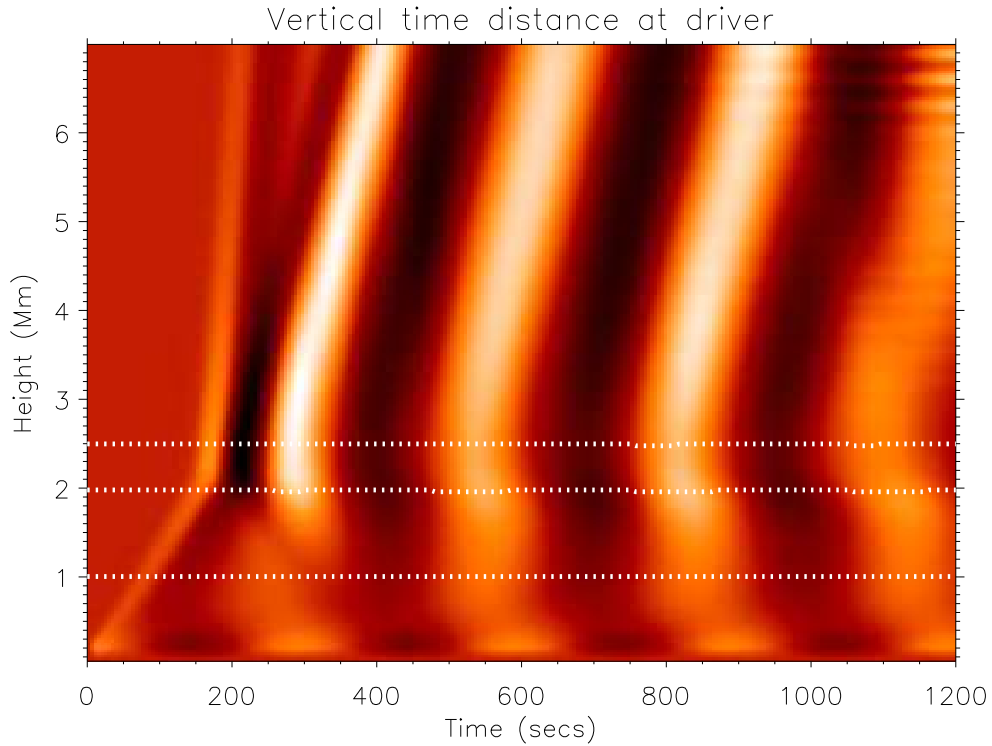


Figure 7.4: Time difference image showing the propagation of signals along a line drawn vertically through the driver application point.

As in Chapter 4, it is instructive to consider a time distance representation of signal propagation along a vertical line through the point of driver application (see Fig. 7.4). The initial fast mode pulse is clearly discernible on this representation, travelling in the photosphere/chromosphere with an approximately constant speed (visible as a well defined slanted straight line). When the signal reaches the transition region, just as in the non-magnetic case, we see the signal being partially reflected, with the reflected fast-mode signal propagating back down the domain. This fast mode signal and the subsequent reflected and transmitted components have been highlighted with white lines on Fig. 7.5.

The reflection is significantly weaker in the 10 Gauss field case than in the earlier non-magnetic simulation (Chapter 4), with the magnetic field acting to guide the wave into the corona as a transmitted fast mode signal. The amplitude in vertical velocity of the transmitted signal peaks at the transition region (reaching around 200 ms^{-1}). As the signal is a fast mode

it disperses into the corona in all directions, and hence reduces in amplitude with height.

The Alfvén speed in the photosphere/chromosphere, in contrast, is of the order of 10^3 ms $^{-1}$. In the high beta regime that applies throughout the simulations, slow mode signals should propagate parallel to the field at this Alfvén velocity. On Fig. 7.4 a second signal can be seen propagating at the slower Alfvén speed in the wake of the fast mode wavefront marked with a white line. Similarly one can identify slow mode signals propagating from the driver after each peak and trough henceforth. These slow modes have been highlighted on Fig. 7.5 with dark lines. These signals are faint and could potentially be a misdiagnosed manifestation of wake oscillations etc. However, the excitation by the driver of both fast and slow mode signals is consistent with Bogdan et al. (2003); Fedun et al. (2009). It is certainly the case that any slow mode driven signal is of relatively low amplitude - the bulk of the driver energy is initially transferred into the fast mode.

While a slow mode would be confined by the magnetic field, and prevented from propagating out in the horizontal direction, the fast mode is able to propagate in all directions much like a sound wave in a non-magnetised medium. The fast speed increases as the angle between the wave vector and the field increases to $\pi/2$ (c.f. 2.3) and hence the wavefront shows a slight ‘flattening’ in the middle. It is noted that the wave front is also more dispersed vertically than in the non-magnetic case.

7.3.2 Transition region surface wave

The initial wavefront reaches the transition region after around 150 seconds. Looking to the right on the time difference image, between the dotted lines that delineate the region of reduced cut-off period at the transition region, there is a second local maximum in vertical velocity after about 250 seconds. This is too soon for a second driven signal to have reached the transition region, occurring at about the same time as the second velocity peak of the driver. It is also too soon for a reflected signal to have returned from the base of the computational domain.

The interpretation of this transition region signal is that just as in the non-magnetic simulations presented in Chapters 4 and 5, the initial fast mode pulse propagating from the driver causes resonant wake oscillations at the cut-off period both in the photosphere/lower chromo-

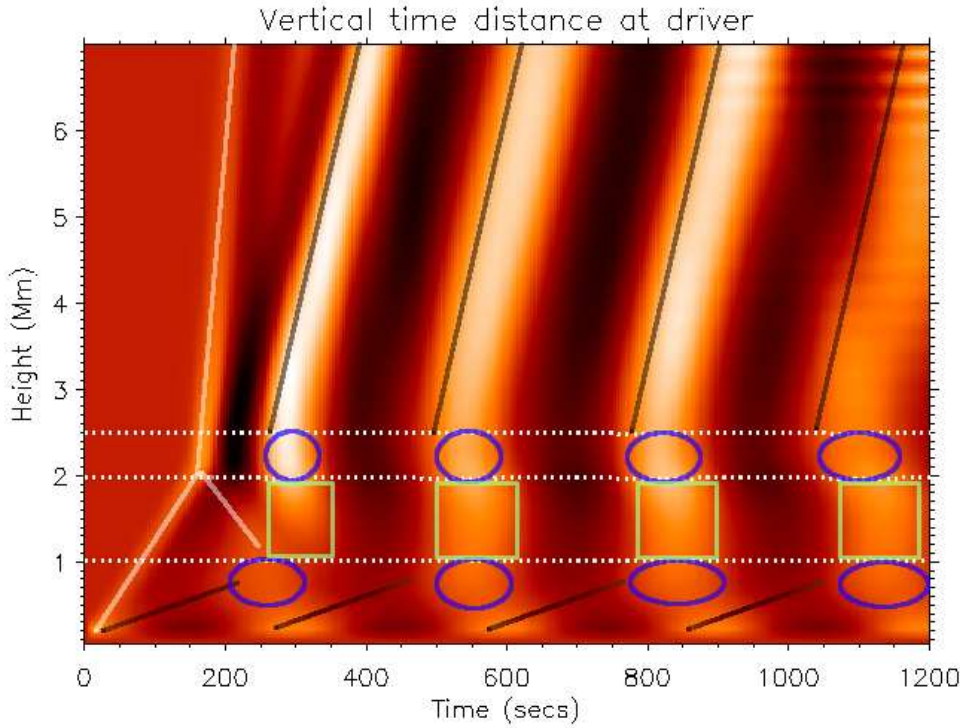
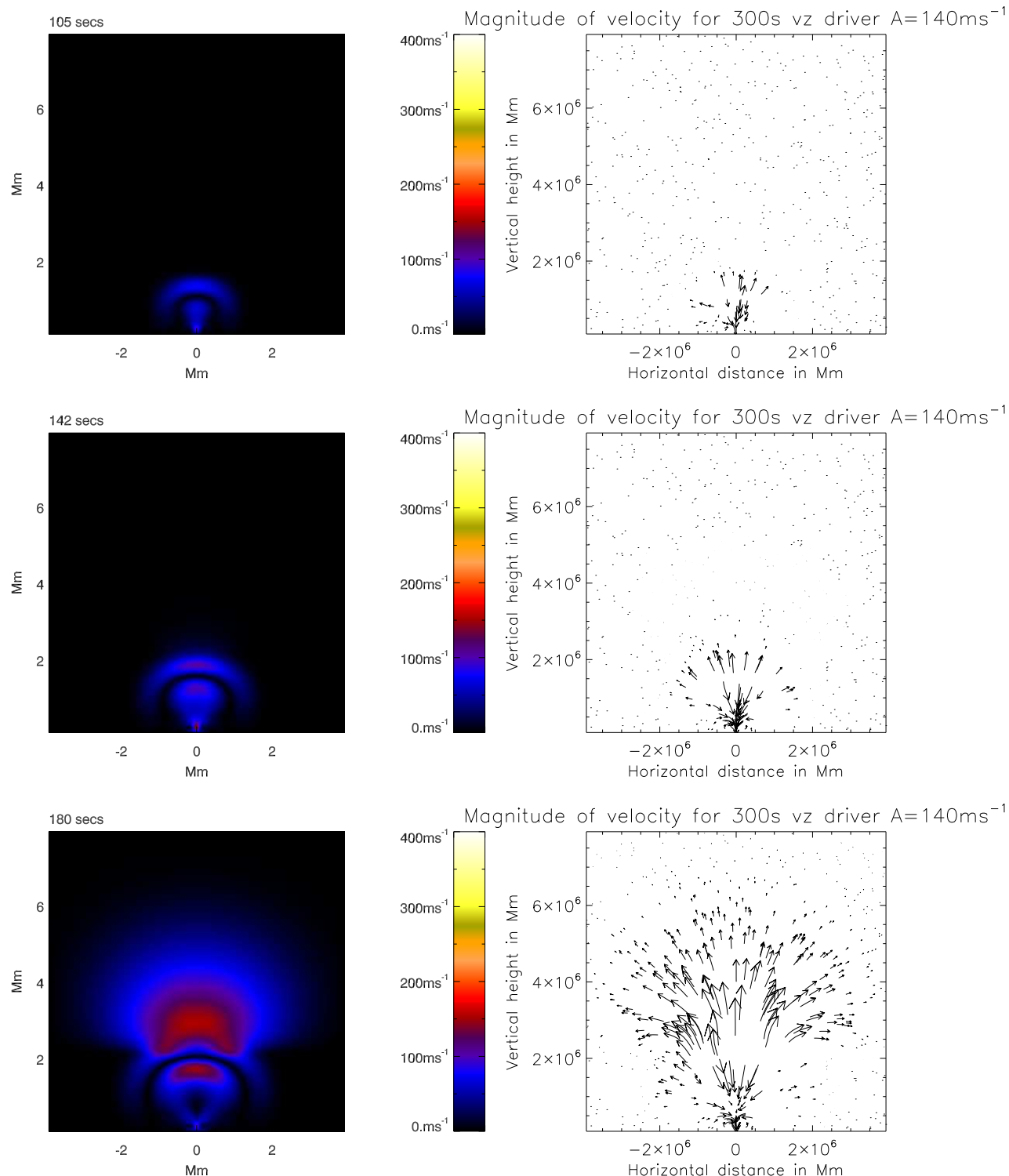
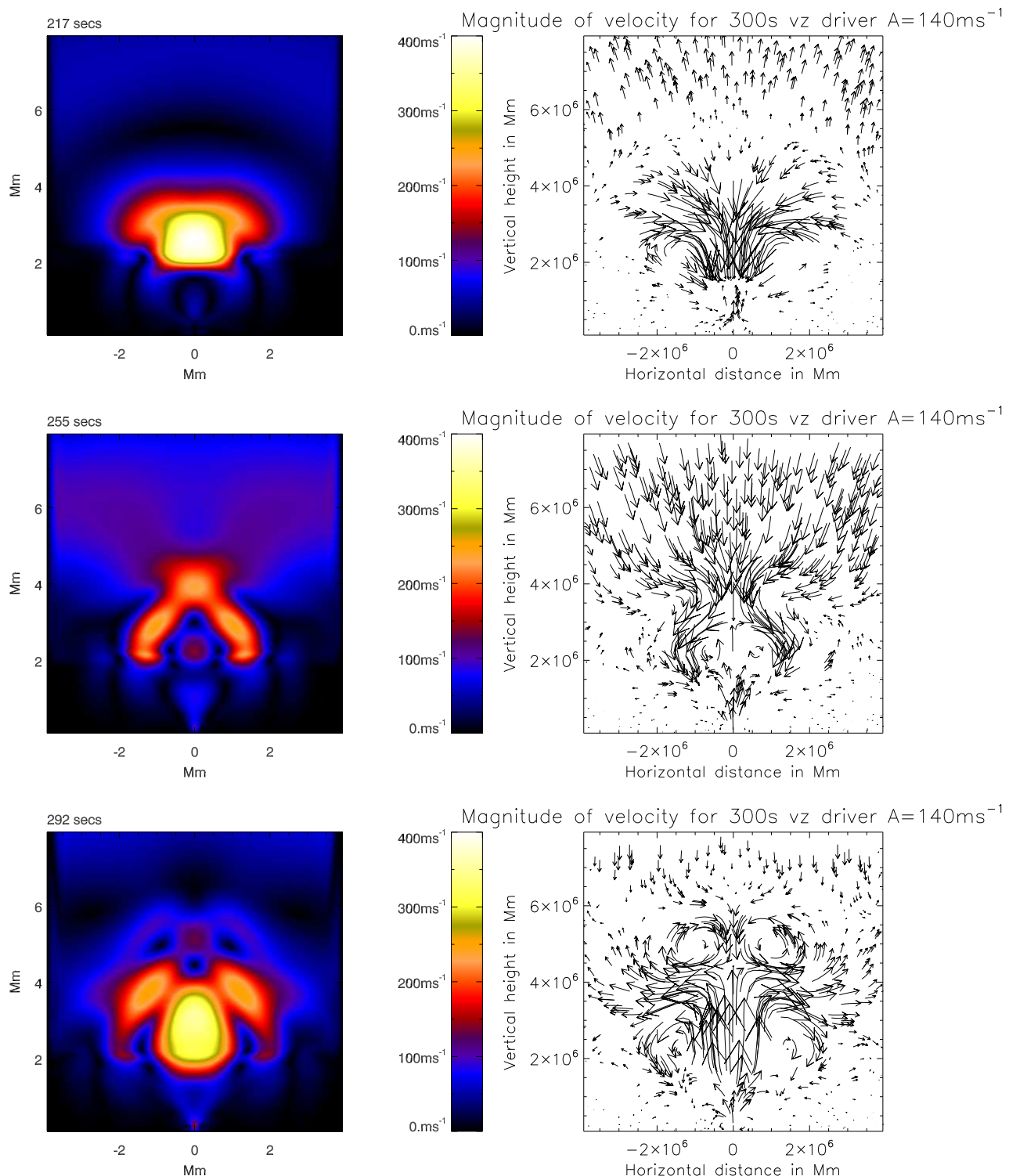


Figure 7.5: Vertical time difference image with vertical velocity peaks highlighted as follows: a) initial fast mode pulse and reflection highlighted with white lines; b) slow mode signals in the corona and possible slow mode signals in the photosphere/chromosphere highlighted with black lines; c) resonant wake oscillations highlighted with green ellipses; d) quasi-standing modes in the chromospheric cavity highlighted with green boxes.

sphere, and at the transition region (i.e. at heights where the cut-off period is shorter than 300 s). This is consistent with the theoretical prediction from Rae & Roberts (1982). The velocity maxima of the wake oscillations are highlighted on Fig. 7.5 with blue circles.

Referring back to Fig. 7.3, the first of these maxima in the fifth frame, taken after 255 seconds, is a circular light area centred at 0 Mm horizontally, at a height of about 2.5 Mm and with a diameter of about 1 Mm. This circular light area is surrounded by downflows (negative vertical velocity, i.e. dark areas) from the 'trough' behind the first pulse and its reflection - supporting the hypothesis that it has not propagated in from below or above. The wake oscillation can be similarly observed on the fifth frame of Fig. 7.6, where an island of upwards motion (purple 'dot' on the velocity magnitude plot) can be seen on the arrow plot surrounded by downflows.





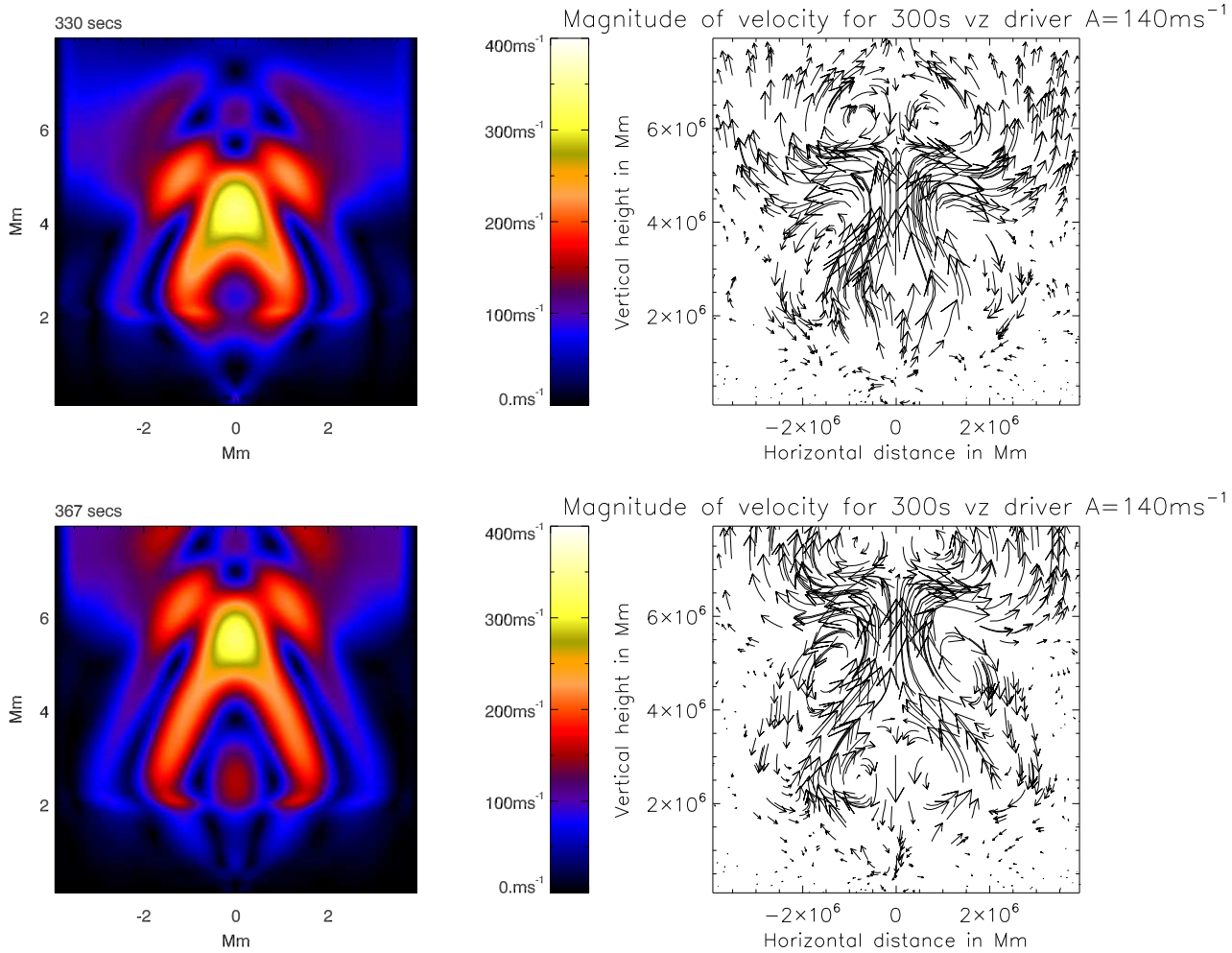


Figure 7.6: Series of snapshots of the velocity in the computational domain taken at 37.5 second intervals. The left hand side of each image shows the velocity magnitude only, while on the right hand side arrows represent the flow direction

The cut-off period at the transition region is shorter than the period of the driven wave, just as in the non-magnetic case, so a strong continuing transfer of energy from the driver to the resonant wake oscillation is expected. Looking below 1 Mm on Fig. 7.4, in the lower chromospheric region of short cut-off period, a similar peak of the resonantly excited wake oscillation is visible after about 200 seconds. This also mirrors the non-magnetic simulations.

The amplitude of the first wake oscillation at the transition region is somewhat higher than the amplitude of the initial fast mode wavefront as it crossed the transition region. This indicates that a very substantial fraction of the initial wave energy was deposited in the cut-off

mode.

The transition region wake oscillation results in a surface wave, again similar to the non-magnetic case. The surface wave propagates outwards from the centre of the transition region in both directions, and can be clearly seen in the final frames of Figs. 7.3 and 7.6, which shows both the velocity magnitude (left) and arrows representing the direction of flow (right). In the non-magnetic case, this surface wave extended to some extent into the corona (up to ~ 3.5 Mm), and was associated with granular circulation cells, c.f. Chapter 6.

In the magnetic case, the transition region surface wave extends into the corona further, linking to upwardly propagating slow modes (see below §7.3.3. Looking at the final three frames in Fig. 7.6, on the right hand side where the flow is represented by arrows, circulation cells associated with the surface wave are apparent.

7.3.3 Slow mode

The wake oscillation in the transition region, vertically above the driver, not only becomes the centre of a transition region surface wave but drives the propagation of slow mode signals into the corona. On Fig. 7.5 there is a very clear signal, highlighted with a dark line, propagating up into the corona driven by the wake oscillation.

Recall that in the corona, with the relatively weak 10 G field and the artificially high thermal pressure required for the simulation, we are in a high beta regime with the sound speed higher than the Alfvén speed. The coronal sound speed is therefore identical to the fast speed for vertical propagation, and is calculated to be $\sim 100,000$ ms $^{-1}$. The Alfvén speed is identical to the slow speed for vertical propagation, and is calculated to be $\sim 30,000$ ms $^{-1}$.

These coincide with the observed wave propagation speeds for the two signals highlighted with light and dark lines, respectively, in Fig. 7.5. The ‘light’ fast mode signal covers 4.5 Mm in approximately 40 seconds, while the ‘dark’ slow mode signal covers the same distance in about 125 seconds.

It is inferred that this is a slow mode not only because it is propagating at the coronal slow speed, i.e. the Alfvén speed, but because the signal is strongly confined by the field in sharp contrast to the fast mode. In the third and fourth frames of Fig. 7.6, the fast mode

quasi-spherical wavefront can be seen propagating up and out into the corona. This wavefront is strongly analogous to a pure sound wave in a non-magnetic atmosphere. In contrast, in frames 6, 7 and 8 the slow mode appears as a bright yellow ‘blob’ that is confined by the magnetic field to propagate upwards only.

This field confinement prevents the wave energy from dispersing. Whereas in the third and fourth frames the fast mode wavefront reduces in amplitude with height, the slow mode amplitude remains similar to the amplitude achieved at the transition region as it propagates, with thermal stratification driven growth countering the small energy losses through dispersion.

Comparing Fig. 7.3 with Fig. 4.5 it is clear that whereas in the non-magnetic case only very low amplitudes were recorded in the corona, in the case with magnetic field the maximum signal amplitudes in the corona are comparable to those at the transition region, both for the initial propagating fast mode, and the slow mode signals driven by the resonant excitation at the transition region. Also, where in the non-magnetic case the first reflected wavefront coming back down from the transition region was clearly visible, in the magnetic case its amplitude is significantly lower.

In short, the presence of a magnetic field allows substantial signal propagation into the corona of the transmitted initial fast mode pulse, and leakage of slow modes driven by the transition surface wave. This is despite reflection at the transition region, and the driven signal having a longer period than the cut-off frequency in both the photosphere/lower chromosphere and at the transition region. Indeed, the deposition of energy in the resonant mode at the transition region actually contributes to higher amplitude coronal signals than would be expected if there was no cut-off excitation - because the resonant excitation becomes a mechanism for mode conversion from dispersive fast to strongly field guided slow modes.

The slow mode generated by the wake oscillation is completely dominant thenceforward, and there is no apparent sign of further fast mode wavefronts propagating from the driver. This situation is analogous to the situation in the non-magnetic case, where the resonant oscillation at the transition region became entirely dominant over the driven signal. The presence of both fast and slow mode signals in the corona, linked to a fast mode signal coming from the transition region, shows that it is possible for a fast mode propagating into the chromospheric

cavity to generate slow modes with a shorter period propagating into the corona. In these simulations, the resulting coronal signal has a period of around 4 minutes compared to the driven period of 5 minutes. It seems plausible, especially given the dynamic nature of the solar atmosphere and the impact that this could have on transition region temperature gradients, and hence cut-off period, that a similar mechanism could be responsible for converting *p*-mode signals in the photosphere into 3 minute oscillations observed higher in the atmosphere.

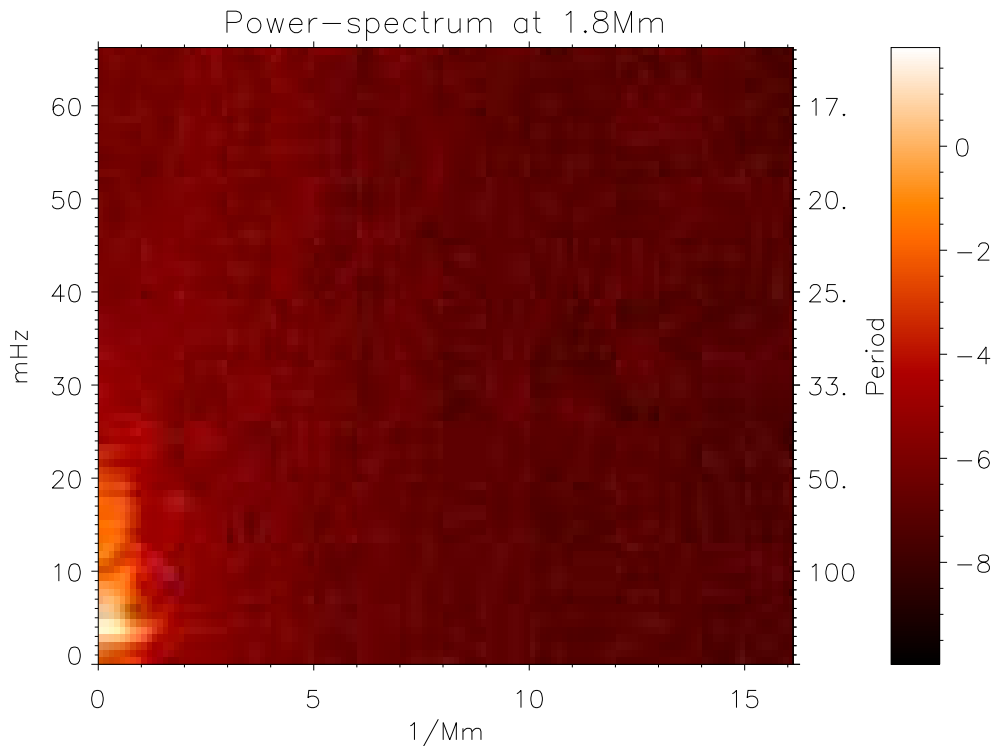


Figure 7.7: Power spectrum taken at a height of 1.8 Mm, in the chromospheric cavity

7.3.4 Chromospheric standing waves

In Chapter 4 one of the notable features of the undertaken simulations was the generation of a standing wave in the chromospheric cavity. The presence of this standing wave was particularly clearly displayed looking at a time-distance image taken along a vertical line through the point of driver application. In Fig. 7.4 a similar phenomenon is visible, between the line of 300 second cut-off in the lower chromosphere and the transition region. This standing signal is

highlighted with green boxes on Fig. 7.5. In the non-magnetic simulations, the existence of a genuine standing cavity mode was supported by the identification of the harmonic power peaks of the cavity mode on a power spectrum taken in the chromospheric cavity.

If the same phenomenon is present here, one would expect to see similar peaks in the relevant power spectrum. However, in Fig. 7.7, a power spectrum taken at a height of 1.8 Mm, there is no sign of the corresponding harmonics. In this case, the reflection of the signal at the transition region is relatively weak, and therefore the reflected (fast mode) signal would be entirely dominated by the propagating signal. The apparent standing wave is interpreted to be not a result of a signal trapped in the chromospheric cavity, but rather as the result of the interference between the resonant excitations on either end of the cavity. This finding is consistent with the hypothesis expressed by Fleck & Schmitz (1991).

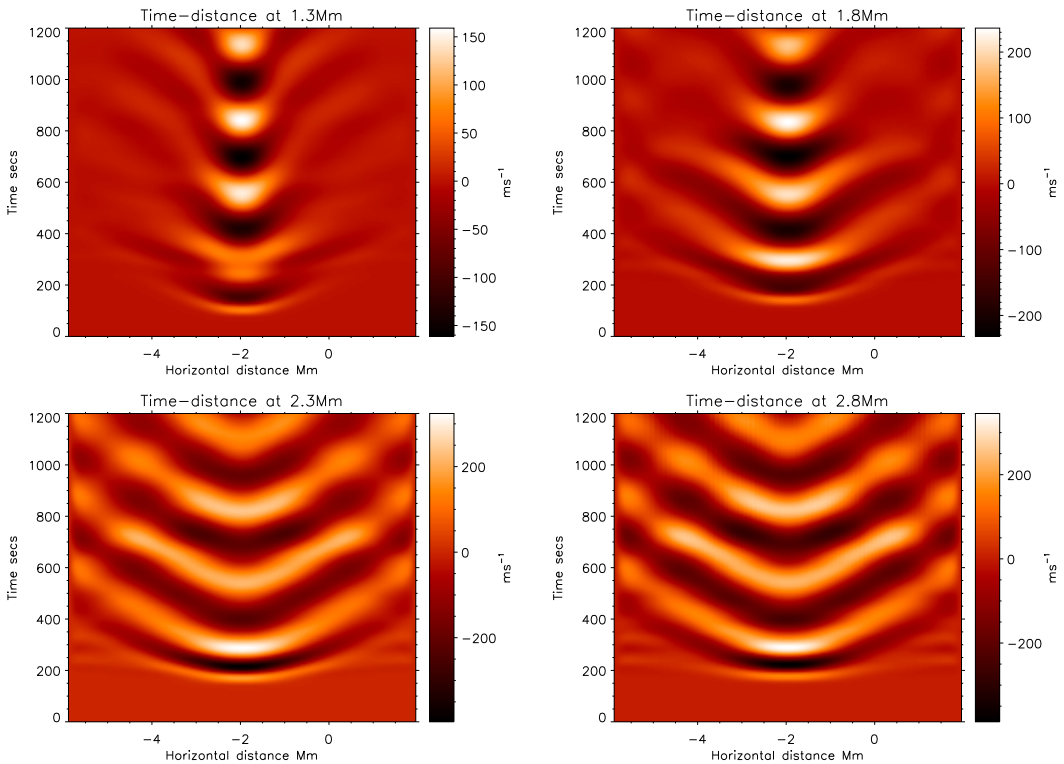


Figure 7.8: Time distance images taken along horizontal lines at 1.3 Mm, 1.8 Mm (both in the chromospheric cavity), 2.3 Mm (at the transition region) and 2.8 Mm (in the corona)

7.4 Summary

The results presented in this Chapter support several of the findings of the non-magnetic simulations presented in earlier chapters. The results are also broadly consistent with the results presented for the 3D case by Fedun et al. (2009). The resonant excitation of cut-off frequency modes in areas of the computational domain where the acoustic cut-off period is less than the driver period is observed in the same two areas (the photosphere/lower chromosphere and transition region) as in the non-magnetic case. This results, as before, in the generation of signals with a shorter period than the driven signal. In the simulations, this reduced period is around 4 minutes.

It seems plausible that this mechanism might be responsible for the generation by solar 5 minute p modes of 3 minute signals such as are observed in the corona. In particular, the transition region cut-off period is strongly linked to the temperature stratification in the region. A stronger stratification would reduce the cut-off period - and given the dynamic nature of the solar atmosphere, it seems very possible that areas of such increased stratification could exist, resulting in a correspondingly shorter period for resonantly excited transition region signals. Additional, more realistic, dynamic modelling would be required to test this possibility further.

The magnetic simulations also suggest that the generation of quasi-standing modes in the chromospheric cavity could be possible even without the reflection driven ‘cavity mode’ identified in the non-magnetic work.

In contrast to the non-magnetic simulations, in which the leakage of signals into the corona was very weak, the magnetic field acts as a guide enabling increased penetration of the initial fast mode pulse across the transition region. It also acts to allow the strong upward propagation of slow modes driven by the resonant transition region excitation. Both of these phenomena suggest that the presence of even a weak magnetic field, such as might be characteristic of the quiet Sun, could allow the leakage into the corona of energy from the solar global p modes.

The simulations presented here do not result in the lifting of substantial quantities of cool material into the solar corona (c.f. Chapter 5). If more energy were deposited through the driver into the system then the effect of a magnetic field on the cool protuberances observed in Chapter 5 could be investigated. Unfortunately, the numerical method used to obtain these

results is not robust in the case where these higher amounts of energy are deposited into the system.

Chapter 8

Summary and conclusions

8.1 Overview of the thesis

Photospheric oscillatory signals, and in particular the solar global p modes, are well observed, documented and explained (Christensen-Dalsgaard 2002). There is also a substantial and growing literature regarding the detection of oscillatory signals higher in the solar atmosphere, be that at chromospheric, transition region or coronal loop temperatures, and much hypothesising about possible sources for these observed signals (c.f. §1.2).

An area of particular interest (De Pontieu & Erdélyi 2006; Erdélyi 2006a,b) is the question of possible linkages between signals at photospheric heights and signals higher in the solar atmosphere. Conventional wisdom suggests that the propagation of solar p modes into the atmosphere is severely restricted by evanescence around the solar photospheric temperature minimum, where the local cut-off period falls somewhat below the 5 minute period characteristic of p modes—perhaps to the extent that there is no significant p mode leakage into the chromosphere and higher at all.

Despite this apparent barrier to transmission, the observation of 5 minute oscillations in the upper atmosphere has suggested that there may be mechanisms allowing leakage of 5 minute power into the chromosphere and onwards, and various papers (c.f. §1.2) have postulated connections between 5 minute photospheric signals and observed 3 minute atmospheric waves.

It has been proposed (De Pontieu et al. 2004) that inclined magnetic field may increase the effective atmospheric cut-off period and provide a guide allowing penetration of 5 minute

power into the higher atmosphere. It has also been suggested that a chromospheric cavity (Leibacher et al. 1982) or resonant excitation of cut-off period modes (Fleck & Schmitz 1991) may provide an explanation for the conversion of 5 minute photospheric signals into shorter period 3 minute signals.

In this thesis I have presented the results of two dimensional forward modelling, in which the propagation of photospheric oscillatory signals into the higher atmosphere is simulated. By investigating a realistically stratified equilibrium atmosphere, excited with several highly simplified synthetic drivers, I have aimed to extend the understanding of the propagation of acoustic and magneto-acoustic signals through the Sun's atmosphere.

Under the assumptions of ideal (M)HD, the particular focus of this work has been on the affect of driven period on signal propagation, and the consequences of resonant wake oscillations at the cut-off period on wave transmission.

The simulations were undertaken using two different numerical regimes. The non-magnetic simulations presented in Chapters 4, 5 and 6 were undertaken using the Versatile Advection Code (VAC) (Tóth 1996) to implement a Total Variation Diminishing Lax Friedrichs scheme for solving the partial differential equations of hydrodynamics. The magnetic simulations were undertaken using an extended version of the VAC called SAC (Shelyag et al. 2008) to implement a Central Differencing scheme, c.f. Chapter 3.

8.2 Conclusions

In this thesis I have demonstrated several possible mechanisms for the generation of upper atmospheric oscillatory phenomena by the leakage and propagation of solar photospheric signals.

Firstly, the numerical results demonstrate that wake oscillations at the cut-off period are indeed generated as predicted at the photospheric temperature minimum. However, by considering the stratified transition region as well it has been demonstrated that significant resonant wake oscillations may also be generated there. In all simulations, substantial fractions of the driver energy was able to propagate through the evanescent region at the photosphere. It has been demonstrated that:

- Resonant excitation of modes at the cut-off period will occur in the photosphere. In the work presented here, this excitation resulted in a dominant photospheric period below the 5 minute driven period. The dominant period of these excited signals in the simulations was not 3 minutes (often quoted as the cut-off period at the minimum itself), but rather between 4 and 5 minutes. It is suggested that based on semi-empirical models such as the VAL IIIc atmosphere, even if the minimum cut-off period in this region falls as low as three minutes, the ‘typical’ cut-off will be somewhat longer. This may restrict the potential for generation of signals with a dominant 3 minute power by this mechanism.

This phenomenon of wake excitation was repeated when simulations were performed with a 10 Gauss quiet Sun magnetic field, though the reduction in observed period was less.

- Resonant excitation of modes at the cut-off period will also occur if 5 minute signals reach the transition region. The strong thermal stratification at the transition region reduces the cut-off period substantially. The transition region therefore exhibits (in the VAL IIIc model) a shorter minimum cut-off than is found in the photosphere. In Chapter 4 it is demonstrated that the resonantly excited signal at the transition region is dominant (at that height) over the driven signal, or any leakage from the photospheric resonant mode. In the simulations presented in Chapter 4, the resultant dominant signal had a period of around 4 minutes. In the magnetic simulations, this was longer, ~ 280 s.

It is suggested that if resonant excitation at the cut-off period is to be proposed as an explanation for observed 3 minute chromospheric signals, it may be that these shorter period waves are being generated at the transition region rather than at the photospheric temperature minimum. In particular, dynamic effects might increase transition region gradients from their equilibrium values, resulting in temporarily reduced cut-off periods. Under the equilibrium assumptions simulated here, while the generation of shorter period resonant signals was observed, these signals had periods above 3 minutes.

- Either or both of the reflection of propagating signals in the chromospheric cavity and the resonant excitation of wake oscillations at the photospheric temperature minimum and transition region may be linked to the generation of quasi-standing modes in the chromosphere. The simulations demonstrated that both of these phenomena may occur. More sophisticated modelling would be required to identify which mechanism was

responsible for specific observed chromospheric oscillations.

- In all cases, the generation of transition region surface waves was observed in the forward modelling. In the simulations these waves propagate outwards along the transition region from the driver location, and are associated with circulation flows at transition region and lower coronal heights, c.f. Chapter 6. It is suggested that such waves might best be observed on the real Sun by considering Doppler analysis of transition region lines.
- Even without the presence of inclined magnetic field, in the simulations photospheric 5 minute oscillations were able to drive coronal signals. In the non-magnetic case, propagation beyond the transition region was weak for a point driver. However, driver configurations that transferred more substantial energy to transition region surface waves (paired drivers, horizontally coherent drivers) led to leakage of the surface wave power into the corona.

In the magnetic case, the transition region surface wave became a driver of field guided slow mode signals into the corona. These slow mode signals had comparable amplitude in vertical velocity to the amplitude of the transition region surface wave, and a shorter period than the driver period. The addition of inclined magnetic field would be expected to only increase the penetration of photospheric signals into the upper atmosphere.

8.3 Relevance to observations

There are currently several space borne observatories being used to observe and analyse solar oscillatory phenomena, notably Hinode, SDO, TRACE and SOHO. De Pontieu & McIntosh (2010) suggest that quasi-periodic propagating signals with periods of between three and ten minutes seen in coronal loops by TRACE and SOHO/EIT may be associated with upflows in coronal loop footpoints, driven from below.

Such upflows might be somewhat consistent with the analysis presented in Chapter 6, in which attention is drawn to the patterns of upflows and downflows associated with transition region guided waves. Hansteen et al. (2010) similarly observe blue shift in low coronal lines, and red shift in transition region lines. Such blue and red shifts are consistent with the prediction of granulation of the transition region by propagating transition region surface waves.

Fujimura & Tsuneta (2009) have observed MHD waves propagating along photospheric magnetic flux tubes in the photosphere using the Solar Optical Telescope of Hinode. They demonstrate that the phase difference between the line of sight magnetic flux, the line of sight velocity, the intensities of the line core, and the continuum intensity are consistent with longitudinal sausage mode and/or transverse kink mode oscillations, where there is interference between an upwardly propagating signal and a downward signal reflected at the transition region. The periods of the oscillations observed by Fujimura & Tsuneta (2009) are between 3 and 9 minutes, which would be consistent with leakage of power from solar global p modes.

Longitudinal sausage modes could be consistent with the propagation of the longitudinally driven photospheric slow mode signals discussed in §7.3.1. The observed phase relation suggests a standing wave in the photosphere/chromosphere, just as was found in the simulations presented in this thesis. Also consistent with the conclusions expressed in Chapter 7 was the observation that there is nevertheless a residual upward Poynting flux suggesting that a significant amount of energy is transmitted into the corona despite reflections at the transition region - just as is predicted by the modelling work here.

8.4 Further work

The simulations presented in this thesis are necessarily limited by the computational tools (in terms of computational power and computational codes) available when the simulations were conducted, the first of them in 2005. While the results presented here provide useful insights into important solar atmospheric physical phenomena, there is substantial potential to further enhance the results through the implementation of additional physics.

One obvious area for development is the shift from 2D to 3D modelling. The results in Chapters 4 and 7 have been extended to the 3D case by Fedun et al. (2009). Importantly, the results from 3D modelling serve to support the 2D observations, suggesting that the findings presented in this thesis are not rendered unphysical by the consideration of 2D geometry. Indeed, as discussed in §4.5, this consistency is what one would expect given that the 3D modelling has a degree of cylindrical symmetry. The increasing availability of powerful multi-node computers makes 3D simulations much more achievable and less time-intensive now than

in the past.

There is also great scope to enhance the results of such modelling work through the consideration of non-ideal physics such as non-LTE assumptions, radiative transport and emission, etc., (Hansteen et al. 2007, c.f.). The consideration of non-ideal physics would substantially affect the results of the simulations driven by short period drivers, where wave energy is likely to be dissipated so as to prevent the substantial transmission of wave energy to the corona observed in Chapter 4. Modelling radiative emission would give the added advantage of being able to more accurately predict the likely observational signatures of the phenomena found in the forward modelling. There is also the issue of unphysically high plasma beta in the simulations presented here. The addition of the turbulent microvelocity terms included in the semi-empirical modelling could allow a better matching of model plasma beta to the plasma beta in the real Sun. There is also the possibility of choosing alternate points of consistency between the simulated atmosphere and semi-empirical models. For instance, the corona might be more realistically modelled if the pressure and density at the higher rather than lower boundary, or in the transition region, were matched to the semi-empirical model values.

In Chapter 2, I pointed out that there has been some dissent in recent years over the existence of the ‘hot’ chromosphere that is traditionally present in semi-empirical models such as the VAL. The alternative hypothesis of a typically cold chromosphere heated by occasional shocks is partially investigated in Chapter 4. Whether the chromosphere is hot or cold, there is certainly scope to extend the modelling performed here to examine the more completely dynamic simulated solar atmospheres. This could, for instance, be achieved by running extended simulations using realistic photospheric velocity drivers based on observations, or by applying harmonic signals to a solar atmosphere that is not in underlying static equilibrium, but which is being stimulated by some synthetic background velocity noise.

The ultimate affirmation of any theoretical or computational prediction is the observation of predicted phenomena in data from the real Sun. Space missions such as SDO, Hinode, HiRISE and the Solar Orbiter will provide increasingly accurate solar atmospheric data. This work would be supported by observation of solar transition region granulation cells in Doppler velocity imaging at transition region temperatures, and by any further observations linking photospheric oscillatory signals to signals with shorter period at magnetically linked locations

in the solar transition region and corona. In addition to space missions, there is also the forthcoming Advanced Technology Solar Telescope (ATST). Future work should aim to use observed photospheric velocity signals as inputs, with the aim of using the forward modelling to reproduce observations of possibly linked signals in the higher atmosphere - such correspondances would provide strong evidence that the physical mechanisms identified here were indeed active in the real Sun.

Finally, the increasing availability of computing power will continue to make more computationally intensive simulations increasingly possible. This provides the scope for more, longer, larger simulations that include increasingly detailed physics. The challenge will be to produce the advanced codes to take advantage of this capacity, and to develop the visualisation and data analysis techniques to effectively deal with the vast quantities of data thus produced.

Bibliography

Alfvén, H. 1942, Nature, 150, 405

Avrett, E. H. 1996, in IAU Symp. 176: Stellar Surface Structure, ed. K. G. Strassmeier & J. L. Linsky, 503

Ayres, T. R. 1998, in IAU Symp. 185: New Eyes to See Inside the Sun and Stars, ed. F.-L. Deubner, J. Christensen-Dalsgaard, & D. Kurtz, 403

Ayres, T. R. 2002, ApJ, 575, 1104

Balmforth, N. J. & Gough, D. O. 1990, ApJ, 362, 256

Bel, N. & Leroy, B. 1977, A&A, 55, 239

Bogdan, T. J. 2000, Sol. Phys., 192, 373

Bogdan, T. J., Carlsson, M., Hansteen, V. H., et al. 2003, ApJ, 599, 626

Boris, J. P. & Book, D. L. 1973, Journal of Computational Physics, 11, 38

Brandenburg, A. 2003, Computational aspects of astrophysical MHD and turbulence, ed. A. Ferriz-Mas & M. Núñez, 269–+

Brynilsen, N., Maltby, P., Fredvik, T., & Kjeldseth-Moe, O. 2002, Sol. Phys., 207, 259

Cally, P. S. 2006, Royal Society of London Philosophical Transactions Series A, 364, 333

Carlsson, M. & Stein, R. F. 1992, ApJ, 397, L59

Carlsson, M. & Stein, R. F. 1995, ApJ, 440, L29

- Carlsson, M. & Stein, R. F. 2002, in ESA SP-505: SOLMAG 2002. Proceedings of the Magnetic Coupling of the Solar Atmosphere Euroconference, ed. H. Sawaya-Lacoste, 293–300
- Caunt, S. E. & Korpi, M. J. 2001, A&A, 369, 706
- Chan, K. L., Sofia, S., & Wolff, C. L. 1982, ApJ, 263, 935
- Chaouche, L. Y. & Abdelatif, T. E. 2005, Sol. Phys., 229, 255
- Christensen-Dalsgaard, J. 2002, Reviews of Modern Physics, 74, 1073
- De Moortel, I. & Hood, A. W. 2003, A&A, 408, 755
- De Moortel, I. & Hood, A. W. 2004, A&A, 415, 705
- De Moortel, I., Ireland, J., Hood, A. W., & Walsh, R. W. 2002a, A&A, 387, L13
- De Moortel, I., Ireland, J., Walsh, R. W., & Hood, A. W. 2002b, Sol. Phys., 209, 61
- De Pontieu, B. 1996, PhD thesis, Max-Planck-Institute for Extraterrestrial Physics
- De Pontieu, B. 2003, in Proc. NATO Advanced Research Workshop 2003 Budapest, Hungary, 277–296
- De Pontieu, B. 2004, in ESA Special Publication, Vol. 547, SOHO 13 Waves, Oscillations and Small-Scale Transients Events in the Solar Atmosphere: Joint View from SOHO and TRACE, ed. H. Lacoste, 25–+
- De Pontieu, B. & Erdélyi, R. 2006, Royal Society of London Philosophical Transactions Series A, 364, 383
- De Pontieu, B., Erdélyi, R., & De Moortel, I. 2005, ApJ, 624, L61
- De Pontieu, B., Erdélyi, R., & de Wijn, A. G. 2003a, ApJ, 595, L63
- De Pontieu, B., Erdélyi, R., & James, S. P. 2004, Nature, 430, 536
- De Pontieu, B. & McIntosh, S. W. 2010, ApJ, 722, 1013
- De Pontieu, B., Tarbell, T., & Erdélyi, R. 2003b, ApJ, 590, 502

- Erdélyi, R. 1998, Sol. Phys., 180, 213
- Erdélyi, R. 2006a, Royal Society of London Philosophical Transactions Series A, 364, 351
- Erdélyi, R. 2006b, in ESA Special Publication, Vol. 624, Proceedings of SOHO 18/GONG 2006/HELAS I, Beyond the spherical Sun
- Erdélyi, R. & Goossens, M. 1994, Ap&SS, 213, 273
- Erdélyi, R., Goossens, M., & Ruderman, M. S. 1995, Sol. Phys., 161, 123
- Erdélyi, R. & James, S. P. 2004, A&A, 427, 1055
- Erdélyi, R., Malins, C., Tóth, G., & De Pontieu, B. 2007, A&A, 467, 1299
- Fedun, V., Erdélyi, R., & Shelyag, S. 2009, Sol. Phys., 258, 219
- Fleck, B. & Deubner, F.-L. 1989, A&A, 224, 245
- Fleck, B. & Schmitz, F. 1991, A&A, 250, 235
- Fludra, A. 2001, A&A, 368, 639
- Fontenla, J. M., Avrett, E. H., & Loeser, R. 1990, ApJ, 355, 700
- Fossum, A. & Carlsson, M. 2005, Nature, 435, 919
- Fujimura, D. & Tsuneta, S. 2009, ApJ, 702, 1443
- Gough, D. & Toomre, J. 1991, ARA&A, 29, 627
- Hansteen, V. H., Carlsson, M., & Gudiksen, B. 2007, in Astronomical Society of the Pacific Conference Series, Vol. 368, The Physics of Chromospheric Plasmas, ed. P. Heinzel, I. Dotorovič, & R. J. Rutten, 107–+
- Hansteen, V. H., Hara, H., De Pontieu, B., & Carlsson, M. 2010, ApJ, 718, 1070
- Hart, A. B. 1954, MNRAS, 114, 17
- Hart, A. B. 1956, MNRAS, 116, 38
- Hasan, S. S. & van Ballegooijen, A. A. 2008, ApJ, 680, 1542

Hasan, S. S., van Ballegooijen, A. A., Kalkofen, W., & Steiner, O. 2005, ApJ, 631, 1270

James, S. 2004, PhD thesis, University of Sheffield

Kalkofen, W. 2001, ApJ, 557, 376

Kalkofen, W., Rossi, P., Bodo, G., & Massaglia, S. 1994, A&A, 284, 976

Kalkofen, W., Ulmschneider, P., & Avrett, E. H. 1999, ApJ, 521, L141

Lamb, H. 1909, Proc. London Math. Soc., s2-7, 122

Lamb, H. 1932, Hydrodynamics (Dover Publ., New York)

Leibacher, J., Gouttebroze, P., & Stein, R. F. 1982, ApJ, 258, 393

Leibacher, J. W. & Stein, R. F. 1971, Astrophys. Lett., 7, 191

Leighton, R. B. 1960, in IAU Symp. 12: Aerodynamic Phenomena in Stellar Atmospheres, ed. R. N. Thomas, 321–325

Lippincott, S. L. 1957, Smithsonian Contributions to Astrophysics, 2, 15

Lynch, D. K., Beckers, J. M., & Dunn, R. B. 1973, Sol. Phys., 30, 63

Malins, C. 2007, Astronomische Nachrichten, 328, 752

Malins, C. & Erdélyi, R. 2007, Sol. Phys., 246, 41

Marsh, M. S. & Walsh, R. W. 2006, ApJ, 643, 540

McDougall, A. M. D. & Hood, A. W. 2007, Sol. Phys., 246, 259

McWhirter, R. W. P., Thonemann, P. C., & Wilson, R. 1975, A&A, 40, 63

Miles, A. J. & Roberts, B. 1992, Sol. Phys., 141, 205

Mosser, B. 1995, A&A, 293, 586

Nessyahu, H. & Tadmor, E. 1990, Journal of Computational Physics, 87, 408

Nishikawa, T. 1988, PASJ, 40, 613

- Nordlund, A. 1985, Sol. Phys., 100, 209
- Nordlund, A. & Galsgaard, K. 1997, Tech. Rep., Astronomical Observatory, Copenhagen University, 1997
- O'Shea, E., Banerjee, D., & Doyle, J. G. 2006, A&A, 452, 1059
- O'Shea, E., Muglach, K., & Fleck, B. 2002, A&A, 387, 642
- Peres, G., Reale, F., & Golub, L. 1994, ApJ, 422, 412
- Plaskett, H. H. 1916, ApJ, 43, 145
- Rae, I. C. & Roberts, B. 1982, ApJ, 256, 761
- Roberts, B. 2004, in ESA SP-547: SOHO 13 Waves, Oscillations and Small-Scale Transients Events in the Solar Atmosphere: Joint View from SOHO and TRACE, ed. R. Erdélyi, J. Ballester, & B. Fleck, 1
- Ryu, D., Jones, T. W., & Frank, A. 1995, ApJ, 452, 785
- Ryutova, M. & Shine, R. 2004a, in American Institute of Physics Conference Series, Vol. 703, Plasmas in the Laboratory and in the Universe: New Insights and New Challenges, ed. G. Bertin, D. Farina, & R. Pozzoli, 203–208
- Ryutova, M. & Shine, R. 2004b, ApJ, 606, 571
- Schmitz, F. & Fleck, B. 1998, A&A, 337, 487
- Schunker, H. & Cally, P. S. 2006, MNRAS, 372, 551
- Secchi, A. 1877 (Paris: Gauthier-Villars)
- Shelyag, S., Erdélyi, R., & Thompson, M. J. 2006, ApJ, 651, 576
- Shelyag, S., Fedun, V., & Erdélyi, R. 2008, A&A, 486, 655
- Sheung, J. 2003
- Stein, R. F. & Leibacher, J. 1974, ARA&A, 12, 407

Stein, R. F. & Nordlund, A. 1998, ApJ, 499, 914

Sutmann, G., Musielak, Z. E., & Ulmschneider, P. 1998, A&A, 340, 556

Taroyan, Y. & Erdélyi, R. 2008, Sol. Phys., 251, 523

They Might Be Giants. 1998, Severe Tire Damage

Tóth, G. 1996, Astrophysical Letters Communications, 34, 245

Tóth, G. 1998, Computational Magnetohydrodynamics: Notes for an introductory level course

Ulrich, R. K. 1970, ApJ, 162, 993

Vernazza, J. E., Avrett, E. H., & Loeser, R. 1981, ApJS, 45, 635

Vögler, A. 2003, PhD thesis, Göttingen

Vonneumann, J. & Richtmyer, R. D. 1950, Journal of Applied Physics, 21, 232

Zhukov, V. I. 2002, A&A, 386, 653